Doctoral Dissertation

Isoscaling with Hydrogen and Helium Isotopes in Sn+Sn Collisions at 270 MeV/nucleon

Jung Woo Lee

Department of Physics

Graduate School

Korea University

February 2023

Isoscaling with Hydrogen and Helium Isotopes in Sn+Sn Collisions at 270 MeV/nucleon

by

Jung Woo Lee

---

under the supervision of Professor Byungsik Hong

A dissertation submitted in partial fulfillment of
the requirements for the degree of
Doctor of Philosophy (in Physics).

Department of Physics

Graduate School

Korea University

February 2023

The dissertation of Jung Woo Lee has been approved by the dissertation committee in partial fulfillment of the requirements for the degree of Doctor of Philosophy (in Physics).

November 2022

Committee Chair: Jung Keun Ahn

Committee Member: Su-Yong Choi

Committee Member: Byungsik Hong

Committee Member: Insik Hahn

Committee Member: Tadaaki Isobe

Isoscaling with Hydrogen and Helium Isotopes in Sn+Sn Collisions at 270 MeV/nucleon

by Jung Woo Lee

Department of Physics

under the supervision of Professor Byungsik Hong

ABSTRACT

The density dependent symmetry energy of the nuclear matter is an important and challenging subject in nuclear physics. The properties of nucleus at saturation density is largely known from studying those of stable nuclei in nature. However, it is rather difficult to study the properties at the subsaturation and suprasaturation densities region. Some observations as neutron star merger events have been made in astrophysics, but these events cannot be observed as frequently as we want. In the laboratory, the density dependent symmetry energy can be studied in the heavy-ion collisions, where a few times of the saturation density can be achieved depending on the beam energy.

On the other hand, although the cross sections of the produced and fragmented particles can be obtained from the heavy-ion collision experiments, in many cases, the experimental data alone cannot provide their detailed physics implications for nuclear matter deeply. As a result, the helps from the theory are often needed, but modeling and calculating the particle production from heavy-ion collisions are challenging in the various points of view. Such models include the the Statistical Multi-

fragmentation Model (SMM) that assumes equilibration of the system and describes the reactions at energy below 100 AMeV well. Another example is the Asymmetrized Molecular Dynamic (AMD) that simulates reactions in a time evolution dynamical process with various input physical parameters.

In this thesis, we analyze the Sn+Sn collisions at 270 AMeV from the SπRIT experiment performed in 2016. The rare-isotope beams were provided by Radioactive Isotope Beam Factory (RIBF), RIKEN in Japan. The collisions of the neutron rich ^{132}Sn + ^{124}Sn and nearly symmetric ^{108}Sn + ^{112}Sn were measured using the SπRIT Time Projection Chamber which is capable of tracking the charged particles in 3-dimensional space. The SπRIT experiment aims and expects to constrain the density dependent symmetry energy further from the recent results, as the current analysis can explore density regions higher than the saturation density for wider range of neutron-to-proton ratio of the system at 1.56 and 1.2.

The isoscaling investigated in this thesis is one of the ways of studying the properties of nuclear matter using the yield ratio of two similar collision systems. One can study the compositions of the clusters produced by the heavy-ion collisions and see how much the systems are equilibrated or thermalized. In this study, the calculation from the SMM and the AMD models are compared to the experimental data from SπRIT experiment as a function of the transverse momentum at mid rapidity. The comparison show that Sn+Sn collisions at 270 AMeV are equilibrated only in part as the breakdown of the isoscaling at high transverse momentum region is observed. The isoscaling effect for low energy particles agree with the AMD and SMM models. However, the observed breakdown of isoscaling for high energy particles cannot be explained at present.

Keyword: Heavy-ion collision, Nuclear equation of state, Rare-isotope, Nuclear fragmentation, Isoscaling, Statistical multi-fragmentation model, Asymmetrized molecular dynamics

Isoscaling with Hydrogen and Helium Isotopes in Sn+Sn Collisions at 270 MeV/nucleon

이정우

물리학과

지도교수: 홍병식

국문 초록

밀도에 의존하는 핵 대칭 에너지를 연구하는 것은 핵물리학에서 매우 중요한 도전과제이다. 포화밀도에서 핵의 성질은 자연에 존재하는 안정된 핵에 대한 연구로 알려져 있다. 그러나 포화밀도보다 낮거나 높은 밀도영역을 조사하는 것은 다소 어렵다. 천체물리학에서 중성자별 충돌과 같은 관측이 일부 이루어지기도 하지만 이러한 사건은 자주 관측할 수 없다. 그래서 실험실에서는 빔의 에너지에 따라 몇 배의 포화밀도를 얻을 수 있는 무거운 이온 충돌로 밀도에 의존하는 핵 대칭 에너지를 연구한다.

핵 충돌 실험에서는 생성되어 나온 입자의 단면적(cross section) 은 측정 할 수 있지만 실험만으로 핵 물질을 깊이 연구하는 데 필요한 모든 물리적 매개변수를 연구할 수 없다 보다 더 많은 정보를 얻기 위해서 중이온 충돌을 시뮬레이션하는 여러 모델을 사용한다. 이러한 모델 중 시스템의 열적 평형을 가정하는 Statistical Multi-fragmentation Model (SMM)은 100 MeV/u 미만의 에너지에서 핵 반응을 잘 설명한다. 또 Asymmetrized Molecular Dynamics (AMD) 모델은 최적화된 물리 매개변수를 이용하여 시간에 따른 역학 시뮬레이션 계산을 한다.

핵 충돌실험에서는 생성되어 나온 입자의 단면적은 측정할 수 있지만 실험만으로

핵 물질을 심도있게 연구할 수 있는 모든 물리적 매개변수를 연구할 수가 없다. 보다 많은 정보를 얻기 위해서는 중이온 충돌을 시뮬레이션하는 여러 모델을 사용해야 한다. 이러한 모델 중 시스템의 혈적 평형을 가정하는 SMM은 100 MeV/u 미만의 에너지에서 핵 반응을 잘 설명해 준다. 또 또 Asymmetrized Molecular Dynamics (AMD) 모델은 최적화된 물리 매개변수를 이용하여 시간에 따른 역학 시뮬레이션을 계산해 준다.

이 학위논문에서는 2016년에 수행된 SπRIT 실험에서 270 MeV/u 빔에너지를 이용한 Sn + Sn 충돌을 분석한다. 실험에서 사용되는 희귀 동의원소 빔은 일본 RIKEN에 있는 RIBF(Radioactive Isotope Beam Factory)에서 제공받았다. 중성자가 풍부한시스템 ^{132}Sn + ^{124}Sn 과 (양성자와 중성자 갯수가) 거의 대칭인 시스템인 ^{108}Sn + ^{112}Sn 은 3차원 공간에서 하전 입자를 추적할 수 있는 SπRIT Time Projection Chamber 에서 측정되었다. SπRIT 실험은 포화 밀도보다 높은 밀도 영역과 1.56 및 1.2의 넓은 범위의 중성자 대 양성자 비율을 탐색할 수 있기 때문에 밀도에 의존하는 핵 대칭 에너지부문 연구를 발전시키는데 기여할 수 있을 것이다.

Isoscaling은 두 개의 유사한 시스템 입자 생성비율에서 발생하는 중이온 충돌의 특성을 연구하는 방법 중 하나이다. 중이온 충돌에서 생성된 클러스터의 구성을 연구하고 시스템의 열형평성 정도를 측정한다. 이 연구에서는 mid-rapidity 영역에서 횡 운동량의 함수로 SπRIT 실험의 데이터를 SMM 그리고 AMD 모델 계산 결과와 비교한다. 그 결과로 270 MeV/u에서 Sn + Sn 충돌이 높은 횡 운동량에서 isoscaling 의 붕괴가 관찰됨에 따라 시스템이 부분적으로만 열적 평형을 이룬다는 것을 알게 되었다. 그러나 고에너지 입자에 대한 경향을 설명하기에는 여전히 어려움이 있다.

중심어: 무거운 핵충돌, 핵 상태방정식, 희귀동위원소, 파편핵, Isoscaling, Statistical multi-fragmentation model, Asymmetrized molecular dynamics

PREFACE

This dissertation is based on the SπRIT experiment campaign performed in 2016 at RIKEN, Japan. The SπRIT experiment is a fixed target experiment using a rare-isotope Tin(Sn) beam at the energy of 270 MeV/u colliding onto the natural Tin target. The SπRIT Time Projection Chamber inside the SAMURAI magnet measures events from the collisions.

The technical analysis and physics results of the SπRIT experiment have been published. A list of publications can be found in the following link:
https://groups.nscl.msu.edu/hira/NP1306_SAMURAI15/publications/.

This dissertation will introduce the experiment setups in Chapter 2. In Chapter 3, the software framework which has been developed for the experiment will be discussed. The data selection for the analysis will be explained in Chapter 4. Finally, the isoscaling analysis on the hydrogen and helium isotopes produced in the neutron-rich system ^{132}Sn + ^{124}Sn and nearly symmetric system ^{108}Sn + ^{112}Sn will be presented in Chapter 5.

Acknowledgement

제가 학부생 때부터 박사학위를 받을 때까지 긴 시간동안 물리를 가르쳐주시고 지도해 주신 홍병식 교수님께 깊은 감사를 드립니다.

대학교와 대학원에서 만나고 같이 공부하고 연구하며 이야기를 나눈 후배들, 동기들, 선배님들, 박사님들 그리고 교수님들 모두 감사합니다. 특히 학부 때부터 같이 알고 지내며 대학원에서 수많은 이야기를 나누고 생각을 공유한 재희 형, 많은 고민을 들어주고 선배로서 모범이 되어준 송교누나, 연구를 같이하며 가장 많이 알려주고 졸업하기까지 많은 관심을 준 진희 형, 연구실 선배로서 쓴소리와 많이 도움을 주신 현하 누나, 미희 누나 그리고 총이 형, 연구실 후배이면서 동기와 다름없었던 연주, 재범이 그리고 별이, 쾌활한 성격으로 긍정에너지를 나누어준 신형이와 우승이, 많은 연구에 관해서 토론해주고 공감해준 정혁이와 선호, 모두 감사드립니다. 같은 연구실은 아니지만 대학원 생활의 활력소가 되어준 상환이 형, 진현이 형, 현이 형, 정호 형, 현기 형, 호준이 형, 은지, 재혁이, 서주 누나 그리고 수영이 모두 감사합니다.

Thank you, Betty, for giving me a research subject and guiding my analysis. I could not have done it without your care. Bill, Aki, Mizuki, Murakami san, Ono san, and Rensheng, thank you for all the discussions during the analysis online or offline. Thank you, Sergio, for all the kind care in writing the paper. Justin, Jon, Kaneko, Zhang Yen, and Tommy, thank you for being my colleagues and letting me be your friends. Giordano, thank you, as you were my boss when developing software and made me confident. Thank you to all the people in SπRIT collaboration. It was a great opportunity for me to work with you.

항상 무한한 사랑과 관심을 주시고 제 미래에 대하여 저보다 더 많이 걱정해 주시고 조언해 준 엄마, 아빠 감사합니다. 제가 부족함에도 질책 대신 지속적인 응원을 보내주신 가족 여러분들 모두 감사합니다. 부족한 저를 사위로 맞아주시고 따듯하게 대해주신 장인어른 그리고 장모님께 감사드립니다. 제가 박사학위를 받을 수 있도록 도와주시고 지금까지 기다려주신 모든 분께 감사의 마음을 드립니다.

마지막으로 제 인생의 동반자이자 세상에서 가장 사랑하는 지혜 그리고 저희 둘의 가장 큰 자랑인 다솔이에게 감사한 마음을 전합니다.

Contents

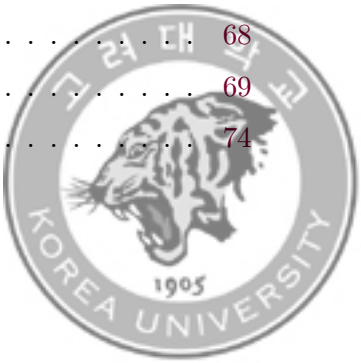

List of Figures

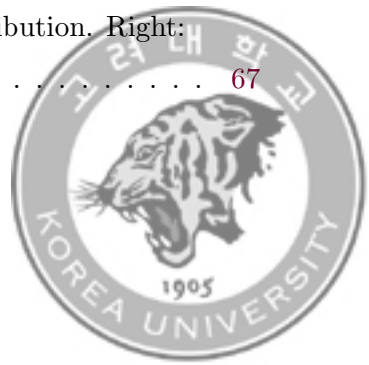

List of Tables

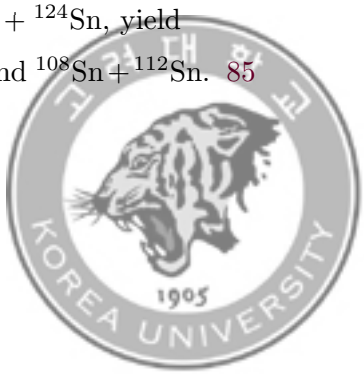

Chapter 1

Introduction

1.1 Nuclear Equation of State

One of the main goals of nuclear physics is to understand the fundamental properties of nuclear matter. The properties of nuclear matter can be described by the nuclear Equation of State (EoS), which essentially reflects the energy per nucleon [14] as a function of nucleon density ρ. Expanding of EoS in terms of the isospin asymmetry $\delta = (\rho_{\rm n} - \rho_{\rm p})/\rho$ where ρ_n and ρ_p are the neutron and proton densities, respectively, we find

$$E(\rho, \delta) = E_0(\rho) + S(\rho)\delta^2. \tag{1.1}$$

The odd δ terms are removed by assuming the charge independence of nuclear force. The higher-order terms of δ are usually neglected because they are expected to be similar or less than 1 MeV [15]. In Eq. 1.1, $E_0(\rho)$ is the energy of the symmetric nuclear matter as $E(\rho, \delta)$ becomes $E(\rho, 0) = E_0(\rho)$ for $\delta = 0$. The second term $S(\rho)$ is often referred to as symmetry energy. By rearranging the equation with $\delta = 1$,

$$S(\rho) = E(\rho, 1) - E_0(\rho), \tag{1.2}$$

representing the energy difference between the pure neutron matter and the symmetric nuclear matter.

At the nuclear saturation density (the density of the normal nuclear matter) $\rho_0 \approx 0.16$ fm^{-3}, the binding energy of the symmetric matter is $\mathrm{E}_0(\rho_0) \approx 16$ MeV. A useful way of studying symmetry energy is to use the expansion around the saturation density as

$$S(\rho) = S_0 - Lx + \frac{1}{2}K_{\mathrm{sym}}x^2 + O(x^3), \tag{1.3}$$

where $x = (\rho - \rho_0)/3\rho_0$. (In other references, the symmetry energy S_0 at the saturation density is sometimes expressed by J.) L and K_{sym} are the slope and curvature parameters, respectively, at the saturation density ρ_0. In Fig. 1.1, the density dependence of the symmetry energy is shown for different parameter sets chosen from Skyrme interactions that reproduce the experimental binding energy difference between ^{132}Sn and ^{100}Sn [1]. Even though the symmetry energy was partly constrained at subsaturation densities, a large variation can be particularly at high densities. The shaded area in Fig. 1.1 corresponds to the constraint obtained by the Pygmy Dipole Resonance (PDR) and the isobaric analog states from Heavy Ion Collisions (HIC) in Ref. [16]. There have been a lot of other efforts to constrain the S_0 and slope parameter L as shown in Fig. 1.2.

The relevance of the density dependence of the symmetry energy to the nuclear equation of state (EoS) of neutron stars has been emphasized in many studies [14, 17, 18, 19]. Because slope parameter L can be expressed as $L = 3\rho\,(dS/d\rho)|_{\rho_0} = (3/\rho_0)P_0$, where P_0 is the pressure of the symmetry energy at saturation density ρ_0, which gives an essential link to neutron star research [20].

The high-density states of nuclear matter can be achieved experimentally through HIC in the laboratory. The HIC can probe symmetry energy, especially using the rare-isotope beams. Depending on the beam energy, a density up to a few times the saturation density can be achieved. The neutron to proton ratios charged pion ratios and elliptic flow differences [21, 22, 23] were proposed to be sensitive to the

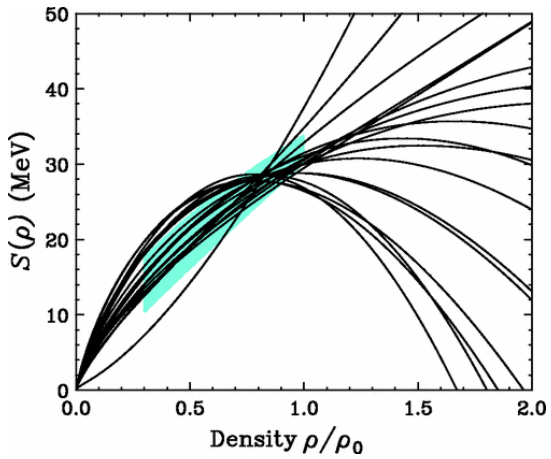

Figure 1.1 Density dependence of the symmetry energy from the Skyrme interactions used in Ref. [1]. The shaded region is obtained from HIC experiments and corresponds to the shaded region in Fig. 1.2. Adopted from Ref. [2].

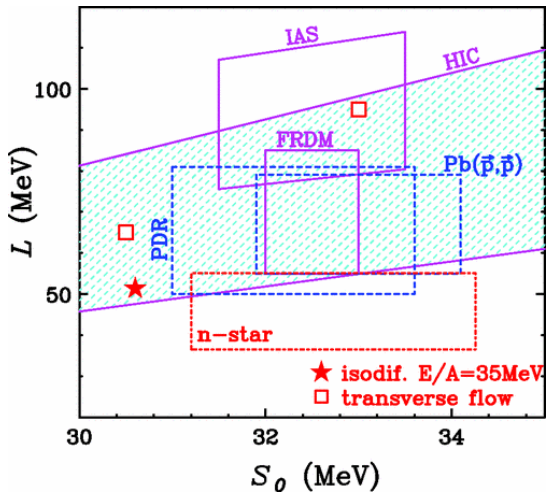

Figure 1.2 Constraints on the slope L and magnitude S_0 of the symmetry energy at saturation density from different experimental observables. The experimental methods are labeled next to the boxes with the estimated uncertainties. Adopted from Ref. [2].

dynamics of single nucleons. In addition, the triton-to-helium ratios t/^{3}He [24] or isoscaling [25, 26] are the probes influenced by the light-cluster production.

1.2 Heavy-Ion Collision

During the collisions involving heavy-ions at energies well above the Coulomb barrier, the nuclear matter is driven through very different configurations. In the early stages, violent collisions between its constituents occur, heating the matter. If these collisions occur above the production thresholds, sub-atomic particles such as pions, for instance, maybe produced [5, 22, 27, 28]. Many particles are ejected in this pre-equilibrium stage [29], carrying away some appreciable amounts of energy from the system. At the same time, the colliding nuclei lead to the compression of nuclear matter, and densities higher than the saturation density can be formed at the center of mass [22, 30].

The dynamical treatments [30] are well suited to study such early stages as the density, the isospin configuration, and the temperatures attained by the system is sensitive to the physical input parameters employed by the models [29, 31, 32, 33]. Therefore, meaningful information on the Nuclear Equation of State (EOS) may be extracted by these dynamical approaches. Conversely, experimental observations may also help to constrain some of these input parameters, such as the in-medium nucleon-nucleon cross-section, which plays a crucial role in the nuclear stopping [34, 35] for example. Determining the input parameters of the models is of particular interest. Besides affecting different observables, it is closely related to the rate of equilibration of the system, providing, in this way, deeper insight into the dynamics of the collisions.

In the subsequent phases, a freeze-out configuration is reached, and many fragments, including protons and neutrons, are emitted [29]. Their behaviors can be described both by dynamical [5, 30] and statistical models [30, 36, 37, 38]. In the former, they appear as a result of the dynamic path taken by the system. While in the latter, a freeze-out configuration is assumed, and its adequacy is checked by com-

paring the model predictions to the experimental observations [30, 36, 37]. In both cases, most of the excited fragments predicted by the models would decay before detection and, therefore, a deexcitation treatment [39, 40] must be applied before comparing the theoretical predictions with the experimental data. Consequently, the deexcitation process may blur significant vestiges of the freeze-out configuration.

As mentioned above, the symmetry-energy probes, such as the triton-to-helium ratios and isoscaling, are strongly related to the multi-fragmentation in the reaction. Fig. 1.3 shows fractions of produced charged particles from HIC experiments for different collision energies. In Au+Au at 400 MeV/u, 30 % of the emitted charged particles are protons, while the fraction goes down to 25 % in Xe+CSI at 250 MeV/u. Furthermore, this ratio hit 10 % for energies lower than 50 MeV/u. On the other hand, the fraction of the hydrogen and helium isotopes exceeds over 85 % at a collision energy of 250 MeV/u.

1.3 Isoscaling

From the thermodynamic picture, the primary fragment yield from the intermediate- and high-energy HIC can be calculated assuming that thermal equilibrium is established in the grand-canonical ensemble limit [41]:

$$Y^{\text{primary}}(N,Z,T) \simeq \frac{VA^{3/2}}{\lambda_T^3}\omega(N,Z,T)\,\exp\left[\frac{E_B(N,Z)+N\mu_n+Z\mu_p}{T}\right], \qquad (1.4)$$

where N, Z, and A are the neutron, proton, and mass number of the isotope, T and V are the temperature and volume, respectively, of the system, $\lambda_T = h/\sqrt{2m_N T}$ is the thermal nucleon wavelength with the plank constant h and nucleon mass m_N. μ_n and μ_p are the neutron and proton chemical potentials, and E_B is the ground state binding energy of the isotope. The factor $\omega(N,Z,T) = \sum_j [2J_j(N,Z)+1]\,\mathrm{e}^{-E_j(N,Z)/T}$ is the intrinsic partition function (J_j and E_j being the spin and excitation energy, respectively, of the isotope) summing over all the stable states j.

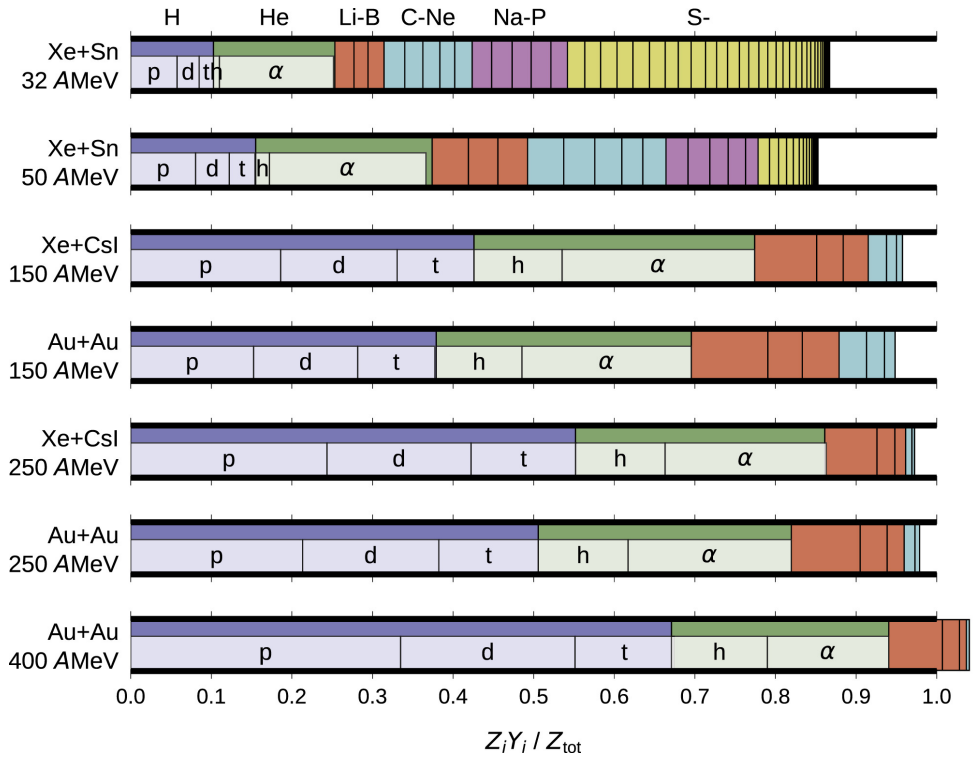

Figure 1.3 Fractions of produced charged particles in heavy-ion collisions of ^{129}Xe+^{nat}Sn (32 and 50 AMeV), ^{129}Xe+CsI (150 and 250 AMeV) and ^{197}Au+^{197}Au (150, 250 and 400 AMeV). Fractions were obtained from the INDRA data [3] for ^{129}Xe+^{nat}Sn and from the FOPI data [4] for ^{129}Xe+CsI and ^{197}Au+^{197}Au. Adopted from Ref. [5].

In the experiments, the fragments cool down to the ground state very fast ($\sim 10^{-20}$ s) from the excited state before they are observed at the detectors ($> 10^{-9}$ s). These secondary decays from the unstable states to the ground state can be assumed as multiplicative factor $f(N, Z, T)$ [25]. In this context, the final yield of the fragments can be written as

$$Y(N, Z, T) = f(N, Z, T)\, Y^{\text{primary}}(N, Z, T). \tag{1.5}$$

We define the ratio of the isotope yield between the two systems, 2 and 1

$$R_{21}(N, Z) = \frac{Y_2(N, Z, T_2)}{Y_1(N, Z, T_1)}. \tag{1.6}$$

By convention, system 2 has larger isospin asymmetry than system 1. If the two systems have the same temperatures, the binding energy term in the Eq. (1.4) cancels out in the ratio of Eq. (1.6). On the further assumption that the secondary decay effect can be canceled out between the two systems as verified in the Ref. [42], the ratio simplifies to

$$R_{21}(N, Z) = C \exp\left(N\frac{\Delta\mu_n}{T} + Z\frac{\Delta\mu_p}{T}\right), \tag{1.7}$$

where $\Delta\mu_n$ and $\Delta\mu_p$ are the difference of the chemical potentials between two systems "2" and "1". The normalization factor C is not a physical parameter, and the value is mostly close to 1. Conventionally, we use $\alpha = \Delta\mu_n/T$ and $\beta = \Delta\mu_p/T$ as scaling parameters.

$$R_{21}(N, Z) = C \exp\left(\alpha N + \beta Z\right). \tag{1.8}$$

This relation, namely "Isoscaling" can be studied in the isotope yield ratio without caring about the secondary decay or the binding energy of the isotopes when

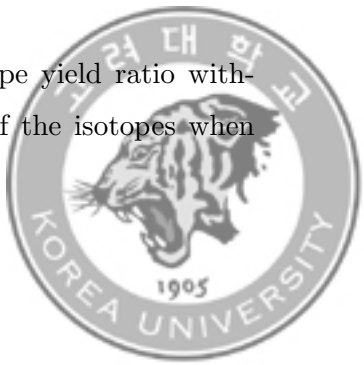

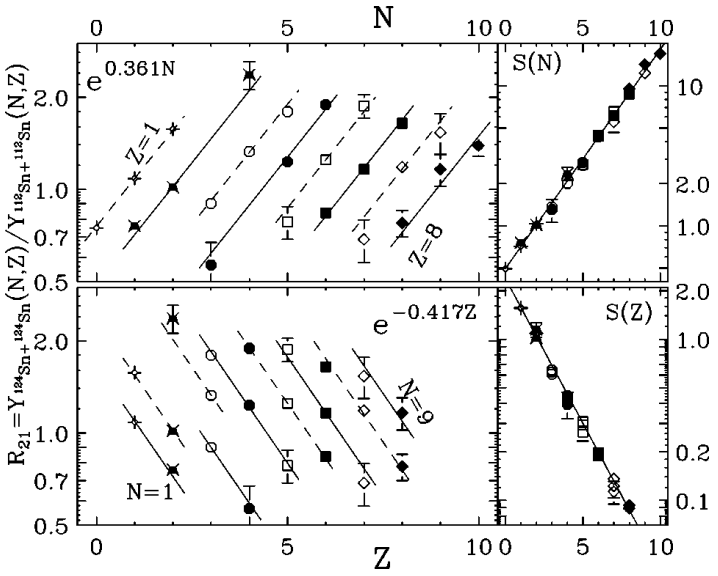

Figure 1.4 The isoscaling first reported from ^{124}Sn + ^{124}Sn and ^{112}Sn + ^{112}Sn systems at 50 MeV/u. Adopted from Ref. [6].

appropriate systems are chosen.

Isoscaling was first reported in the Refs. [25, 26] from the two symmetric systems ^{124}Sn+^{124}Sn and ^{112}Sn+^{112}Sn at 50 MeV/u as shown in Fig. 1.4. The top left panel shows the yield ratio of two systems as a function of N in a log scale. It is found that the isotopes with the same Z can be fitted by the straight line, resulting from fit using Eq. (1.8) with given Z. The bottom left panel shows the same data but as a function of Z where the fit lines correspond to the isotones with the same N. For the compact display of the isoscaling, the isotope function ($S(N)$) or isotone function ($S(Z)$) can be used:

$$S(N) = R_{21}(N,Z)\exp(-Z\beta), \tag{1.9}$$

$$S(Z) = R_{21}(N,Z)\exp(-N\alpha). \tag{1.10}$$

The fitted parameters from the systems ^{124}Sn + ^{124}Sn and ^{112}Sn + ^{112}Sn at 50

MeV/u are $\alpha = 0.36$ and $\beta = 0.41$. The value of α having positive value means that the more neutron-rich system ^{124}Sn + ^{124}Sn has larger neutron chemical potential compared to that of less neutron-rich system ^{112}Sn + ^{112}Sn.

Isoscaling has been observed in various experimental reactions. In Ref. [43], it is shown that the scaling property does not hold for the very heavy fragments ($Z > 26$ and $N > 35$) produced in the Kr+Sn reactions at 35 MeV/u studied in that work. In Ref. [44], the parameter α is found to be proportional to the difference between the Z/A of the two sources and exhibits a clear dependency on the excitation energy. In addition, Ref. [45] reveals a different behavior of the scaling parameters for fragments originating from the participant region or the projectile-like fragments. Isocaling was also found in very asymmetric collisions induced by light-ion beams [46].

Apart from the experiment results, isoscaling has been observed in all statistical models that achieve chemical equilibrium, including the Statistical Multi-fragmentation Model (SMM) employing the micro-canonical and the canonical ensembles [42] and in the expanding emission source model [42]. Furthermore, isoscaling is also observed in the Antisymmetrized Molecular Dynamics (AMD) [47] model, which makes no apriori assumptions on thermal equilibration.

1.4 Isotopic Temperature

As emphasized above, the isoscaling method is only valid when the temperatures of the two systems are the same. However, a direct measure of the temperature of the collision is impossible. An indirect measure of the temperature of the collision using the yield of different particles can be evaluated from Eq. (1.4).

Since the free-proton and free-neutron density are

$$\rho_p = \frac{Y^{\text{primary}}(1,1,T)}{V} = \frac{2J_p+1}{\lambda_T^3}\exp\left(\frac{\mu_p}{T}\right), \tag{1.11}$$

$$\rho_n = \frac{Y^{\text{primary}}(1,0,T)}{V} = \frac{2J_n+1}{\lambda_T^3}\exp\left(\frac{\mu_n}{T}\right), \tag{1.12}$$

the Eq. (1.4) then can be rewritten as

$$Y^{\text{primary}}(N,Z,T) = \frac{VA^{3/2}\lambda_T^{3(A-1)}}{2^A}\,\omega(N,Z,T)\rho_n^N\rho_z^Z\,\exp\left[\frac{E_B(N,Z)}{T}\right]. \quad (1.13)$$

The yield ratio between two different isotopes (N,Z) and $(N,Z+1)$ is

$$\begin{aligned}\frac{Y(N,Z)}{Y(N',Z')} &= \left(\frac{A}{A'}\right)^{3/2}\left(\frac{\lambda_T^3}{2}\right)^{A-A'}\frac{\omega(N,Z)}{\omega(N',Z')} \\ &\quad\cdot\,\rho_n^{N-N'}\rho_z^{Z-Z'}\exp\left[\frac{E_B(N,Z)-E_B(N',Z')}{T}\right]. \quad (1.14)\end{aligned}$$

and the free-proton density becomes

$$\begin{aligned}\frac{Y(N,Z)}{Y(N,Z+1)} &= \left(\frac{A}{A+1}\right)^{3/2}\frac{2}{\lambda_T^3}\,\frac{\omega(A,Z)}{\omega(A,Z+1)} \\ &\quad\cdot\,\rho_z^{-1}\exp\left[\frac{E_B(N,Z)-E_B(N,Z+1)}{T}\right]. \quad (1.15)\end{aligned}$$

Here we considered only the ground state of the isotopes because the excitation energy of H and He isotopes are not significantly lower than considered temperatures (which is below tens of MeV). Also we apply $\lambda_T^3 = 4.2\cdot 10^{-36}T^{-3}cm^{-3}$ where T is expresse in MeV.

$$\begin{aligned}\rho_z &= \left(\frac{A}{A+1}\right)^{3/2}\frac{10^{36}}{2.1}T^{3/2}\,\frac{2J_0(A,Z)+1}{2J_0(A,Z+1)+1} \\ &\quad\cdot\exp\left[\frac{E_B(N,Z)-E_B(N,Z+1)}{T}\right]\frac{Y(N,Z+1)}{Y(N,Z)}. \quad (1.16)\end{aligned}$$

Temperature evaluation depends on the isotopes we examine in the experiments. An easiest case is combination of ^{2}H, ^{3}H, ^{3}He and ^{4}He. This is because the energy spectra measured at large angles for these isotopes show similar exponentially decaying spectra in intermediate- and high-energy heavy-ion collisions, suggesting

they might share a common origin inside the source. From the free-proton density evaluated from yield ratio of ^{3}He and ^{2}H and yield ratio of ^{4}He and ^{3}H, we get

$$\rho_p = 0.39 \cdot 10^{36}\, T^{3/2} \exp\left[-5.5/T\right] \frac{Y(^3\mathrm{He})}{Y(^2\mathrm{H})} \tag{1.17}$$

$$= 0.62 \cdot 10^{36}\, T^{3/2} \exp\left[-19.8/T\right] \frac{Y(^4\mathrm{He})}{Y(^3\mathrm{H})}, \tag{1.18}$$

leading to

$$T_{\text{He-H}} = 14.3 \cdot \ln^{-1}\left[1.6 \cdot \frac{Y(^2\mathrm{H}) \cdot Y(^4\mathrm{He})}{Y(^3\mathrm{H}) \cdot Y(^3\mathrm{He})}\right]. \tag{1.19}$$

This specific temperature using hydrogen and helium isotope is usually called as Hydrogen Helium ratio and denoted as H-He temperature or $T_{\text{H-He}}$. In Ref. [48], it was shown that the H-He temperature is independent of the neutron-to-proton ratio of the system. It should be noted that the H-He temperature is not an absolute temperature. However, it is useful when exploring the physical phenomenon where the temperature is needed as a reference.

Chapter 2

SπRIT Experiment

The SπRIT experiment took data from the Radioactive Isotope Beam Factory (RIBF) [7, 49] in RIKEN, Japan. The rare-isotope beam of Tin (Sn) was produced at 270 AMeV and impinged on the isotopically enriched Tin (Sn) target. The SπRIT-TPC was placed right after the target to detect charged particles from the collisions. We measured four Sn+Sn collision systems and summary of them are listed in the Table 2.1. This chapter will discuss the setup and the detectors used in the SπRIT experiment.

2.1 Radioactive Isotope Beam Factory

The experiment used the Tin isotope beams at 270 MeV/u at Radioactive Isotope Beam Factory (RIBF). The fixed-energy mode of RIBF was used to accelerate primary beam ^{238}U for neutron-rich beams (^{132}Sn and ^{124}Sn) and ^{124}Xe for less neutron-rich beam (^{112}Sn and ^{108}Sn) were used. The primary is first accelerated by the RIKEN Heavy-ion Linac 2 (RILAC2), and accelerated through the four cyclotrons RRC, fRC, IRC, and SRC to rich the fixed kinetic energy of 345 MeV/u. At the entrance of the superconducting fragment separator, BigRIPS, production target Be was installed for the in-flight fission of primary beams ^{238}U and ^{124}Xe. The thick-

Beam	Target	N/Z
^{132}Sn	^{124}Sn	1.57
^{108}Sn	^{112}Sn	1.2
^{112}Sn	^{124}Sn	1.36
^{124}Sn	^{112}Sn	1.36

Table 2.1 List of collision systems used in the SπRIT experiment.

ness of the target was 4 mm to produce the most neutron-rich beam ^{132}Sn and 1 mm for others ^{124}Sn, ^{112}Sn and ^{108}Sn beams. The fragments from the fission were filtered out in BigRIPS to select the desirable magnetic rigidity $B\rho$ for the experiment. As fragments contain many other isotopes out of interest, the isotopes are identified in the phase space of atomic mass number mass-to-charge ratio A/Q vs. Z [50].

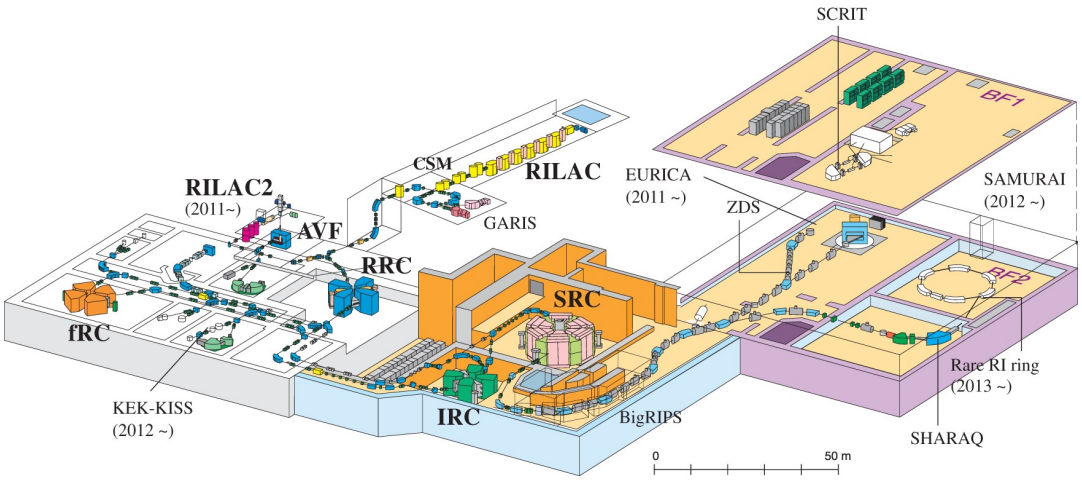

Figure 2.1 Adopted from Ref. [7]

2.2 SπRIT Time Projection Chamber

The SπRIT-TPC is a cuboid-shaped TPC designed to identify the charged particle tracks from the fixed target event. The exploded view of the SπRIT-TPC is shown

in Fig. 2.2. The local coordinates are defined by choosing the beam axis as $z - axis$. The SπRIT-TPC is a 3-dimensional tracker. The pad plane is installed at the top of the TPC facing the y-axis. It measures the event from pads (channel) in a grid along x and z-axis. The remaining y-axis value is measured from the array of 512 switched capacitors represented by the time bucket in each pad. The charges are stacked in each time bucket, whereas one-time buckets accumulate charges every 40 ns. The time buckets are then converted to y-position from the simulated electron drift velocity. A magnetic field of 0.5 T was provided from the SAMURAI magnet [51] where TPC is placed inside. The curved tracks of charged particles from the magnetic field enable measuring the track's momentum.

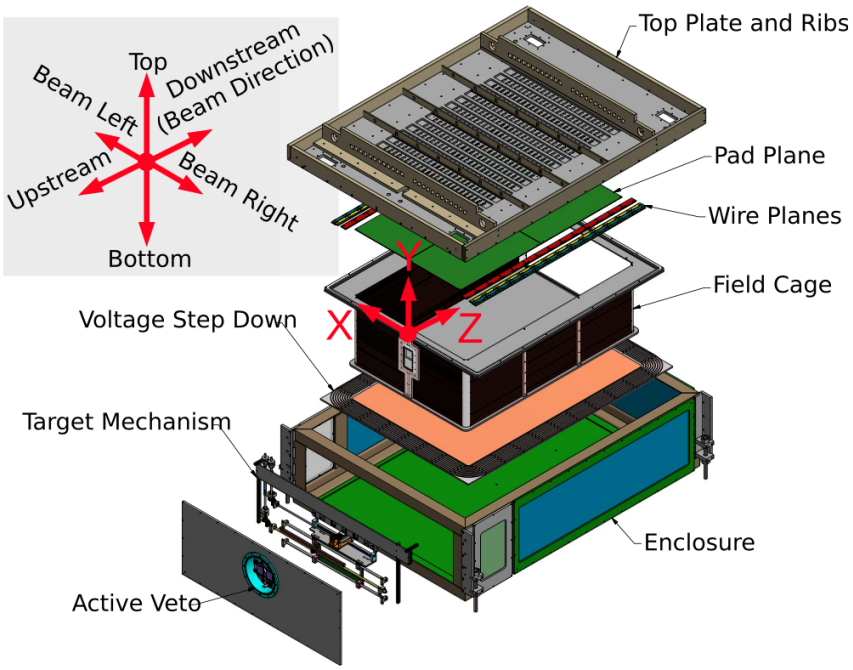

Figure 2.2 The exploded view of the SπRIT-TPC. Adopted from Ref. [8].

The field cage is filled with P10 gas (Ar 90% and CH_4 10%) at atmosphere pressure. The charged particles from the collisions will leave track inside the TPC by ionizing the gas and producing electrons. The cathode voltage was -6700 V, pro-

TPC properties	
Pad plane area	1344 mm × 864 mm
Number of pads	12096 (112 × 108)
Pad size	12 mm × 8 mm
Drift distance	∼ 500 mm
Gas composition	90 % Ar + 10 % CH_4
Gas pressure	1 atm
Gas gain	∼ 1000
Magnetic field	0.5 T
Electric field	124.7 V/cm
Electron drift velocity	∼ 5.5 cm/μs
Sampling rate	25 MHz
Shaping time	117 ns
ADC dynamic range	120 fC
ADC channels	4096
Typical track multiplicity	60
Typical electron dispersion	2 - 3 pads

Table 2.2 Main properties of SπRIT-TPC.

viding an electric field of 124.7 V/cm inside the field cage. The electric field drifts the electrons to the top of the TPC, where wire planes are placed. The drift velocity of the electron in such an environment was found to be around 5.5 cm/μs from the electron simulation using MAGBOLTZ [52]. The full drift length inside the field cage is $\sim$ 500 mm.

The wire plane consists of gating grid, ground, and anode wires from bottom to top. The gating grid wires can be switched to "closed" or "open", enabling electrons to block or pass through, respectively. For most of the time, the gating grid is "closed", where the voltages of the wires are staggered, and the gating grid wire absorbs electrons as a result. When the trigger condition is satisfied, the gating grid switch to the "open" configuration, and the same voltages are applied to all wires so that electrons will pass through. In between the ground and anode plane, electrons gain around 1000 times of charge from an avalanche between them. The electrons are terminated from the anode plane, and the positive ions produced from the avalanche region induce an image charge on the pad plane.

The signals created by the ions are read pad from pad plane. The pad plane consist 12096 (112 layers through z-axis $\times$ 108 rows through x-axis) pads with area of 1344 $\times$ 864 mm^2. The size of each pad is (z,x) = (12, 8) mm.

The SπRIT-TPC employs the Generic Electronics for TPC (GET). Fig. 2.3 shows an overview of the GET system applied for the SπRIT-TPC. The AGET chip can read 64 channels (pads) in total, and 63 channels were connected for SπRIT-TPC. The AGET chip has a 512 capacitor array where capacitors serve as charge storage in time. Four AGET chips are mounted on the AsAd board, where the analog signals are converted into the digitized signal, and pulse shaping is done. This data is sent to the Cobo board, where one Cobo board can control 4 AsAd boards. The Cobo board buffer data and the data are sent to the DAQ server when a trigger signal is sent. We used a sampling rate of 25 MHz, a dynamic range of 120 fC, and a shaping time of 117 ns.

The main properties are listed in the Table 2.2. The detail of SπRIT-TPC can be

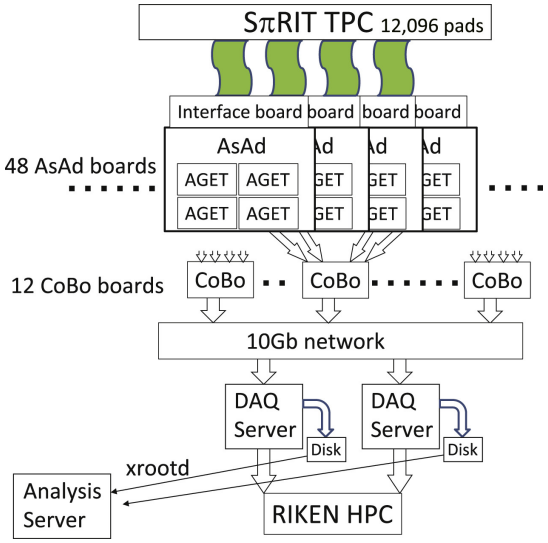

Figure 2.3 Adopted from Ref. [9].

found in Refs. [8, 9, 50, 53].

2.3 Ancillary Detectors

The Scintillation Beam Trigger (SBT) is a plastic scintillator with an areal dimension of 120 mm × 120 mm and 0.2 mm thickness. The SBT was placed 4.5 m upstream of the Sn target and triggered the event's start time.

The active veto array [54] was placed 22 cm upstream from the Sn target. The four scintillators with dimensions of 90 × 50 × 6 mm^3. The four scintillators were placed in four directions leaving the window in the path of the beam approximately 30 × 40 mm^2, regarding that beam hits the target. Therefore, the trigger signal from the active veto array means that beam did not hit the target and will not trigger the event.

The Kyoto multiplicity array is a multiplicity trigger detector [55] designed to measure the multiplicity from the collisions. The Kyoto multiplicity array was placed on both sides of the SπRIT-TPC, with each wall consisting of 30 plastic scintillator

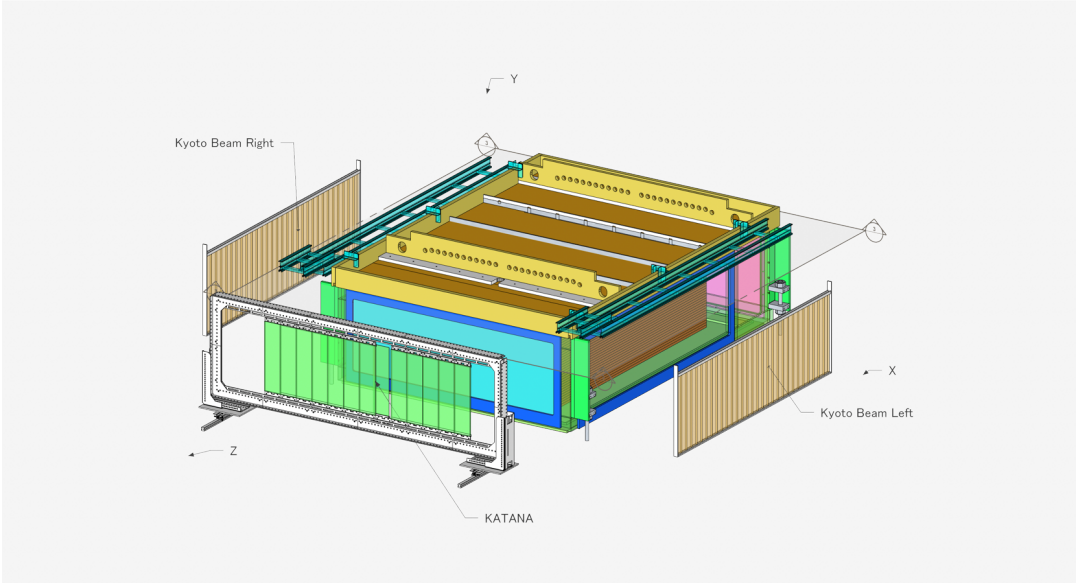

Figure 2.4 Exploded view of Kyoto multiplicity array and KATANA. Adopted from Ref. [10].

bars. Each scintillator bar has a size of 450 × 50 × 10 mm^3.

The Krakow Array for Triggering with Amplitude discrimiNAtion (KATANA) [56] was placed downstream of the TPC to trigger and veto events. The KATANA-Trigger is 12 thicker paddles having a dimension of 400 × 100 × 10 mm^3. It was used for the trigger, where seven were placed on the beam left, and five were placed on the beam right. One thinner paddle, KATANA-Veto, with a dimension of 400 × 100 × 1 mm^3, was placed between the two groups of thicker paddles. The position of KATANA-Veto was optimized to be in the passage of the beam, from the result of the GEANT4 simulation. If a Beam particle or fragment heavier than $Z = 20$, a veto signal is produced to protect the TPC.

The exploded view of the Kyoto multiplicity array and KATANA is shown in Fig. 2.4.

2.4 Glimps of the Events

The typical "good" events taken from the experiment are displaced from the top of the TPC in Fig. 2.5. Each grid corresponds to one pad, and the accumulated charge inside the pad is drawn in color as shown in the palette of z-axis. The tracks are mostly produced from the primary vertex. The primary vertex is placed upstream from the (z,x) = (0,0). The observed tracks are curved clockwise, as most are (+) charged particles. Negatively charged particles, such as electrons and pions, are also produced. The blank pads following the beam's trajectory can be observed due to the saturation of the charge in the pad. The multiplicity of the charged track is $\sim$ 50.

In Fig. 2.6, different events are seen from the side of the TPC. The charge is accumulated for time bins (shown as $y - axis$), and each layer of pads is drawn in the color corresponding to the charge value. The blank line around y = -25 mm (y = 0 mm is the pad plane on the top) shows the existence of a gating grid plane. The tracks going straight upward are created by delta electrons which is the leading cause for the saturation of pads and large dE/dx points, which is the reason for using truncated mean dE/dx of the track.

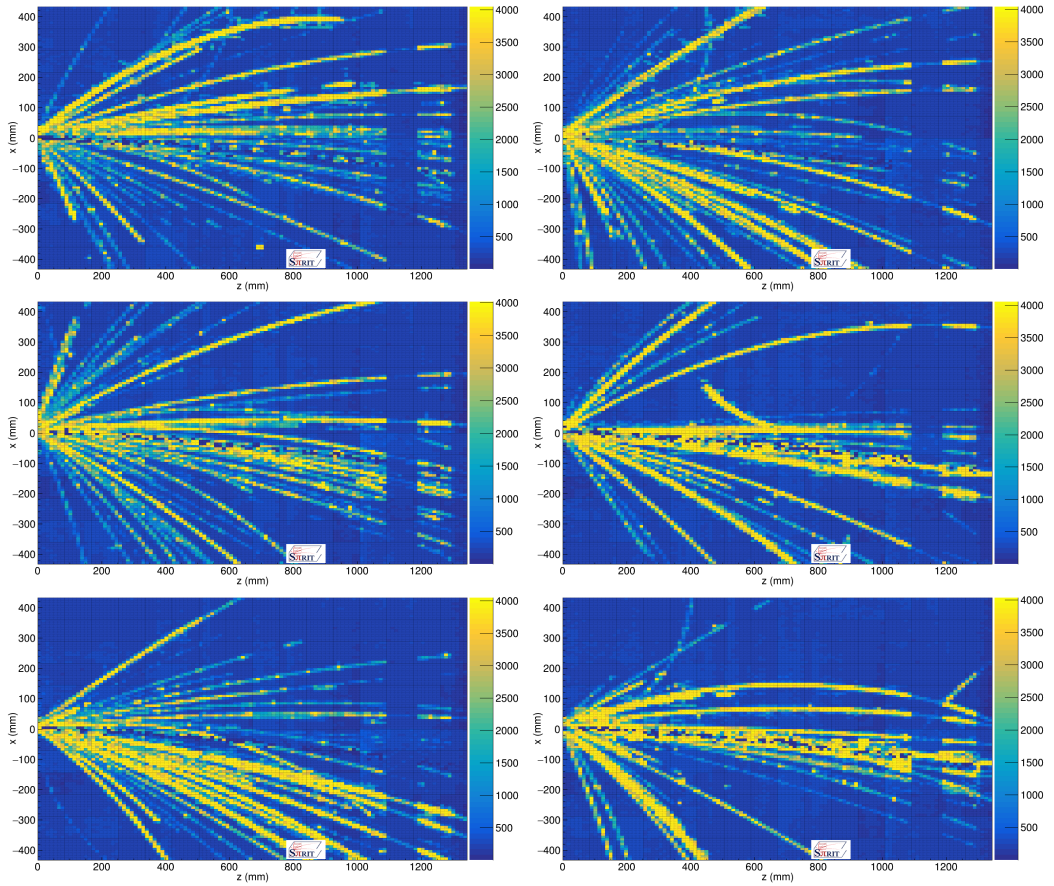

Figure 2.5 Examples of the SπRIT experiment events seen from the top of the TPC. The accumulated charge for each pad is drawn in color of z-axis.

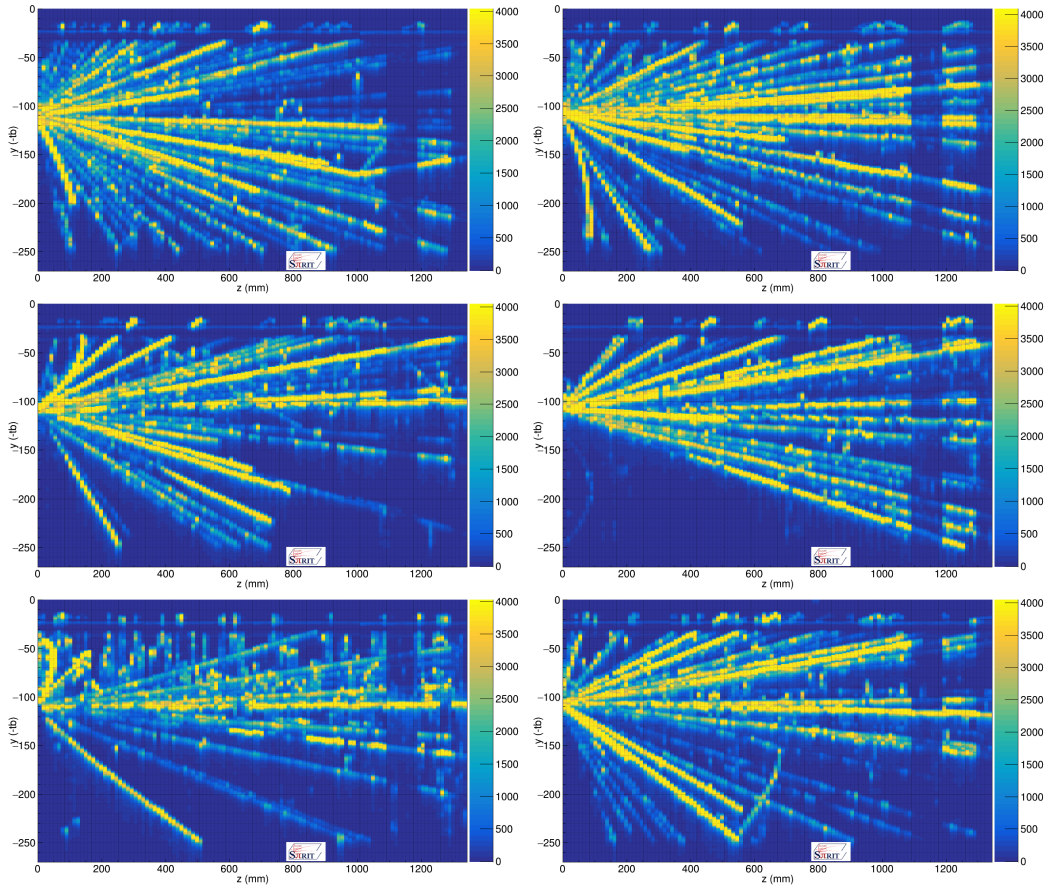

Figure 2.6 Examples of the SπRIT experiment events seen from the side of the TPC. The accumulated charge for time bins (drawn as y-axis) at each layer of pads are drawn in color of z-axis.

Chapter 3

The Reconstruction Software SpiRITROOT

SpiRITROOT is a software framework developed for the analysis and simulation of SπRIT-TPC experiments [57, 58, 59]. The basic frame is built on top of FairROOT [60] which provide a basic level framework for nuclear physics experiments. As the naming suggests, the FairROOT framework is written based on ROOT [61], the C++ library for large-scale data processing and analysis. SpiRITROOT is being managed by Git with main public repository in Ref. [57]. The analysis given in this thesis is produced from the SpiRITROOT version in Ref. [57].

3.1 Simulation and Digitization

The C++ package Geant4 [**?**] was used for the simulation of the SπRIT-TPC. Geant4 is a toolkit for the simulation of the passage of particles through matter which is widely used in the field of nuclear physics. For the simulation using Geant4, one should build a geometry리 of the detector with the material information and a physics process information called *Physics List*. A geometry of the detector can

be created using the ROOT as visualization is shown in Fig. 3.1 and a Physics List `QGSP_BERT_HP_EMY`, provided by Geant4 was used.

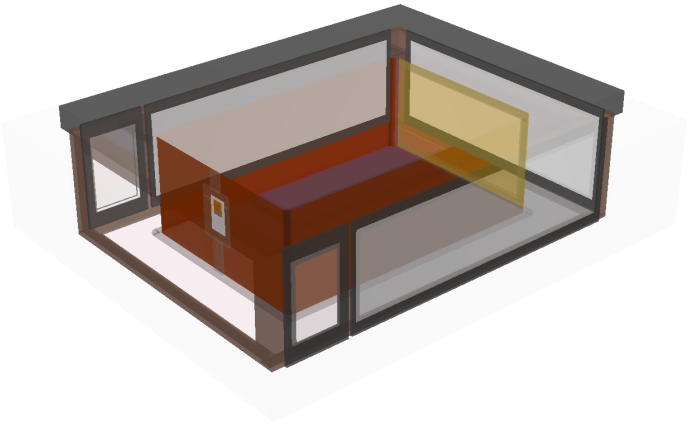

Figure 3.1 The geometry created from ROOT to be used in the Geant4 simulation.

To mimic the detector response, digitization tasks are written, which produce and drift electrons to the pad plane and simulate electronics. The simulation data are stored to charge-array in time for each TPC pad in a way experiment stores the data. Simulation data can share the same reconstruction and analysis flow of experimental data in this way.

As particle pass through the TPC in the simulation, the creation of electrons is omitted because simulation time increases exponentially when too many electrons are created. Instead, the number of electrons is calculated from the energy left by the particle inside the TPC using the mean ionization energy of the gas. The electrons will drift towards the pad plane ($+y$-direction for SπRIT-TPC). The time and position at which electrons arrive at the pad plane are calculated from the MAGBOLTZ simulation [52], using the properties of electrons drifting inside the gas, such as the drift velocity and diffusion coefficients. The diffusion of electrons in perpendicular ($\perp$) and parallel ($\parallel$) to the drift direction are defined by the Gaussian distribution

Drift velocity	5.5 cm/μs
Longitudinal diffusion coefficient $C_\perp$	0.034
Transversal diffusion coefficient $C_\parallel$	0.024

Table 3.1 Parameters of electron drifting inside the SπRIT-TPC.

with $\sigma_\perp$ and $\sigma_\parallel$ calculated from the drift length l_{drift} and coefficients $C_\perp$ and $C_\parallel$:

$$\sigma_\perp = C_\perp \sqrt{l_{\text{drift}}}, \tag{3.1}$$

$$\sigma_\parallel = C_\parallel \sqrt{l_{\text{drift}}}. \tag{3.2}$$

where the corresponding parameters for SπRIT-TPC are listed in the Table 3.1.

After the electrons arrive at the top of the TPC, the avalanche occurs as electrons pass through between the ground wire and the anode wire. This diffusion in this region is defined by the Gatti distribution [62]:

$$\frac{\rho(\lambda)}{q_a} = K_1 \frac{1 - \tanh^2(K_2\lambda)}{1 + K_3 \tanh^2(K_2\lambda)}, \tag{3.3}$$

where

$$K_1 = \frac{K_2\sqrt{K_3}}{4\tan^{-1}\sqrt{K_3}} \tag{3.4}$$

and

$$K_2 = \frac{\pi}{2}\left(1 - \frac{\sqrt{K_3}}{2}\right). \tag{3.5}$$

Here $\lambda = x/h$ where x is the distance from the avalanche center, h is the separation of anode and cathode, and q_a is the net anode charge. The K_i (i=1,2,3) are the geometric parameters, and the corresponding parameters for SπRIT-TPC are listed in Table 3.2 for each avalanche direction. The typical number of pads in the width of the track created by diffusion and avalanche is 2 - 3.

The electron distribution convoluted with the Gatti distribution is integrated for

	K_1	K_2	K_3
x-direction	0.29	0.99	0.55
z-direction	0.28	0.95	0.62

Table 3.2 The Gatti distribution parameters for SπRIT-TPC.

each pad in the pad plane and filled as an array of time buckets where a one-time bucket corresponds to 40 ns. For each time bucket, the reference pulse of Fig. 3.2, which will be explained in the next section, is drawn. The sum of these pulses becomes the final output of the pads in the digitization flow.

3.2 Event Reconstruction

3.2.1 GETDecoder

The SπRIT-TPC employs the newly developed Generic Electronics system for Time Projection Chamber [9, 63] and unpacking software GETDecoder for SπRIT-TPC was developed, which takes advantage of time and disk space. See Reference [64] for the detail.

3.2.2 Pulse analysis

The pulse shape from the single track is fixed regardless of the particle type, drift length, and data type (i.e., cosmic data or nuclear collision data). We extracted the standard shape of the pulse from the pads containing the single track. The chosen pulse amplitude range was from 1000 to 3000 ADC channels. The peak amplitude of each pulse was normalized to one, and the peak position in time was aligned to an arbitrary reference time. The average ADC points create a reference pulse shape, $f(\mathrm{tb})$. This pulse shape is used to fit pulses with time and amplitude parameters. The sketch of the reference pulse is shown in Fig. 3.2. The start of the reference pulse is defined as the tb at 5% of the pulse height. The peaking time, describing the

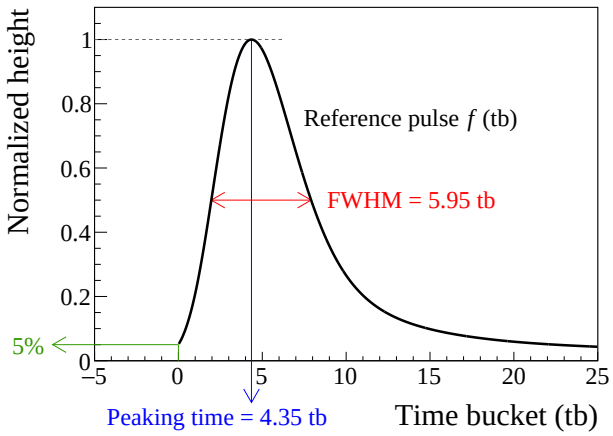

Figure 3.2 The reference pulse shape $f(\mathrm{tb})$ is extracted from the experiment data. The start of the reference pulse is defined as the 5% of the pulse height. The peaking time describing the time duration to reach the maximum height of the pulse, is 4.35 tb. The Full Width Half Maximum (FWHM) of the pulse is 5.95 tb.

time duration to reach the maximum height of the pulse, is 4.35 tb which is 174 ns in real-time, and 9.53 mm by applying the electron drift velocity. The Full Width Half Maximum (FWHM) of the pulse is 5.95 tb ($\simeq$ 238 ns $\simeq$ 13.19 mm).

The pulse shape analysis steps are shown in Fig. 3.3. The pulse shape analysis starts by finding the peak above the threshold from the earliest time buckets. Therefore, the pulses are reconstructed from the earlier time to the latter time. When the peak is found, the single pulse χ^2-fit is performed as shown in Fig. 3.3(a). For the pulse fit, we use the reference pulse $w_i f(\mathrm{tb} - \mathrm{tb}_i)$ where w_i and tb_i is the hit charge (amplitude) and the hit time (tb-axis position) respectively. The fit range is focused on the peaking time range, which is about 5-time buckets. After the pulse fit is performed, the fit function is subtracted from the data: Fig. 3.3(b). This process is repeated in Fig. 3.3(b)$\sim$(d) until no peaks arise above the threshold as shown in Fig. 3.3(e). The final result of pulse shape analysis is the sum of all single pulse fits: Fig. 3.3(f).

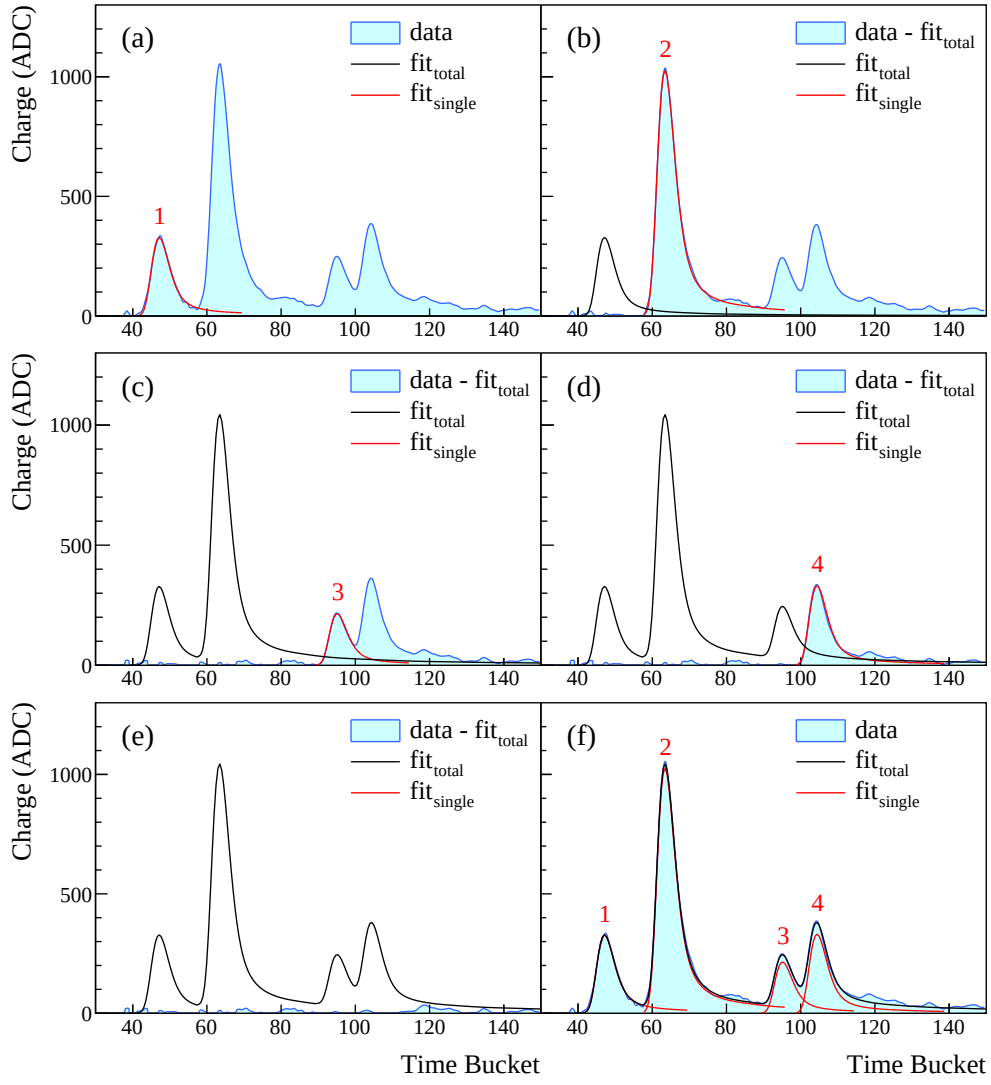

Figure 3.3 The pulse shape analysis steps from the charge spectrum are shown. For each panel, the sum of previously fitted pulses ($\text{fit}_{\text{total}}$) is drawn in black, the data subtracted by $\text{fit}_{\text{total}}$ is shown as a filled histogram, and the single pulse fits are drawn in red with pulse index ($\text{fit}_{\text{single}}$). A detail of the process is written in the text.

3.2.3 Hit reconstruction efficiency

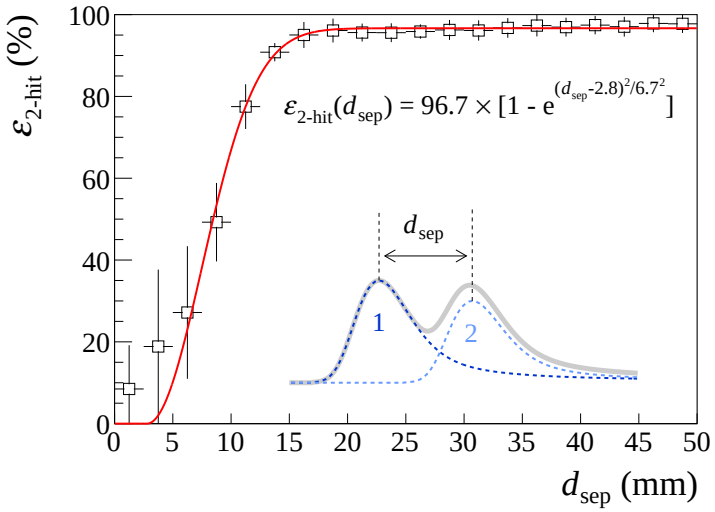

Figure 3.4 Two hit separation efficiency $\epsilon_{2\text{-hit}}$ plotted as a function of the separation distance d_{sep}. The data (square) is fitted with Eq. 3.8 (red) to guide the eye, and the fit equation is shown. The region for $d_{\text{sep}} \leq 20$ mm shows a significant variance in efficiency while the region for $d_{\text{sep}} > 20$ mm is saturated. The definition of separation distance d_{sep} is drawn with the two pulses in the lower right corner.

The single hit finding efficiency of Eq. 3.6 is calculated using the Monte-Carlo simulation. From the simulation, we count the number of pads where the track passes through directly, n_{total}, and compare it with the number of reconstructed hits, which is reconstructed to a track, n_{reco}. The single hit finding efficiency is $\epsilon_{1\text{-hit}} = 95 \pm 1\,\%$ from this calculation.

$$\epsilon_{1\text{-hit}} = \frac{n_{\text{reco}}}{n_{\text{total}}}. \tag{3.6}$$

By checking for reconstructed hits of two track events, we can count the number of pads which reconstruct both hits, $n_{1,2}$, and the total number of pads with two

track events, $n_{\text{2-track}}$. The two-hit separation efficiency is then defined as

$$\epsilon_{\text{2-hit}} = \frac{1}{\epsilon_{\text{1-hit}}} \times \frac{n_{1,2}}{n_{\text{2-track}}}. \tag{3.7}$$

Again from the simulation, we chose pads that only the two tracks pass through. Now we define the y-axis positions of the hits created from the two tracks as y_1 and y_2, where $y_1 > y_2$. The difference between y_1 and y_2 is the hit separation distance, $d_{\text{sep}} = y_1 - y_2$. The two-hit separation efficiency of Eq. 3.7 is estimated as a function of the hit separation distance between two consecutive pulses, d_{sep}, and is shown in Fig. 3.4. The data in Fig. 3.4 is fitted with

$$\epsilon_{\text{2-hit}} = \epsilon_{\text{max}} \left(1 - \exp \frac{-(d_{\text{sep}} - d_0)^2}{\delta_d^2} \right), \tag{3.8}$$

where ϵ_{max} is saturation efficiency, and d_0 and δ_d are the fit parameters. The efficiency saturates to $\epsilon_{\text{max}} = 96.7\,\%$ and the average efficiency error of the data points in the saturated region ($d_{\text{sep}} > 20$) was found to be 2.3 %. This error of efficiency comes from the uncertainty in the reference pulse shape from different track angles. For example, a larger track angle will create a wider distribution of electrons along the time axis and result in a broader pulse shape. On the other hand, a track parallel to the pad plane will create a narrower distribution of electrons along the time axis and result in a standard pulse shape with better efficiency. The pulse height difference is another cause, as the second pulse, with a smaller height compared to the first, has a chance that it will be recognized as a part of the first pulse.

3.3 Helix Track Finding Task

The events from the SπRIT experiment typically produce 30 to charged particles that leave tracks inside the TPC. The magnetic field produced by the SAMURAI magnet cause particles going through TPC to leave helical tracks. These tracks are

recognized as individual tracks in the helix track finding task using the hits collected from the PSA task. Apart from the algorithm, two methods, the Riemann circular fit method and a Point Of Closest Approach (POCA), which are the two main methods used, will be introduced in this section.

3.3.1 The helix track parametrization

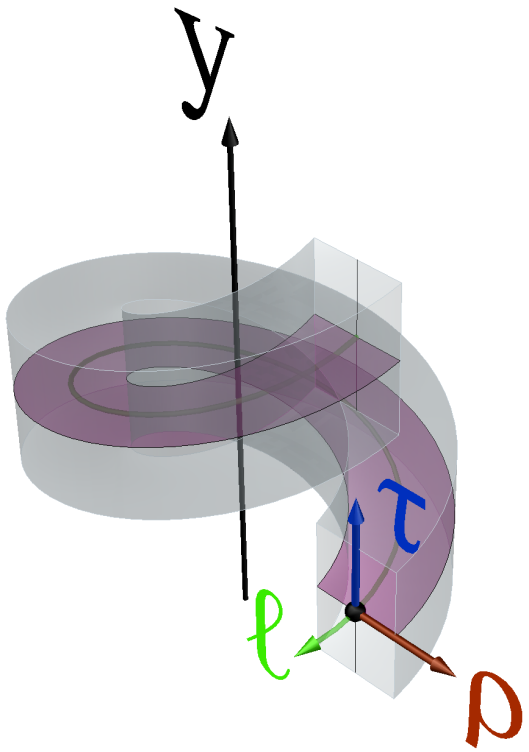

Figure 3.5 The figure explaining the helical axis defined for the helix track. See the text for detail.

The helix track describes the ideal trajectory of charged particles inside the magnetic field. An idea of the helix parametrization is shown in Fig. 3.5:

- Helix center $\boldsymbol{x}_{\mathrm{h}} = (x_{\mathrm{h}}, z_{\mathrm{h}})$ of the circle projected onto the pad plane,
- Helix radius R_{h} of the projected circle,
- Polar angle of the helix α being the parametric angle defining the x and z

values (values at the two end points of the helix are defined as $\alpha_{\rm tail}$ and $\alpha_{\rm head}$, respectively):

$$x = R_{\rm h}\cos\alpha + x_{\rm h}, \tag{3.9}$$

$$z = R_{\rm h}\sin\alpha + z_{\rm h}, \tag{3.10}$$

- Slope parameter $s_{\rm h}$ and y-offset $y_{\rm h}$, which describe the linear relation between the polar angle α and the y-position of the helix:

$$y = s_{\rm h}\alpha + y_{\rm h}, \tag{3.11}$$

- The track window Δ_ρ and Δ_τ of the two axis ρ and τ, which are described below.

The dip angle describing the angle between the track momentum and the pad plane is defined by

$$\theta = \arctan\left(\frac{s_{\rm h}}{R_{\rm h}}\right). \tag{3.12}$$

The helicoid coordinate is employed as shown in Fig. 3.5. The first axis is the radial axis $\hat{\boldsymbol{\rho}}$ from the helix center, the second axis $\hat{\boldsymbol{\ell}}$ follows the helix path, and the last axis $\hat{\boldsymbol{\tau}}$ is normal to both $\hat{\boldsymbol{\ell}}$ and $\hat{\boldsymbol{\rho}}$. The $\hat{\boldsymbol{\rho}}$ and $\hat{\boldsymbol{\tau}}$ axes will be used as the axis defining the width and height of the track, respectively. The transformation of the point $\boldsymbol{x}_{\rm i}$ at corresponding $\alpha_{\rm i}$ is given by

$$\rho_{\rm i} = R_{\rm i} - R_{\rm h}, \tag{3.13}$$

$$\tau_{\rm i} = \delta y_{\rm i}\sec\theta, \tag{3.14}$$

$$\ell_{\rm i} = \alpha_{\rm i}R_{\rm h}\sec\theta + \delta y_{\rm i}\sin\theta, \tag{3.15}$$

where $R_{\rm i} = \sqrt{(x_{\rm i}-x_{\rm h})^2 + (z_{\rm i}-z_{\rm h})^2}$ and $\delta y_{\rm i} = y_{\rm i} - s_{\rm h}\alpha_{\rm i} + y_{\rm h}$.

Now let us assume a point $(x, y, z)_{\rm i}$ which can be transformed into $(\rho, \tau, \ell)_{\rm i}$, and

find the point on a helix where the distance becomes minimum. Such a point on a helix is called the Point Of Closest Approach (POCA). We approximate POCA to $(\rho, \tau, \ell)_{\mathrm{POCA}} = (0, 0, \ell_{\mathrm{i}})$. In this definition, ρ_{i} and τ_{i} correspond to the shortest distance from the track in $\hat{\boldsymbol{\rho}}$ and $\hat{\boldsymbol{\tau}}$ axis, respectively. For the use in track finding algorithm, we define the "hit collecting window" of the helix track as root mean square of hit residuals $\mathrm{res}(\rho)_{\mathrm{track}}$ and $\mathrm{res}(\tau)_{\mathrm{track}}$ as given below. These RMS values typically range from 1 to 5 mm.

$$\Delta_{\rho} = 3.5 \times \sqrt{\sum_{\mathrm{hit}} \mathrm{res}(\rho)^2_{\mathrm{hit}}}\,, \tag{3.16}$$

$$\Delta_{\tau} = 3.5 \times \sqrt{\sum_{\mathrm{hit}} \mathrm{res}(\tau)^2_{\mathrm{hit}}}\,. \tag{3.17}$$

3.3.2 The helix track finding

Typically the collision events in the SπRIT-TPC have a high track density around the target position, whereas, at the far side of the TPC, the track density is much lower due to the outgoing emission angles and the presence of the magnetic field that separates the tracks by their magnetic rigidity. The challenging task of event reconstruction can be simplified by starting the tracking at the end of the tracks and iteratively working back toward the collision vertex.

The flow chart of the track-building algorithm is shown in Fig. 3.6. For the first step, the event map containing all reconstructed hits is created. The event map is sophisticated in that for a given position, it will find the corresponding pad and its neighboring pads, where each of those pads contains reconstructed hits.

The hits are classified into three groups:

1. free-hits, which have not participated in track building,
2. used-hits, which participate in track building, and
3. track-hits, which have been collected as part of a track.

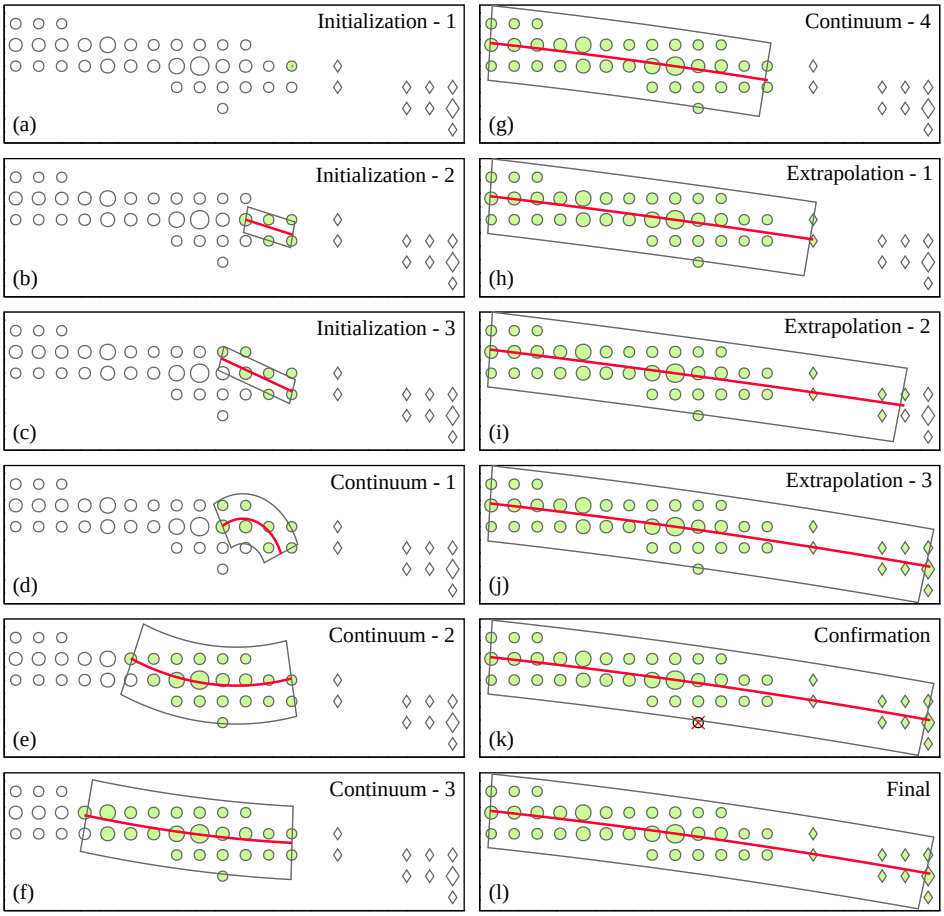

Figure 3.6 Flow chart of the track building algorithm with each panel showing an example track evolution. The example cartoons demonstrate the case of a successful build of the track. The used-hits are shown as empty diamonds, free-hits are shown as an empty circle, and the track-hits are shown as green circle markers. The used-hits originate from the earlier track buildings that have failed. The track-hits, belong to the track being built, which are fitted with a straight line in the initialization stage (a)∼(c) and fitted with helical parametrization for the other stages (d)∼(l). The area surrounded by the solid line shows the track window Δ_ρ. The initialization stage and continuum stage (a)∼(g) collect hits from the neighbors of track-hits. While track hits are collected from the extrapolation point of the track-fit in the extrapolation stage (h)∼(j). (k) In the Confirmation stage, the hits (red cross) outside the track window Δ_ρ are removed from the track.

All hits are flagged as a free-hit by default. The hits collected during the track building are flagged as a track-hit. After a track is successfully built, track-hits are removed from the event map. If the track-building fails, track-hits are returned to the event map and flagged as used-hit. This type of flag is essential to prevent track building from starting in the island of isolated hits which cannot develop into a track: e.g., the island of diamond markers in Fig. 3.6.

In this track-building algorithm, only one track is built at a time. The track's first hit is given with the farthest hit from the target among free-hits in the event-map. The track is then built through four stages:

1. *Initialization* stage,
2. *Continuum* stage,
3. *Extrapolation* stage, and
4. *Confirmation* stage.

In each stage, candidate hits are searched from the neighboring pads and pads at extrapolated points. If a candidate hit falls into the track window $\Delta_{\rho,\tau}$, the hit is added to the track, and the track parameters are updated by track fitting.

In the *Initialization* stage, hits from neighboring pads are collectedand the track length is calculated with the linear fit of the track.This stage fails if the track length is smaller than $2.5 \times \mathrm{RMS}(\rho)_{\mathrm{track}}$ with at most 15 hits. In the *Continuum* stage, all hits from neighboring pads that fit into the track window $\Delta_{\rho,\tau}$ are added. The area surrounded by the dotted line in Fig. 3.6 shows the range of track window Δ_{ρ}. The radius of the helix must be larger than 25 mm at the end of this stage. The *Extrapolation* stage works in the same way as the *Continuum* stage, but the candidate hits are added by extrapolating the track across regions where there may be no hits until the track extrapolation reaches the boundary of TPC volume. Discontinuities in the track can be caused by low-gain regions or saturated regions where little to no charge was extracted, resulting in a broken track. Finally, in the *Confirmation* stage,

the hits are compared with the helix parameter set until no more hits are removed or added. After a track is built, a new cycle begins with the remaining free-hits in the event-map. The process is repeated until the event-map no longer contains free-hits.

3.3.3 Helix fit via Riemann fit

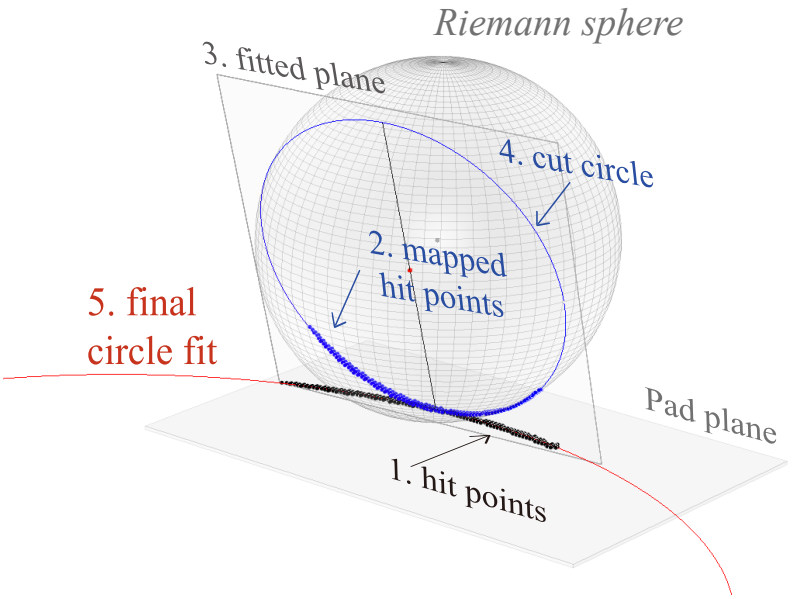

Figure 3.7 The steps of the Riemann fit process are shown with the Riemann sphere sitting on the pad plane. Firstly, the black hit points (1) on the pad plane are projected onto the Riemann sphere surface, as shown by the blue points (2). Next, a plane is fitted to the projected points (3). The intersection of the Riemann sphere and the fit plane defines the blue circle (4). Finally, the blue circle is projected back to the pad plane, resulting in the red circle line (5).

The helix parameters introduced in Section3.3.1 are used in many places throughout the software. Section 3.3.6 will show that the guideline of hit clusterization is based on the path and direction of the track. Also, the parameters used as the initial values of momentum tracks are fitted with GENFIT. Most importantly, updating the track window is required in every track-building step, which is why the helix fit is

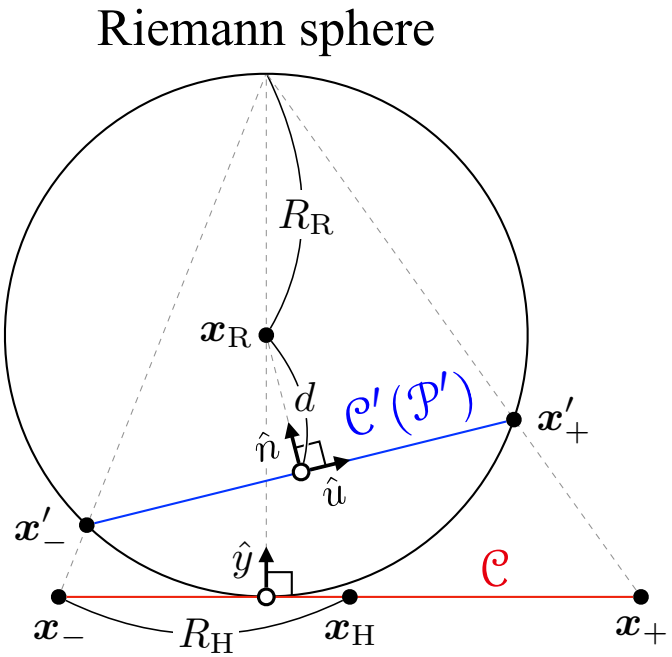

Figure 3.8 A cross-section of the Riemann sphere and the components used to evaluate the helix parameters in the plane of $\hat{\boldsymbol{n}}$ and $\hat{\boldsymbol{u}}$. The circle fit of the original hit distribution $\mathcal{C}$ is shown in red The circle $\mathcal{C}'$ defined by the intersection of the Riemann sphere and plane $\mathcal{P}'$ is shown in blue. The inverse projection of points $\boldsymbol{x}'_\pm$ to $\boldsymbol{x}_\pm$ are indicated.

crucial in this software.

In this section, we describe helix fit via Riemann circle fit, which can find the three circle parameters $\boldsymbol{x}_{\mathrm{h}} = (x_{\mathrm{h}}, z_{\mathrm{h}})$ and R_{h} among the helix parameter set. The slope and offset parameters s_{h} and y_{h} can be determined with a standard linear fit, and the remaining parameters, the polar angles at the end of the helix (α_{head} and α_{tail}), can be found with the POCA method.

The χ^2 fit of the circle is known as a non-linear problem. We simplify the problem by implementing the so-called Riemann circle fit [65, 66]. This method uses the fact that the plane fit is a linear problem and that the circle in the pad plane uniquely maps onto a circle on the sphere. The circle on a sphere uniquely defines a plane which can be solved by Orthogonal Distance Regression (ODR) method. The sphere used in the Riemann circle fit, which sits right on top of the pad plane, is called the Riemann sphere. Figure 3.7 shows the exact steps of the Riemann circle fit.

The center and radius of the Riemann sphere are chosen to be $\boldsymbol{x}_{\mathrm{R}} = \langle \boldsymbol{x} \rangle_{\mathrm{hit}} + R_{\mathrm{R}}\, \hat{\boldsymbol{y}}$ and $R_{\mathrm{R}} = 2\boldsymbol{\sigma}^2_{\mathrm{hit}}$, respectively. Here, $\langle \boldsymbol{x} \rangle_{\mathrm{hit}}$ and $\boldsymbol{\sigma}^2_{\mathrm{hit}}$ are the mean and variance of the hit position in the pad plane, respectively. These parameters are chosen so that the projected points are widely distributed on the sphere's surface.

The fit starts by mapping data points onto the Riemann sphere by stereographic projection. The intersection of the sphere and line connecting the hit to the north pole of the sphere defines the projected points $\boldsymbol{x}_{\mathrm{map}}$, which can be written as

$$\boldsymbol{x}_{\mathrm{map}} = \frac{\left([x_{\mathrm{hit}}]\,,\ \frac{r^2_{\mathrm{eff}}}{2R_{\mathrm{R}}},\ [z_{\mathrm{hit}}] \right)}{1 + r^2_{\mathrm{eff}}} + \langle \boldsymbol{x}_{\mathrm{hit}} \rangle\,, \tag{3.18}$$

with mean-subtracted position $[\boldsymbol{x}] = \boldsymbol{x} - \langle \boldsymbol{x} \rangle$ and effective radius

$$r_{\mathrm{eff}} = \frac{\sqrt{[x_{\mathrm{hit}}]^2 + [z_{\mathrm{hit}}]^2}}{2R_{\mathrm{R}}}.$$

As the next step, a plane is fitted to the points on the Riemann sphere. The

solution is given by solving the eigenvalues and eigenvectors of the matrix

$$\boldsymbol{A} = \sum_{i}^{N_{\rm hit}} \boldsymbol{X}_i^{\rm T} \boldsymbol{X}_i, \tag{3.19}$$

where $\boldsymbol{X}_i = \sqrt{q_i}\,(\boldsymbol{x}_{{\rm map},i} - \langle \boldsymbol{x}_{\rm map} \rangle)$ with hit charge q. By choosing the smallest eigenvalue, the corresponding eigenvector becomes the normal vector $\hat{\boldsymbol{n}}$ of the fit-plane $\mathcal{P}'$ defined by $\hat{\boldsymbol{n}} \cdot \boldsymbol{x} = k$, where k is the distance from the origin to the plane $\mathcal{P}'$. The cross-section of the Riemann sphere and plane $\mathcal{P}'$ defines a cut circle $\mathcal{C}'$.

The circle fit of the original hit distribution $\mathcal{C}$ is found by the inverse projection of a circle $\mathcal{C}'$. The sketch of the inverse projection is shown in Fig. 3.8 to explain the geometrical meaning of each component in the paragraph. We start by finding the highest-y point $\boldsymbol{x}'_+$ and lowest-y point $\boldsymbol{x}'_-$ of a circle $\mathcal{C}'$. The inverse projection of these two points $\boldsymbol{x}_\pm$ defines the endpoints of the line that becomes the diameter of the circle $\mathcal{C}$. Since the two eigenvectors $\hat{\boldsymbol{l}}$ and $\hat{\boldsymbol{m}}$ from the first and second largest eigenvalues of matrix $\boldsymbol{A}$ always lie in the plane $\mathcal{P}'$, a unit vector $\hat{\boldsymbol{u}}$ pointing from the center of the circle $\mathcal{C}'$ to $\boldsymbol{x}_+$ is found by

$$\hat{\boldsymbol{u}} = \frac{1}{\sqrt{l_y^2 + m_y^2}} \left(l_y\, \hat{\boldsymbol{l}} + m_y\, \hat{\boldsymbol{m}} \right). \tag{3.20}$$

Therefore, the points $\boldsymbol{x}'_\pm$ and $\boldsymbol{x}_\pm$ are written as

$$\boldsymbol{x}'_\pm = \boldsymbol{x}_{\rm R} - d\hat{\boldsymbol{n}} \pm \sqrt{R_{\rm R}^2 - d^2}\,\hat{\boldsymbol{u}}, \tag{3.21}$$

$$\boldsymbol{x}_\pm = \frac{1}{1 - y'_\pm / 2R_{\rm R}} \left(x'_\pm, 0, z'_\pm \right), \tag{3.22}$$

where d is the distance from the center of the Riemann sphere to the plane $\mathcal{P}'$;

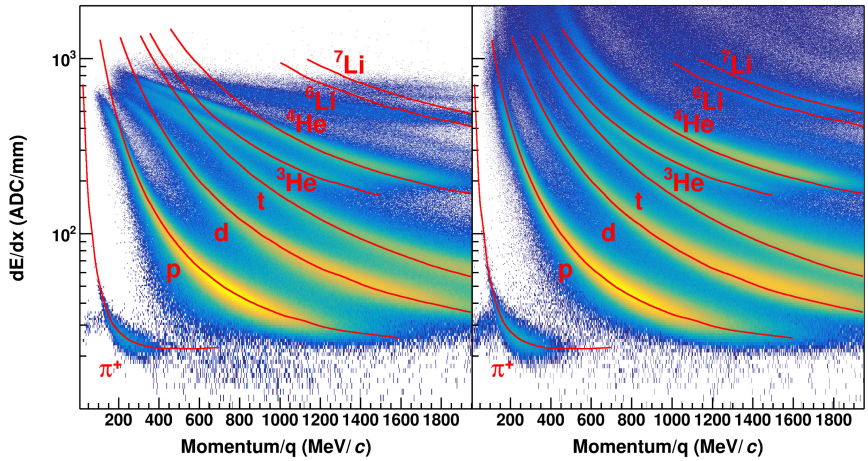

Figure 3.9 PID plot ($\langle dE/dx \rangle$ vs p/Z before (left panel) and after (right panel) de-saturation correction. Adopted from Ref. [11].

$d = |\hat{\boldsymbol{n}} \cdot \boldsymbol{x}_{\mathrm{R}} - k|$. Finally, the helix parameters defined as

$$R_{\mathrm{h}} = |\boldsymbol{x}_{+} - \boldsymbol{x}_{-}|/2, \tag{3.23}$$

$$\boldsymbol{x}_{\mathrm{h}} = (\boldsymbol{x}_{+} + \boldsymbol{x}_{-})/2. \tag{3.24}$$

3.3.4 De-Saturation correction

Although the dynamic range of the SπRIT-TPC was designed to cover from pions to Helium isotopes, the low energy tracks create a large amount of charge that can be covered. This limit can be seen in the left panel of Fig. 3.9, where the extrapolation of the Bethe-Bloch formula in the low rigidity region disagrees with the data. This effect was corrected from the pad response level, where the saturated pad has a pulse shape and a cut in the neck. The charge of the saturated pulse is recovered from the pads around them, which are not saturated. The charge distribution is fitted with the experimental pad response function fixed by the anode wire geometry. The PID plot recovered by this method is shown in the right panel of Fig. 3.9. The details can be found in Ref. [11].

3.3.5 E × B Correction

In the experiment, beams hardly not collide on the target. These beams passing through the TPC create many electrons and ions along the beam trajectory. The electrons drift to the top of the TPC while the ions drift down to the bottom of the TPC. The drift velocity of ions, however, is slower than electrons, and they are accumulated through time to create a space charge effect. The distortion of the E-field by space charge is minor but enough to move drifting electrons side-way and resulting the cluster position being off from the original position. The space charge effect was evident from the data, where the distribution of x-difference from track to vertex was separated and the difference of peak value was almost 10 mm when data from the left and right sides of the beam were compared. The space charge effect was corrected by solving the Langevin equation to restore the cluster position to the original position. The details can be found in Ref. [67].

3.3.6 The Hit clusterization

The mean value of the hit distribution perpendicular to the track's trajectory gives the best estimate of the center of the track. Although the pad size is only 7.5 mm × 11.5 mm, we can significantly improve the position resolution, which is needed to reconstruct accurate momentum, by grouping clusters of hits together, either in the same row (row-cluster) or in the same layer (layer-cluster).

The classification of clusters is determined from the crossing angle of the track ξ. The crossing angle is defined as the angle between track momentum and z-axis as shown in Fig. 3.10:

$$\textbf{row-cluster}: \quad 45^\circ < |\xi| < 135^\circ, \tag{3.25}$$

$$\textbf{layer-cluster}: \quad |\xi| < 45^\circ, \quad |\xi| > 135^\circ. \tag{3.26}$$

The hit cluster charge, the sum of hit charges, gives Q. The hit cluster position (along

the direction of clustering) is determined by averaging charge-weighted positions of each hit in the cluster; the perpendicular coordinate is set to the center of the pad. For example, if hits are being clustered in a layer (x-direction), the x-position is the weighted mean value of the hits, and the z-position is set to the z-position of the center of that layer, and vice versa for row clustering.

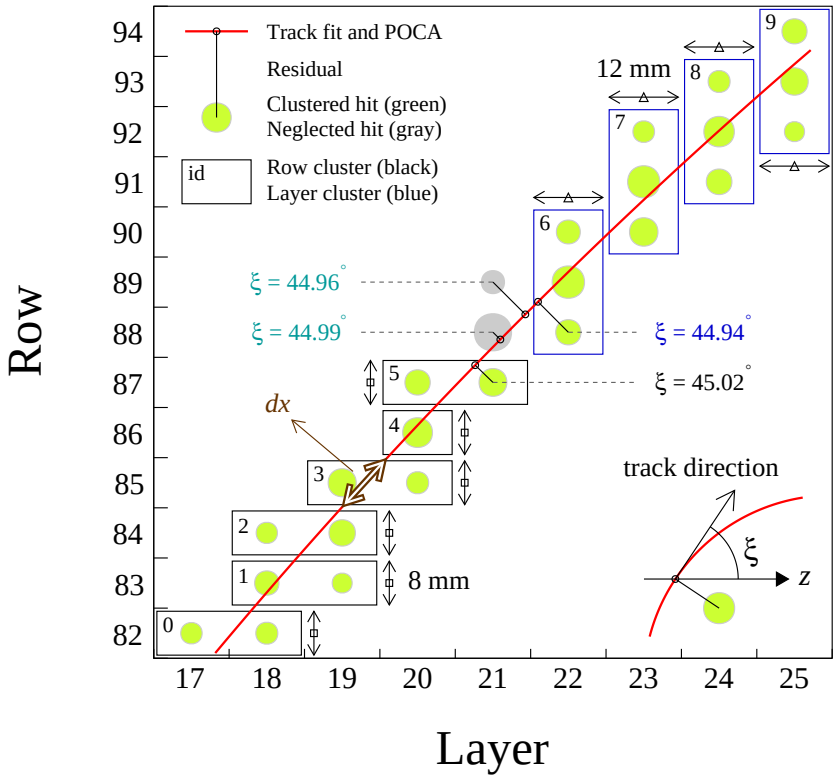

Figure 3.10 An example track (red line) creates clusters of two different types; row-cluster and layer-cluster in black and blue rectangles. The cluster participant hits are shown in green circles, with the size of the circle proportional to the charge of the hit. The hits which could not create any clusters are colored in gray. The number on the top left corner of the cluster denotes the index of the clusters. The corresponding crossing angle ξ of the hits is defined as a cartoon in the lower right corner. See the text for detail.

The position error of each cluster was estimated from the residual distribution,

the cluster's position to the position of the reconstructed track. The errors can be written separately depending on the type of hit clusters as given in Eqs. 3.27 and 3.28.

$$\boldsymbol{\sigma}_{\text{row}} = (0 \text{ mm},\ \sigma_y(\theta),\ \sigma_{\text{row},z}(\xi))\,, \tag{3.27}$$

$$\boldsymbol{\sigma}_{\text{layer}} = (\sigma_{\text{layer},x}(\xi),\ \sigma_y(\theta),\ 0 \text{ mm})\,. \tag{3.28}$$

The error in a cluster's position mainly depends on the dip angle θ and the crossing angle ξ, which are shown in Fig. 3.11. The effect of electron diffusion is expected to be enhanced at large θ because the effect on neighboring pads increases the width of the pulse shape. The same effect is expected for ξ as it approaches the angle $|\xi| = 45°$ and $|\xi| = 135°$ because hit clusters are formed in the plane of $\xi = 0°$ for row-clusters and $\xi = 90°$ for layer-clusters. The components $\sigma_{\text{row},x}$ and $\sigma_{\text{layer},z}$ are defined to be 0 mm because the track fit is performed in the plane normal to the x-axis for row-clusters and normal to the z-axis for layer-clusters.

The energy loss per unit length, dE/dx (ADC/mm), can be calculated for each hit cluster used for the particle identification analysis. The energy loss dE is defined as the hit cluster charge Q, and the length dx is calculated from the path length of the track in the cluster box range as shown in Fig. 3.10.

Fig. 3.10 shows an example of the track (red line) creating clusters of two different types. The row-cluster and layer-cluster are shown in black and blue rectangles, respectively. The cluster participant hits are shown in green circles. The size of the circle is proportional to the charge of the hit. The hits that could not create any clusters are colored in gray. The number on the top left corner of the cluster denotes the index of the clusters. The corresponding crossing angle ξ of the hits is defined as a cartoon on the lower right corner. Row-clusters are created from hits with $\xi > 45°$ (cluster (0) to (5)), and layer-clusters are created from hits with $\xi < 45°$ (cluster (6) to (9)). Note that the cluster's depths are 8 mm for row-cluster and 12 mm for layer-cluster. Since the last row-cluster (5) and the first layer-cluster (6) should not

share the same row or layer of pad, two hits (gray circles) in-between are neglected from the clusterization. The definition of the track length dx of the cluster is drawn above cluster (3) as an arrow.

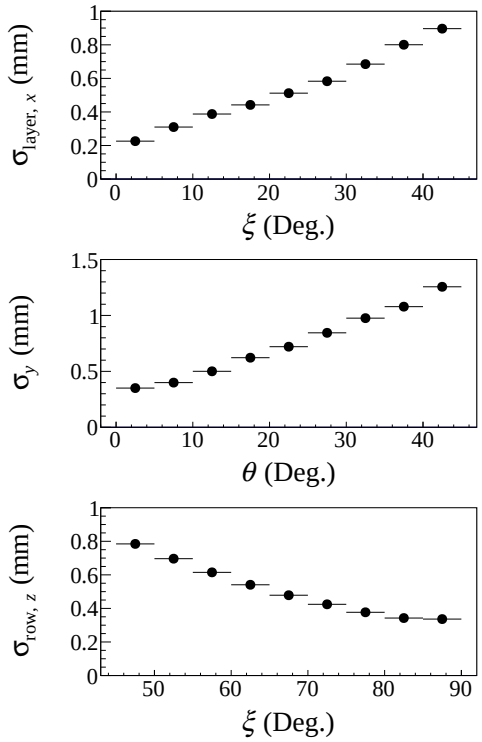

Figure 3.11 Position errors of a hit cluster as functions of the dip angle θ and the crossing angle ξ. It shows that σ_y constantly increases as θ increases. In addition, $\sigma_{\mathrm{layer},x}$ and $\sigma_{\mathrm{row},z}$ become larger as ξ gets close to 45°.

3.3.7 Momentum reconstruction

The momentum reconstruction is performed on the hit clusters using GENFIT [68]. GENFIT can perform fits on the hit clusters in 3-dimensions with a Kalman fitter algorithm [69], stepping through the various materials while calculating the energy loss and next point along the way leading to momentum reconstruction. The hit cluster position and its error, gas properties, and magnetic field map are provided as

input.

We can evaluate the transverse momentum resolution using a cocktail particle beam of deuterons and tritons at momentum around 1700 MeV/c taken during the experiment. The resolution is 1.5 % for deuterons and 2 % for tritons, as shown by the symbols in Fig. 3.12. The measured resolution is very close to the predicted values, as shown by the solid curves.

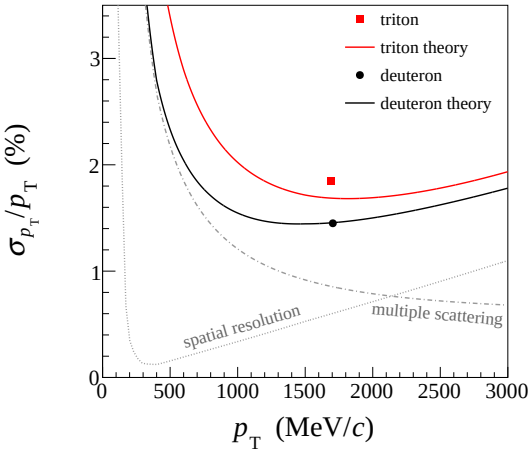

Figure 3.12 Transverse momentum resolution of deuteron and triton. The theoretical lines as a function of momentum are compared with the data. The two factors of momentum resolution (spatial resolution and multiple scattering) are indicated for the deuteron.

3.3.8 Vertex reconstruction

Determining position information for the primary vertices is essential for selecting on-target events, selecting primary tracks, and improving momentum resolution. The C++ package RAVE [70] is used for vertex reconstruction in the SπRIT-TPC. RAVE is the optimized vertex reconstruction tool for high multiplicity events developed by the CMS community. We used the Adaptive Vertex Fitter (AVF) [70] among other fitters for the reconstruction of a vertex. The AVF is an iterative weighted Kalman filter, which will assign a weight to each track, ignoring outlier tracks. The user

parameters for the implementation of RAVE are adjusted as explained in Ref. [71].

The position distribution of reconstructed vertices along the beam axis is shown in Fig. 3.13. Peaks corresponding to the position of the beam pipe window (the entrance of the TPC structure) and the target are visible, followed by active-target type events in the P10 gas. The occurrence of active-target events decreases along the beam axis as a result of the trigger condition.

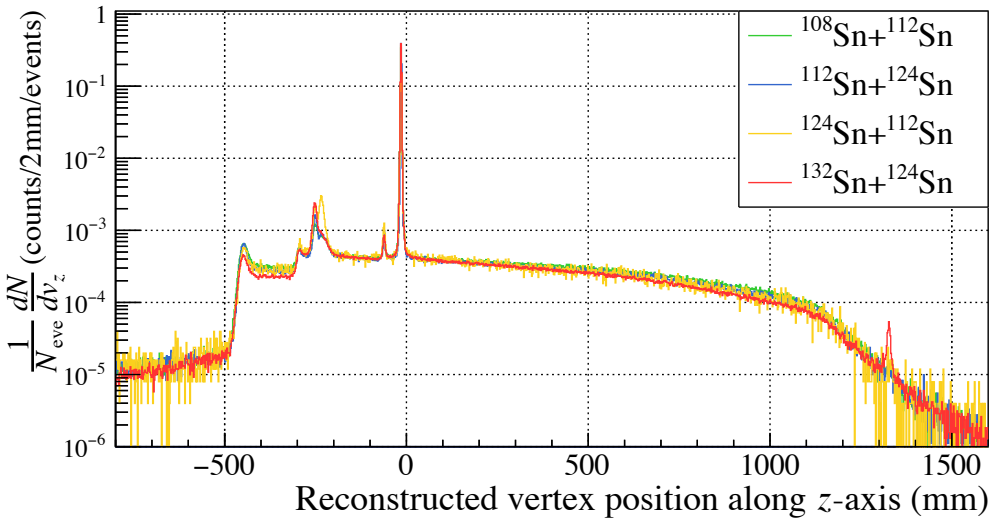

Figure 3.13 Vertex distribution along the beam axis. The beam pipe window, TPC structure, and on-target collision events are evident. The decreasing trend of P10 gas target events is due to the trigger condition provided by the Kyoto Multiplicity Array. Adopted from Ref. [12]

Chapter 4

Data Analysis

4.1 Particle Identification

The particle identification for the SπRIT-TPC experiment, the truncated mean of energy loss per unit length, $\langle dE/dx \rangle$, and the magnetic rigidity, p/Z (momentum divided by charge in laboratory frame), is used. To simplify the description, we use the following notation for the momentum per charge and p/Z and mean energy loss per unit length$\langle dE/dx \rangle$:

$$\mathcal{P} = p/Z,$$

$$\mathcal{E} = \langle dE/dx \rangle.$$

The distribution of energy loss per unit length dE/dx for charged particles in the gas can be described by the Landau function, which is also known as the straggling function [72]. The most probable value is the most reliable parameter representing the track's dE/dx distribution. However, the number of hit clusters is usually insufficient to reconstruct the complete dE/dx distribution function. Moreover, rare single-collisions (creating delta electrons, for example) sometimes leave with high energy loss, and it distorts the straggling function. Therefore, the truncated mean of dE/dx is preferred to the most-probable value in the TPC analysis.

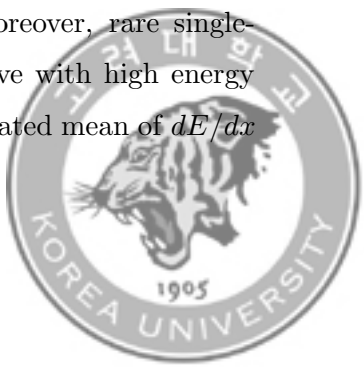

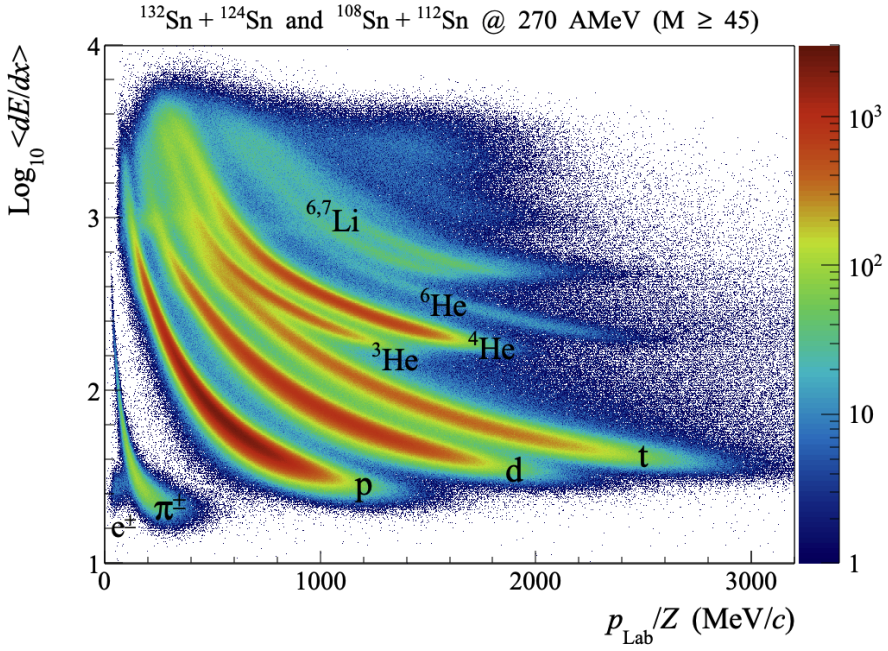

Figure 4.1 PID plot showing $\mathrm{Log}_{10}\mathcal{E}$ vs $\mathcal{P}$ ($\mathrm{Log}_{10}\langle dE/dx\rangle$ vs p/Z) of two collision systems ^{132}Sn + ^{124}Sn and ^{108}Sn + ^{112}Sn.

For SπRIT-TPC, the mean energy loss per unit length $\mathcal{E}$ is calculated by truncating the highest 30 % of the dE/dx values of hit clusters. The disadvantage of this method is that the total $\mathcal{E}$ spectrum does not follow the empirical Bethe–Bloch formula.

Fig. 4.1 show PID plot ($\mathcal{E}$ vs $\mathcal{P}$) of two collision systems ^{132}Sn + ^{124}Sn and ^{108}Sn + ^{112}Sn together from the events. The y-axis is exploded using $\mathrm{Log}_{10}\mathcal{E}$. General quality cuts are applied in the figure which are introduced in Table 4.3 with charged track multiplicity cut of 45. In the plot, we can observe e^-, π^+, p, d, t, ^{3}He, ^{4}He, ^{6}He, ^{6}Li, ^{7}Li from left bottom corner to the top right by eye. Considering that tighter cuts will be applied later, the absolute number of yield is insufficient for the relatively heavy fragments ^{6}He, ^{6,7}Li and $Z \geq 4$ even though they are visible from Fig. 4.1. Therefore, these heavy particles are not included in the analysis and we focus on identifying p, d, t, ^{3}He and ^{4}He.

Instead, we attempt to fit our data with the modified version of the Bethe-Bloch

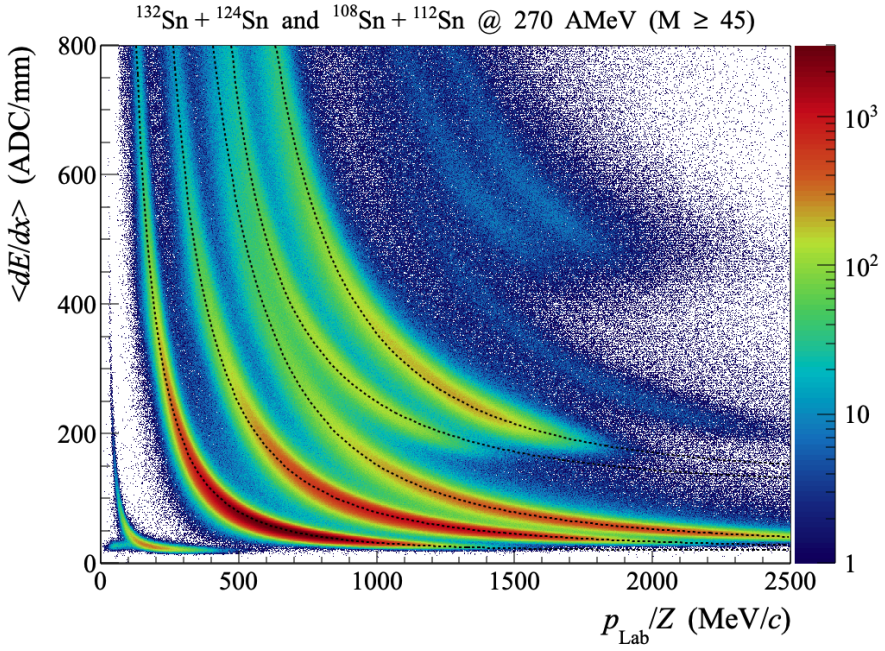

Figure 4.2 PID plot ($\mathcal{E}$ vs $\mathcal{P}$) of two collision systems ^{132}Sn+^{124}Sn and ^{108}Sn+^{112}Sn. The fitted modified Bethe-Bloch formula of Eq. (4.1) is drawn for Hydrogen and Helium isotopes.

formula with six fit parameters C_i (i = 1, 2, 3, 4, 5, 6),

$$\mathcal{E} = \frac{C_1 + C_2\beta}{\beta^2}\left[\ln\left(C_3 + \left(\frac{m_e}{\beta}\right)^{C_4}\right) - \beta^{C_5} + C_6\right], \tag{4.1}$$

where $\beta = p/\sqrt{p^2 + m}$ is the velocity and m_e is the electron mass. The result of the fit is shown in Fig. 4.2. The fitted lines are drawn with dotted black in each particle spectrum. There are small discrepancies, such as the deuteron spectrum near $\mathcal{P} \sim$ 600 MeV/c or at the high rigidity end of the ^{3}He. However, these differences do not affect the PID analysis so much as the systematic uncertainty in PID is found to be small when the PID probability cut is applied. The real issue to be discussed comes from separating the t and ^{3}He in the low rigidity region ($\mathcal{P} \leq$ 700 MeV/c). Since the spectrum of t and ^{3}He are very close to each other, the uncertainties increases

for ^{3}He. This issue will be discussed later.

The final goal of PID is to define the probability value of being particle I for each track. By multiplying the probability by the total particle yield, one can extract the yield of the selected particle and remove background particles. In our case, a track will have probability values for being one of the five particles: p, d, t, ^{3}He, and ^{4}He. To achieve this, the $\mathcal{E}$ spectrum of each particle I is fitted by Gaussian distribution through the different rigidity ranges with the center value of $\mathcal{P}$: $\mathrm{Fit}_I(\mathcal{P}|\mathcal{E})$. The mean value $\mu_I(\mathcal{P}|\mathcal{E})$ of Gaussian distribution is then given by the modified Bethe-Bloch formula. At the same time, the amplitude $A_I(\mathcal{P}|\mathcal{E})$ and standard deviation $\sigma_I(\mathcal{P}|\mathcal{E})$ are fitted simultaneously. The PID probability $\mathrm{Prob}_I(\mathcal{P}|\mathcal{E})$ of the track being particle I from given $\mathcal{P}$ and $\mathcal{E}$ can be defined as

$$\mathrm{Prob}_I(\mathcal{P}|\mathcal{E}) = \mathrm{Fit}_I(\mathcal{P}|\mathcal{E}) \Big/ \sum_{i=p,d,t,^3\mathrm{He},^4\mathrm{He}} \mathrm{Fit}_i(\mathcal{P}|\mathcal{E}) \ . \tag{4.2}$$

Fig. 4.3 shows an example of PID-Probability evaluation for $\mathcal{P} = 650$ MeV/c and $\mathcal{E}= 400$. The upper panel shows PID fits as a function of $\mathcal{E}$ for each particle in different colors where the y-axis show relative count. The sum of fits is shown as a gray band. The PID-Probability for triton (green) 32 %, at selected ($\mathcal{P}$, $\mathcal{E}$) values is calculated from the division between triton count (262) and total count (809). The same is done for ^{3}He (blue) from the division between ^{3}He count (262) and total count (809) to get 67 %.

The lower panel shows the PID-Probabilities as a function of $\mathcal{E}$ for each particle. The shaded area shows the selected $\mathcal{E}$ range when analysis cuts (Sigma distance |SD| cut and PID-Probability cut) are applied, which will be discussed in Section 4.4. Note that the sigma distance (distance from the fitted mean in σ unit) cut and PID-Probability cuts complement each other. For example, proton PID-Probability is almost 100 % for $\mathcal{E}$ = 20 - 40, but the tracks (if they exist) in this region are likely to be low-quality tracks or light particles such as pions and electrons. The same logic can be applied to ^{4}He in high $\mathcal{E}$. These tracks can be removed from the sigma

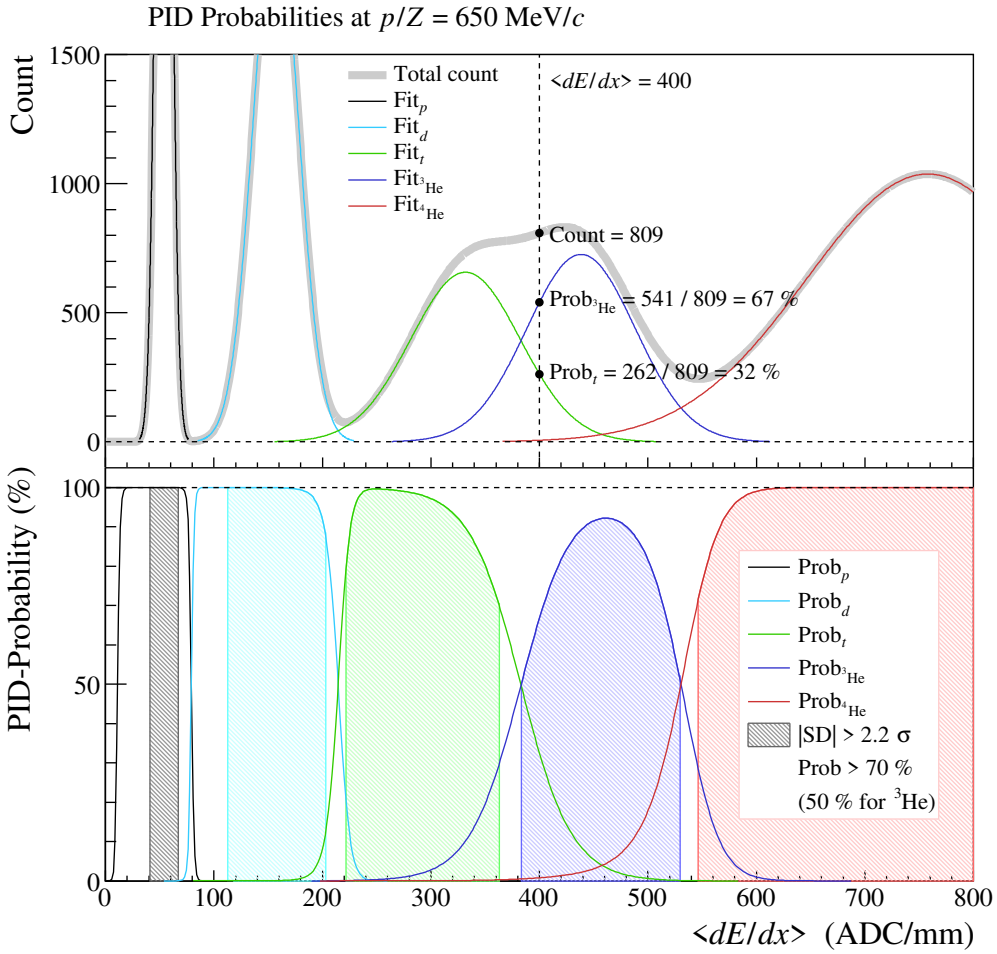

Figure 4.3 Upper panel: The PID fits as a function of $\langle dE/dx \rangle$ in p/Z around 650 MeV/c. The total count is shown as a gray band, and each PID fit is shown with different colors. The evaluation of PID-Probabilities for t and ^{3}He are shown at p/Z= 650 MeV/c and $\langle dE/dx \rangle$ = 400. Lower panel: Evaluated PID-Probability is shown for each particle. The shaded area shows the chosen range when the analysis cuts (Sigma distance |SD| cut and PID-Probability cut) are applied.

	^{132}Sn + ^{124}Sn	^{108}Sn + ^{112}Sn
p	0.85	0.85
d	0.86	0.86
t	0.87	0.87
^{3}He	0.88	0.88
^{4}He	0.89	0.89

Table 4.1 The average efficiencies in $0 < y_0 < 0.4$ and $0 < p_T/A < 600$ MeV/c.

distance cut. Moreover, the value of PID-Probability cut with > 50 % is used to prevent double counting tracks, which cannot be done with a sigma distance cut.

4.2 Monte Carlo Embedding and Efficiency

The TPC efficiencies arising from the detector performance are determined by the track embedding method [12, 73] using events generated from Monte Carlo (MC) simulations and GEANT-4. The embedding technique simulates a single track inside the simulation flow and then embeds it into the actual data taken from the experiment. This way, we can account for the real detector effects that are not considered in the simulation.

About 10^6 tracks for each p, d, t, ^{3}He and ^{4}He are simulated through the MC, which were distributed uniformly in the range of transverse momentum p_T from 0 to 1200, 1400, 1600, 2500 and 2500 MeV/c for p, d, t, ^{3}He and ^{4}He respectively, and rapidity $-1 \leq y_0 < 2$. Here, rapidity is defined by $y_0 = y/y_{NN}^{c.m.} - 1$ where y is the rapidity of the particle and $y_{NN}^{c.m.}$ is center-of-mass rapidity of the nucleon-nucleon system.

The embedded tracks were identified with the cut $n_{\mathrm{EmbeddedCluster}}/n_{\mathrm{Cluster}} > 0.5$, where $n_{\mathrm{EmbeddedCluster}}$ is the number of clusters that are created from the embedded track and n_{Cluster} is the total number of clusters. This cut prevents 1) counting more than one embedded track that accidentally breaks into two (or more) and 2)

tracks from the actual event that collected the embedded clusters. Each (y_0, p_T) bin was weighted so that the distribution of embedded tracks in the (y_0, p_T) phase space became almost identical to the experimental distribution [12] to consider the bin smearing effect.

The efficiency Eff_I of the particle I for given (y_0, p_T) can be constructed as

$$\mathrm{Eff}_I(y_0, p_T) = \frac{n_I^{\mathrm{reco}}(y_0, p_T)}{n_I^{\mathrm{init}}(y_0, p_T)}, \tag{4.3}$$

where $n_I^{\mathrm{reco}}(y_0, p_T)$ and $n_I^{\mathrm{init}}(y_0, p_T)$ are the number of reconstructed embedded tracks and the number of initial tracks that are embedded, respectively.

Fig. 4.4 show evaluated efficiencies in the (y_0, p_T/A) phase space for p, d, t, ^{3}He and ^{4}He. The cuts applied in this figure are $-30° < \phi < 20°$, $160° < \phi < 210°$, distance-to-vertex < 20 mm and number-of-clusters ≥ 15. The references lines are shown with $\theta_{\mathrm{Lab.}}$ (dotted) at 30 and 60 degrees, and $p_{\mathrm{Lab.}}/Z$ (dashed) for 500 MeV/c interval. Because of the bin smearing effect, efficiency larger than 1 (yellow to dark red) is shown in large p_T/A. The average efficiency values in the region for analysis; $0 < y_0 < 0.4$ and $0 < p_T/A < 600$ MeV/c, are summarized in Table 4.1.

The final correction factor C_I for particle I can be obtained as

$$C_I = \frac{\mathrm{Prob}_I}{\mathrm{Eff}_I}. \tag{4.4}$$

4.3 The Impact Parameter Selection

The impact parameter b is defined by the distance between the center of the two nuclei at their impact. The impact parameters characterize the initial state of the heavy-ion collisions and give influence many physics observables. Therefore, the experiments must determine and gate on the events with chosen impact parameter. However, the impact parameter is not directly measurable in the experiments. One

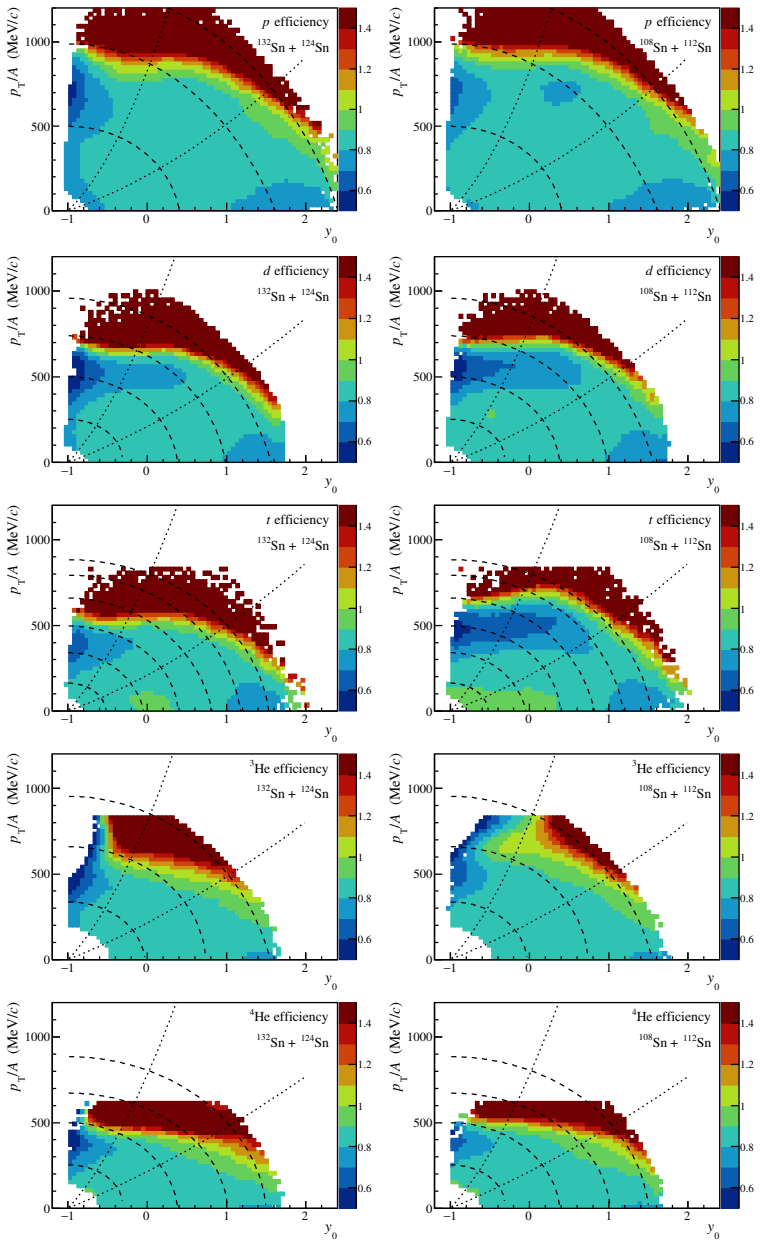

Figure 4.4 The efficiency of the hydrogen and helium isotopes for $^{132}\mathrm{Sn} + ^{124}\mathrm{Sn}$ and $^{108}\mathrm{Sn} + ^{112}\mathrm{Sn}$ systems in the phase space of y_0 and p_T/A. The reference lines of $\theta_{\mathrm{Lab.}}$ (dotted) for 30 and 60 degrees and $p_{\mathrm{Lab.}}/Z$ (dashed) in 500 MeV/c interval are shown.

observable that is strongly correlated with the impact parameter is the multiplicity of the detected charged particles [74].

The geometrical cross-section is defined as,

$$\sigma_{\mathrm{g}} = \pi b^2, \tag{4.5}$$

and the total geometrical cross-section can be written as,

$$\sigma_{\mathrm{max}} = \pi b_{\mathrm{max}}^2, \tag{4.6}$$

where b_{max} is the maximum impact parameter corresponding to the sum of the radius of the target and projectile nucleus. In the SπRIT experiment, the b_{max} from the experimental total cross section was found to be 7.52 fm for ^{132}Sn + ^{124}Sn, 7.13 fm for ^{108}Sn + ^{112}Sn, 7.33 fm for ^{112}Sn + ^{124}Sn and 7.31 fm for ^{124}Sn + ^{112}Sn reactions [50]. Generally, the mean value of the charged particle multiplicity N decreases monotonously as a function of impact parameter b. Therefore, we can write down the relation between multiplicity N, and corresponding impact parameter b as

$$\sum_{N'=N}^{\infty} \sigma(N') = \int_0^{b^2} d(b'^2) \frac{d\sigma_{\mathrm{g}}}{d(b'^2)}, \tag{4.7}$$

where $\sigma(N)$ and σ_{g} are the measured cross section for the charged particle multiplicity N and the geometrical cross-section respectively. Since $d\sigma_{\mathrm{g}}/d(b^2) = \pi$, the equation follows,

$$\pi b^2 = \sum_{N'=N}^{\infty} \sigma(N'), \tag{4.8}$$

$$\frac{b^2}{b_{\mathrm{max}}^2} = \sum_{N'=N}^{\infty} \frac{\sigma(N')}{\sigma_{\mathrm{max}}}. \tag{4.9}$$

Now we introduce the reduced impact parameter [74] $\hat{b} = b/b_{\mathrm{max}}$ ranging from

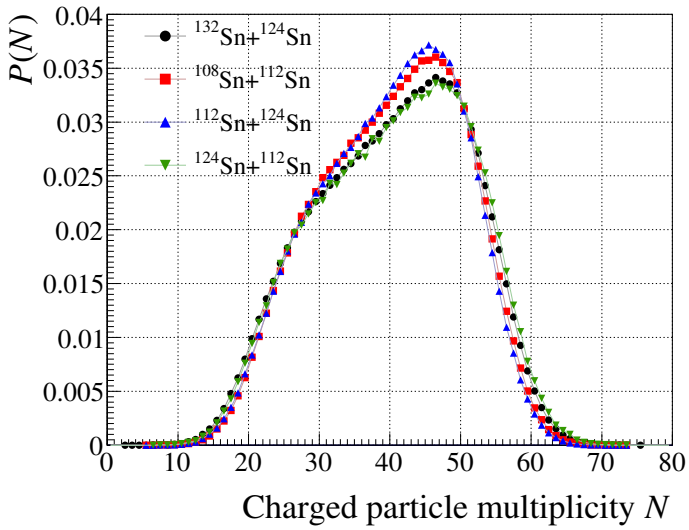

Figure 4.5 The probability distribution of charged particle multiplicity.

0 to 1, and the event probability $P_{\text{event}}(N) = \sigma(N)/\sigma_{\text{max}}$ with the charged particle multiplicity equal to N normalized by $\sum_N P_{\text{event}}(N) = 1$. The resultant relation between reduced impact parameter $\hat{b}$ and probability $P_{\text{event}}(N)$ becomes,

$$\hat{b} = \frac{b}{b_{\text{max}}} = \sqrt{\sum_{N'=N}^{\infty} P_{\text{event}}(N')} \ . \tag{4.10}$$

Therefore, one can extract the impact parameter b by summing $P_{\text{event}}(N)$ over N, which is equal to or greater than N, given that the total geometrical cross-section is known.

$$b = b_{\text{max}} \sqrt{\sum_{N'=N}^{\infty} P_{\text{event}}(N')} \ . \tag{4.11}$$

Fig. 4.5 shows the probability $P_{\text{event}}(N)$ distributions as a function of charged particle multiplicity N for the four collision systems. Since a larger number of nucleons

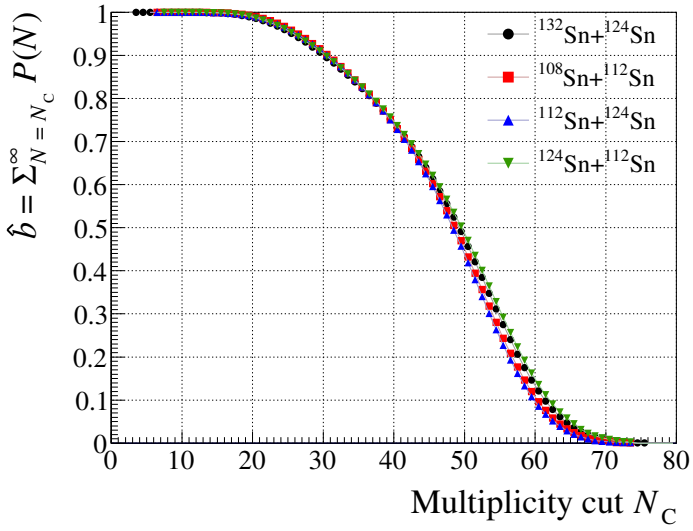

Figure 4.6 The reduced impact parameter $\hat{b}$ as a function of multiplicity cut N.

exist in the beams in the two systems ^{132}Sn + ^{124}Sn and ^{112}Sn + ^{124}Sn compared to the other two systems ^{108}Sn + ^{112}Sn and ^{124}Sn + ^{112}Sn, the $P(N)$ values in the region below $N \sim 50$ is smaller for the former two systems. In contrast, the opposite trend is shown for the above region.

Fig. 4.6 and 4.7 show the distribution of reduced impact parameter $\hat{b}$ and impact parameter b respectively as a function of multiplicity cut N. The calculated values are listed in Table 4.2. Note that the selection of charge multiplicity cut for $b \lesssim$ 1.5 fm corresponds to the 57 and 56 for ^{132}Sn + ^{124}Sn and ^{108}Sn + ^{112}Snystems, respectively, which are highlighted by cyan and yellow.

4.4 Selection of the Data

The selection of the quality cuts is summarized in Table 4.3. In the PID quality cut, we consider PID probability which measures the particle signal out of total yield, and PID sigma distance which measures the distance from the center $\langle dE/dx \rangle$

	^{132}Sn + ^{124}Sn		^{108}Sn + ^{112}Sn		^{112}Sn + ^{124}Sn		^{124}Sn + ^{112}Sn	
N	b (fm)	$\hat{b}$	b (fm)	$\hat{b}$	b (fm)	$\hat{b}$	b (fm)	$\hat{b}$
45	4.61	0.614	4.29	0.602	4.36	0.595	4.55	0.622
46	4.4	0.586	4.08	0.572	4.13	0.563	4.35	0.595
47	4.18	0.556	3.85	0.539	3.88	0.53	4.14	0.566
48	3.94	0.524	3.6	0.505	3.62	0.494	3.92	0.536
49	3.69	0.491	3.35	0.47	3.35	0.457	3.69	0.504
50	3.44	0.457	3.08	0.432	3.07	0.419	3.44	0.471
51	3.17	0.421	2.81	0.395	2.78	0.38	3.19	0.436
52	2.89	0.385	2.54	0.356	2.49	0.34	2.93	0.401
53	2.62	0.348	2.27	0.318	2.21	0.301	2.67	0.365
54	2.34	0.311	2	0.28	1.93	0.263	2.4	0.329
55	2.07	0.275	1.74	0.243	1.66	0.227	2.14	0.292
56	1.8	0.24	1.49	0.209	1.41	0.193	1.88	0.257
57	1.55	0.206	1.26	0.176	1.19	0.162	1.63	0.223
58	1.32	0.175	1.04	0.146	0.977	0.133	1.4	0.192
59	1.1	0.147	0.851	0.119	0.793	0.108	1.19	0.162
60	0.909	0.121	0.685	0.0961	0.63	0.086	0.996	0.136
61	0.735	0.0978	0.542	0.0761	0.491	0.067	0.821	0.112
62	0.586	0.078	0.417	0.0585	0.377	0.0515	0.664	0.0909
63	0.46	0.0611	0.316	0.0444	0.285	0.0389	0.528	0.0722
64	0.354	0.0471	0.234	0.0329	0.209	0.0286	0.423	0.0579
65	0.27	0.0359	0.172	0.0242	0.15	0.0204	0.328	0.0448

Table 4.2 List of expected impact parameter b and reduced impact parameter $\hat{b}$ when multiplicity cut N is chosen. The highlighted rows in cyan and yellow are the selection of the multiplicity cuts in the data analysis for reactions ^{132}Sn + ^{124}Sn and ^{108}Sn + ^{112}Sn respectively, which correspond to $b \lesssim 1.5$ fm.

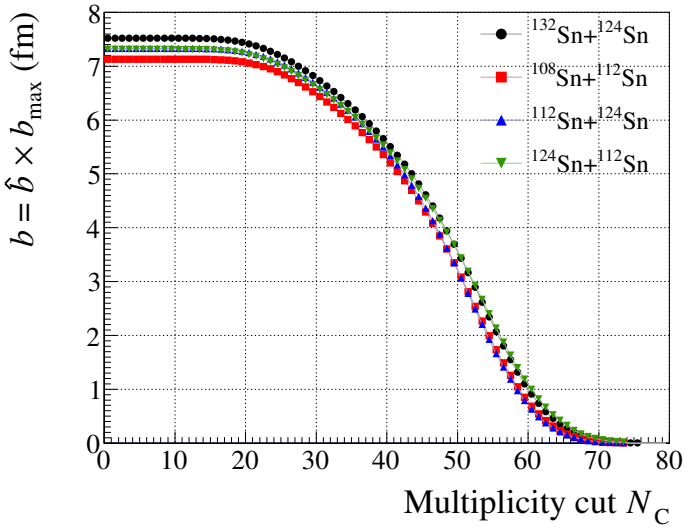

Figure 4.7 The impact parameter b as a function of multiplicity cut N.

of the PID line to the $\langle dE/dx \rangle$ of the track in σ_{PID} unit. Other than quality cuts, azimuthal angle cut $\theta < 80°$ and ϕ angle cut of beam-left ($160 < \phi < 210$) and beam-right ($-20 < \phi < 30$) is chosen.

Most of the particles are hardly affected by the PID quality cuts. However, triton and ^{3}He spectrum in PID plot is found to overlap by a considerable amount below $p_Z/A \sim 700$ MeV/c as it can be found from the Bethe-Bloch lines of Fig. 4.2. It should be noted that the contamination of tritons in the ^{3}He spectrum with ^{3}He probability larger than 50 % is found to be $\sim$ 40 % at $p/Z = 700$ MeV/c and constantly decreases down to 10 % at $p/Z = 1000$ MeV/c. The range of interest in this work is the mid-rapidity region, where the participating nucleons are most involved in the dynamic process. The PID plot in different rapidity regions is shown in Fig. 4.8 where the cuts in Table 4.3 are applied. Here the rapidity y_0 is defined by the $y_0 = y/y_{NN}^{c.m.} - 1$ where y and $y_{NN}^{c.m.}$ is rapidity of the particle and center-of-mass rapidity of the nucleon-nucleon system.

In all four different rapidity ranges y_0, the proton, deuteron, and ^{4}He are well

Quality cut	Default value	Variation
PID probability (Prob)	Prob > 70 % (50 % for ^{3}He)	± 10 %
PID sigma distance (|SD|)	|SD| < 2.2 σ_{PID}	± 0.2 σ_{PID}
Number of clusters (NCl)	NCl > 20	± 2
Distance to vertex (DistV)	DistV < 15 mm	± 4 mm
Charged particle multiplicity (Mult)	Mult ≥ 57 (56)	± 1

Table 4.3 List of quality cuts and default values applied to the analysis.

separated. In the mid-rapidity range $y_0 = -0.4$ - 0, the triton spectrum is shown in the rigidity above $p/Z = 700$ MeV/c while ^{3}He spectrum is placed below $p/Z = 1000$ MeV/c. In addition, the efficiency of the track in this region making challenging to analyze the data with accuracy. The same mid-rapidity range in the positive region $y_0 = 0$ - 0.4 show that triton entirely runs away from the overlapping region while ^{3}He spectrum stays in the rigidity region $p/Z = 600$ - 1000 MeV/c where triton contamination is around 30 %. For this region, the significant number of ^{3}He is lost with a PID probability of 70 %. Therefore, we choose a PID probability cut of 50 % for ^{3}He while 70 % is used for other particles.

For The track quality cut, the number of clusters in the track (NCl) and the distance to the primary vertex (DistV) in mm are considered. For the event quality cut, the charged particle multiplicity (Mult) is used, which is related to the impact parameter of the collision. The chosen impact parameter in this work is b < 1.5 fm, and the corresponding multiplicity is found in Table 4.2. The closest value which satisfies the condition b < 1.5 fm is 57, as highlighted in cyan for the ^{132}Sn + ^{124}Sn system, and 56 as highlighted in yellow for the ^{108}Sn + ^{112}Sn.

4.5 Summary of Systematic Uncertainties

The systematic uncertainties are studied as a function of p_T/A by varying the different quality cuts. The default and variation of cuts for the analysis are listed in Table 4.3. The summarized result is listed in Table 4.4 showing the total systematic

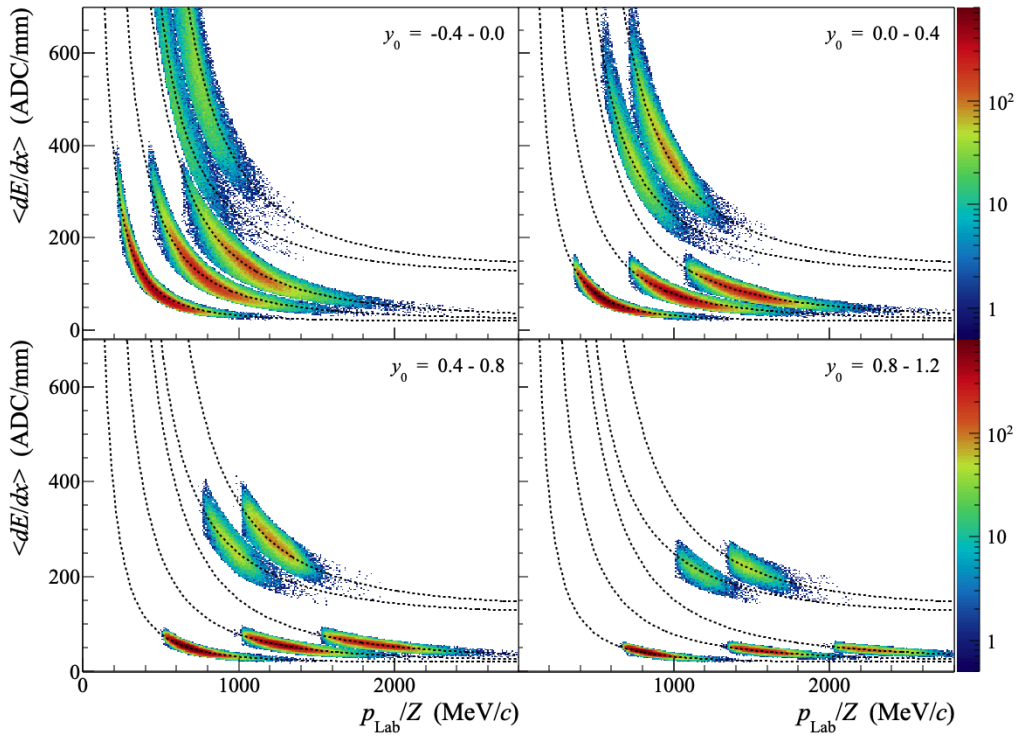

Figure 4.8 PID plots shown for different rapidity ranges. The top right figure show the rapidity range used in this analysis.

	^{132}Sn + ^{124}Sn	^{108}Sn + ^{112}Sn	Yield ratio R_{21}
p	3.8	3.7	1.0
d	3.6	3.5	1.4
t	3.3	3.7	2.0
^{3}He	5.4	4.8	2.1
^{4}He	4.0	3.4	2.3

Table 4.4 The systematic errors (%) in the range y_0 = 0 - 0.4 and p_T/A = 0 - 400 MeV/c.

error analyzed in p_T/A = 0 - 400 MeV/c for the ^{132}Sn + ^{124}Sn system (Y_2), ^{108}Sn + ^{112}Sn system (Y_1) and the ratio between two ($R_{21} = Y_2/Y_1$). Also, p_T/A and y_0 dependent error distribution can be found in the Figures 4.9, 4.10, and 4.11. See Appendix A for detail.

The systematic error of particle yield in $p_T/A < 400$ MeV/c is 5 % for ^{3}He and 4 % for other particles (Fig. 4.9). The large error of ^{3}He is because the triton spectrum largely overlaps the spectrum of ^{3}He in PID analysis. This effect can be observed in Fig. A.4 where the change in PID probability cut from 50 % to 70 % makes a large difference in the yield. The error is larger for the negative rapidity region, as shown in Fig. 4.10. However, this discrepancy partly recover in the ratio for $p_T/A < 400$ MeV/c, where most particles have systematic error around 2 % (Fig. 4.11). In the higher p_T/A region of 400 - 600 MeV/c, the systematic errors for p and d hardly change in particle yield and yield ratio. While the systematic error of t and ^{3}He increases up to 15 % and a systematic error of ^{4}He increase over 20 %.

The systematic error as a function of rapidity (Fig. 4.10) shows that all particles except ^{3}He below $y_0 \lesssim 1$ has error around 3 - 5 % while ^{3}He has a larger error (15 - 17 %) for negative rapidity and linearly decrease down to 5 - 6 % from y_0= -0.2 to y_0= 0.2. The error increases exponentially in the high rapidity region at y_0= 0.8 for Helium and y_0= 1.2 for d and t.

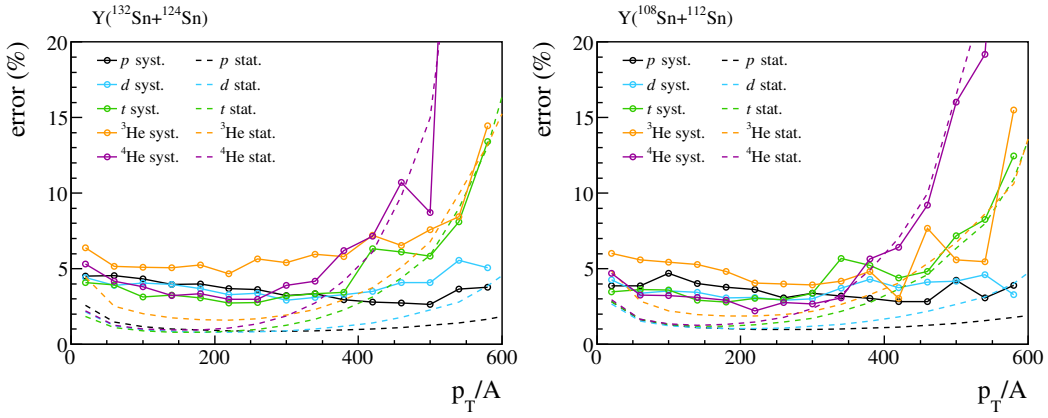

Figure 4.9 Summary of p_T/A distribution error.

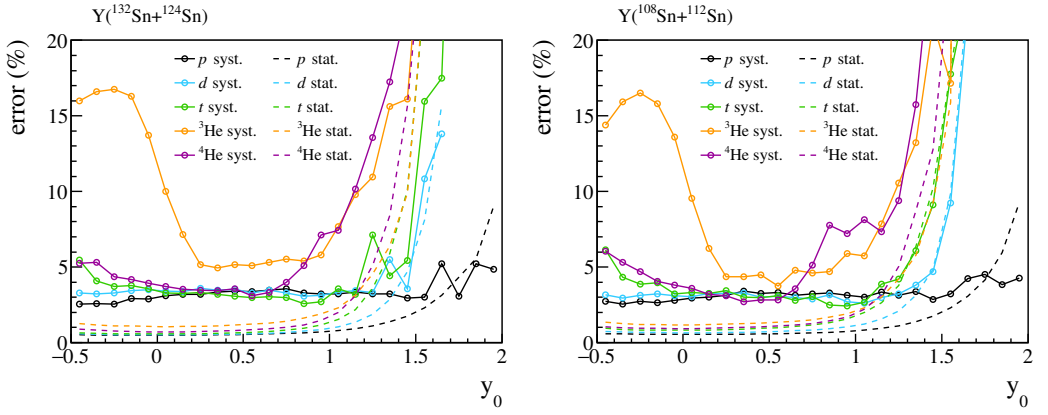

Figure 4.10 Summary of y_0 distribution error.

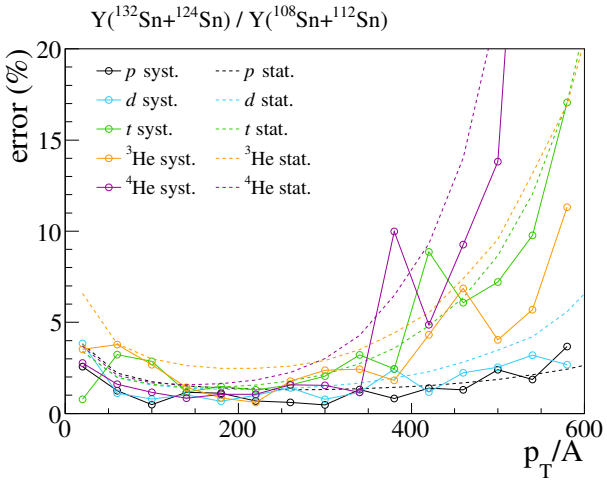

Figure 4.11 Summary of p_T/A yield ratio error.

Chapter 5

Result

In this chapter, we analyze isoscaling properties measured from the neutron-rich system ^{132}Sn + ^{124}Sn and nearly symmetric system ^{108}Sn + ^{112}Sn using Hydrogen isotopes and Helium isotopes. The result is compared to the Statistical Multifragmentation Model (SMM) and Asymmetrized Molecular Dynamic Model (AMD) model calculations. The parameter sets used in AMD are chosen in Ref. [13]. This chapter will focus mainly on the transverse distribution of Hydrogen and Helium isotopes. It is an extended work of Ref. [13], which discussed the rapidity distribution of Hydrogen isotopes from the SπRIT experiment. This analysis was also published as Ref. [75].

5.1 Particle Yield

The left panels of Fig. 5.1 show experimental rapidity distribution of p, d, t, ^{3}He, ^{4}He from top to bottom for ^{132}Sn+^{124}Sn (black circle) and ^{108}Sn+^{112}Sn (red square). The particle yields of the different systems are shown together in each panel. The neutron-rich system ^{132}Sn + ^{124}Sn is shown to produce more d, t, and ^{4}He compared to the nearly symmetric system ^{108}Sn + ^{112}Sn while proton and ^{3}He are produced more from the ^{108}Sn + ^{112}Sn. Since the efficiencies are very low from the rapidity

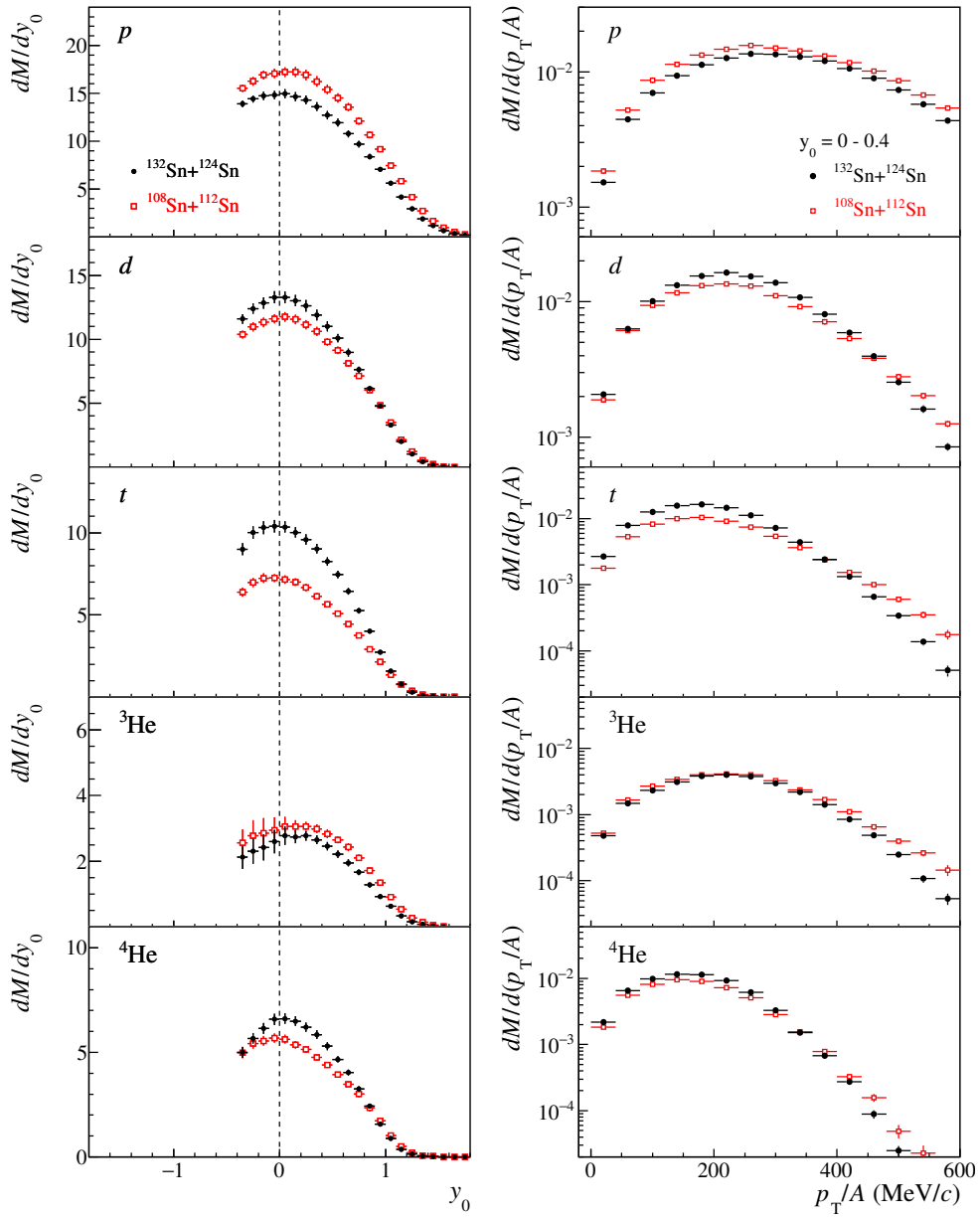

Figure 5.1 Particle yields from ^{132}Sn+^{124}Sn (black circle) ^{108}Sn+^{112}Sn (red square) systems at 270 MeV/u. Left: Rapidity distribution. Right: p_T/A distribution with mid-rapidity gate y_0 = 0 - 0.4. The exact point values are listed in Tables C.2, C.3, C.4, C.5, C.6.

below zero, only the $y_0 > -0.4$ regions are shown. The difficulty in identifying ^{3}He from the PID analysis results in the distorted shape of ^{3}He as discussed previously in Section 4.1. We chose the PID-probability cut to be 70 % for all particles but ^{3}He (50 %). The peak positions of Helium isotopes are off from the center because of the PID ambiguity and low efficiencies due to the geometric limits in SπRIT-TPC.

The right panels of Fig. 5.1 show experimental p_T/A distribution of p, d, t, ^{3}He, ^{4}He in each panel for ^{132}Sn+^{124}Sn (black circle) and ^{108}Sn+^{112}Sn (red square). Here the mid-rapidity for y_0 = 0 - 0.4 is selected. First, we focus on the low transverse momentum region. A similar trend of rapidity distribution (left panels of Fig. **??**) can be seen. The three $(N-Z)$ groups can be observed. For the proton and ^{3}He with $N-Z=-1$, large yields are obtained in the ^{108}Sn + ^{112}Sn system. For the deuteron and ^{4}He with $N-Z=0$, larger yields are obtained in the ^{132}Sn + ^{124}Sn system. In the case of the tritons, the yields are larger in the ^{132}Sn + ^{124}Sn system, and the difference is the largest compared to the other particle species. This grouping will manifest more when the yield ratio R_{21} between the two systems is presented.

Now we look at the d, t, and ^{4}He at the high transverse-momentum region. These particles were produced more for ^{132}Sn + ^{124}Sn system over ^{108}Sn + ^{112}Sn system. This is expected because these particles are composed of the same or more neutrons compared to protons. However, in the high transverse momentum region just below p_T/A = 400 MeV/c, for example, for tritons, the spectra are crossing over between ^{132}Sn + ^{124}Sn and ^{108}Sn + ^{112}Sn systems. This indicates that the yield ratios between systems change as a function of p_T/A, which implies a change in the trend of the isoscaling effect. No clear explanation exists yet for the cross-over phenomenon between the two collision systems.

Fig. 5.2 show experimental rapidity (left panels) and p_T/A (right panels) distribution of p, d, t, ^{3}He, ^{4}He from top to bottom for ^{112}Sn + ^{124}Sn (black circle) and ^{124}Sn + ^{112}Sn (red square). The ^{132}Sn + ^{124}Sn system (gray box) is drawn for the comparison. These two systems are not included in the isoscaling analysis, yet, the yield distributions are shown as a reference. These two systems are mirror systems

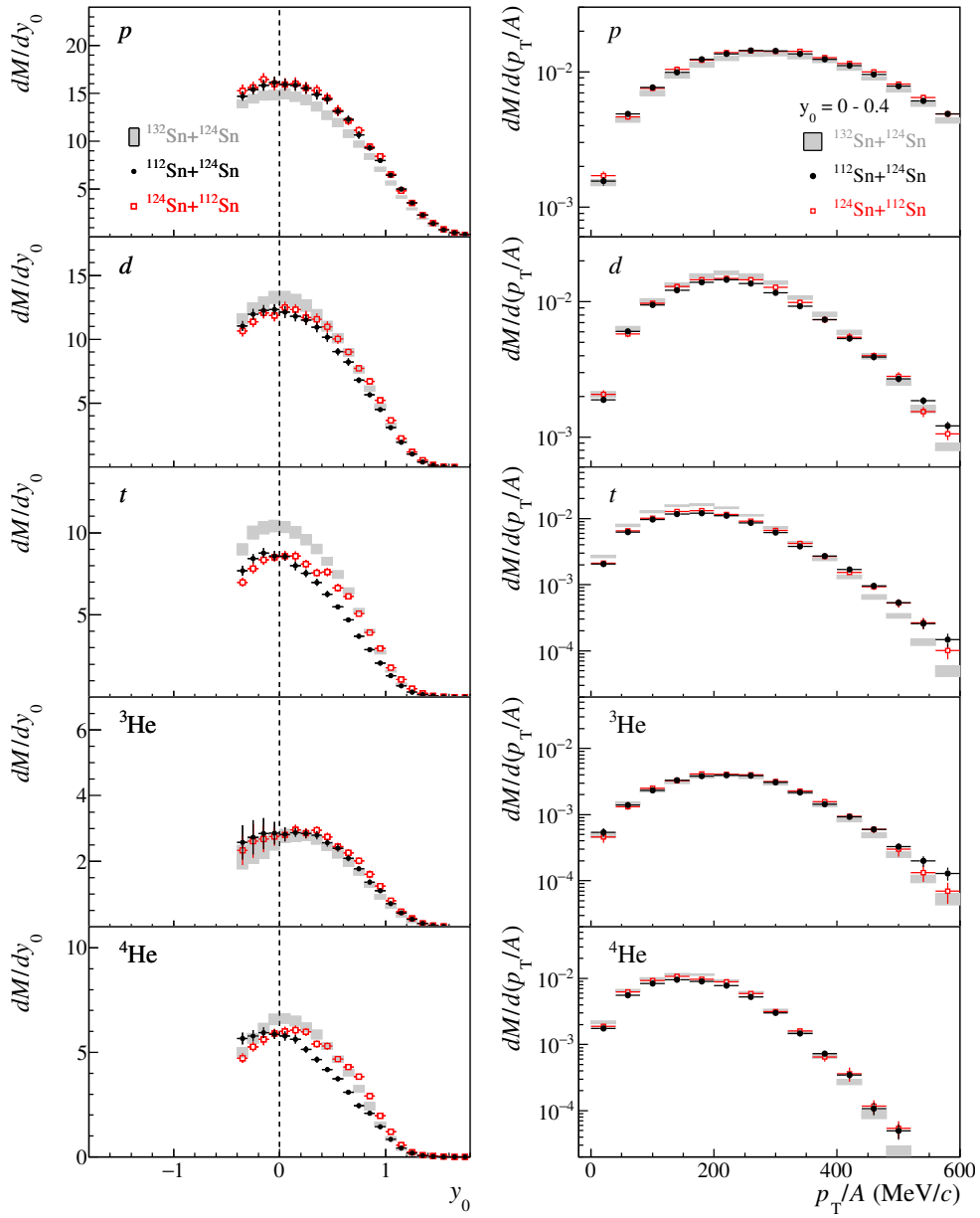

Figure 5.2 Particle yields from ^{112}Sn+^{124}Sn (black circle) ^{124}Sn+^{112}Sn (red square) systems at 270 MeV/u. The distribution from ^{132}Sn + ^{124}Sn (gray box) is drawn as a reference. Left: Rapidity distribution. Right: p_T/A distribution with mid-rapidity gate y_0 = 0 - 0.4.

where the projectile and the targets are replaced with each other. Ideally, the yield of any particles for two systems should be the same at $y_0 = 0$, which is displayed in the left panels of Fig. 5.1. The difference between the two systems is the number of neutrons. This difference is shown in the yield at the high rapidity region from the particles other than the proton. The difference is enlarged with the one neutron (triton and ^{4}He) compared to the particles with the two neutrons (triton and ^{3}He). On the right panels of Fig. 5.2, two systems (^{112}Sn + ^{124}Sn and ^{124}Sn + ^{112}Sn) show similar p_T/A distributions (right panels) as the mid rapidity gate y_0 = 0 - 0.4 is chosen.

5.2 Comparison to the previous work

The data selection and centrality is slightly different from the previous work Ref. [13]. In Ref. [13], only the beam-right ($-20 < \phi < 30$) is selected while both beam-left ($160 < \phi < 210$) and beam-right ($-20 < \phi < 30$) are used in this work. This is because larger statistics are needed to analyze the Helium isotopes. The method of centrality selection is also different due to the choice of different maximum impact parameter $b_{\rm max}$. In the former work, $b_{\rm max}$ = 10 fm was defined by the sum of the radii for the projectile and target. In this work, $b_{\rm max}$ is defined to be the experimental $b_{\rm max}$ of 7.52 fm in ^{132}Sn + ^{124}Sn and 7.13 fm in ^{108}Sn + ^{112}Sn. However, t and the results are consistent with each other. However, the selection of impact parameter cut $b < 1.5$ fm is the same in both works, and slight differences in the multiplicity gates do not affect the results of both works.

Fig. 5.3 shows the yield difference (%) of rapidity distribution between this work and Ref. [13] for the Hydrogen isotopes. The difference in the focused rapidity range y_0 = 0 - 0.4 is less than 3 % for the two systems.

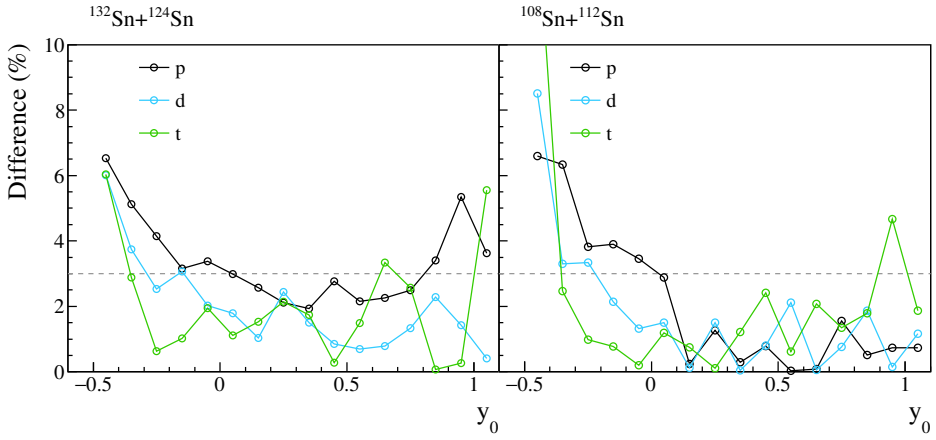

Figure 5.3 The yield Difference between this work and Ref. [13] as a function of rapidity.

5.3 Yield Ratio and Temperature

It has been shown that the isoscaling effect may occur only when the two systems have nearly the same temperature [6]. The upper panel of Fig. 5.4 displays the H-He temperature evaluated from the equation introduced in Section 1.4:

$$T_{\text{He-H}} = 14.3 \cdot \ln^{-1}\left[1.6 \cdot \frac{Y(^2\text{H}) \cdot Y(^4\text{He})}{Y(^3\text{H}) \cdot Y(^3\text{He})}\right]. \tag{5.1}$$

The upper panel of Fig. 5.5 compares only the ^{132}Sn + ^{124}Sn and ^{108}Sn + ^{112}Sn systems. The $T_{\text{H-He}}$ for both neutron-rich (solid circles) and the nearly-symmetric (open squares) systems are almost identical at the low transverse-momentum region. The temperatures increase slowly from around 8 MeV to 11 MeV with increasing the p_T/A value. Above 280 MeV/c, the temperatures start to increase dramatically. Furthermore, the temperatures of the two systems begin to diverge. Above 400 MeV/c, the temperature of the near-symmetric system is higher than that of the neutron-rich system, although the large error bars present any definite conclusions yet. The increasing temperature differences with p_T/A indicate that the Sn+Sn at

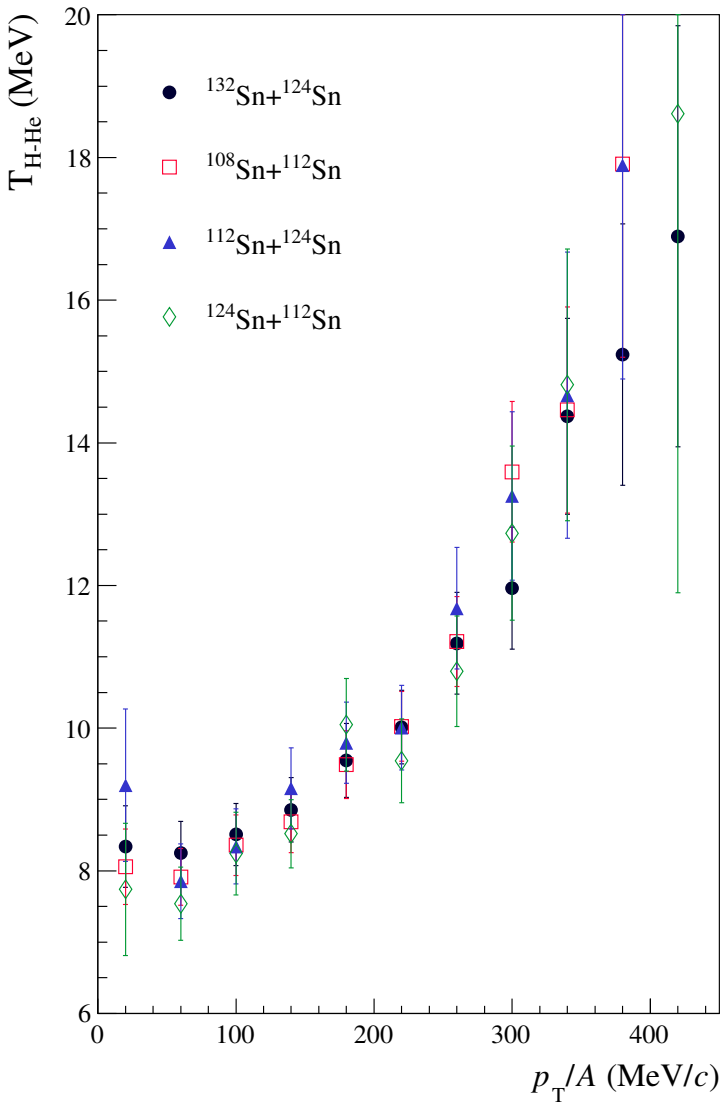

Figure 5.4 The H-He temperature evaluated using the isotope ratios. The exact point values are listed in Table C.7.

270 MeV/u studied here do not form a fully equilibrated system. Such behavior was not observed in the previous works [45, 76] at lower beam energy.

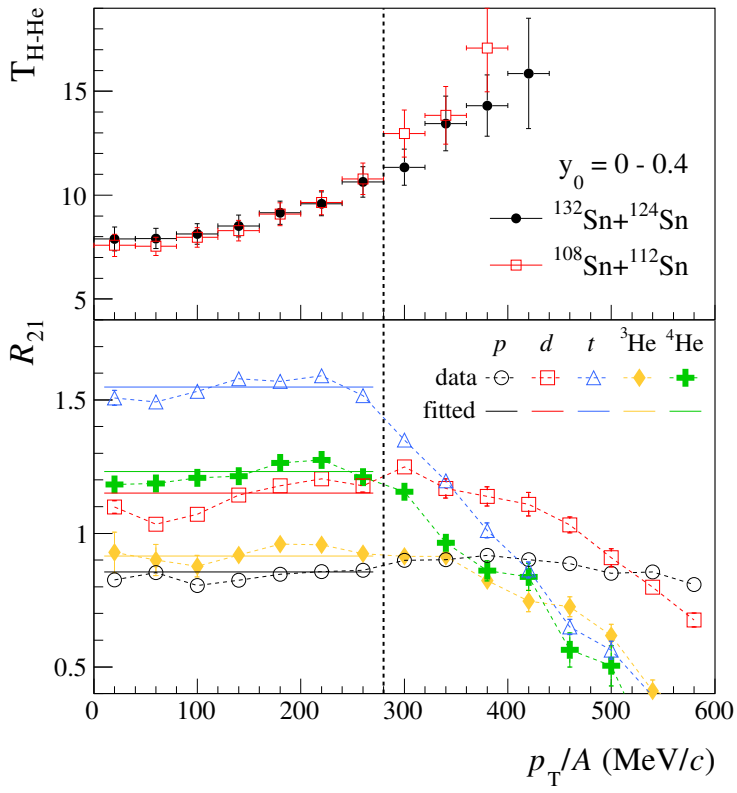

Figure 5.5 Upper panel: the H-He temperature evaluated using the isotope ratios for $^{132}\mathrm{Sn}+^{124}\mathrm{Sn}$ and $^{108}\mathrm{Sn}+^{112}\mathrm{Sn}$ systems. Lower panel: the isotope yield ratio R_{21} as a function of transverse momentum per nucleon for different particle species. The average fitted values of R_{21} are shown as the solid horizontal lines for $p_T/A < 280$ MeV/c.

Reminding of the isoscaling effect from Section 1.3, the scaling phenomenon can be observed from the yield ratio of systems 2 and 1. When systems 2 and 1 have similar temperatures and size, the isotope yield between two systems $R_{21} = Y_2/Y_1$, can be simplified as

$$R_{21}(N, Z) = C \exp(\alpha N + \beta Z). \tag{5.2}$$

where α, β and C are the fit parameters. Empirically, the fit parameters α and β have a similar value with opposite signs. Assuming of $\beta \approx -\alpha$, Eq. 5.2 becomes,

$$R_{21}(N,Z) = C \exp\left(\alpha(N-Z)\right). \tag{5.3}$$

The isoscaling is already noticeable from the R_{21} distribution by groups of the particles with the same $(N-Z)$.

Therefore, we now focus on the spectral ratios of the isotope yields $R_{21}(N,Z)$ of the Z=1 and 2 particles, observed in the ^{132}Sn + ^{124}Sn and ^{108}Sn + ^{112}Sn. The results are shown in the lower panel of Fig. 5.5 as a function of p_T/A. The dotted lines connect the data points to guide the eyes. The vertical dotted line at p_T/A = 280 MeV/c marks the approximate region when the temperatures of the two systems start to diverge.

The lower energy isotope ratios plotted to the left of the line show clear isoscaling characteristics. In each ($N-Z=-1$, 0 and 1) group, $R_{21}(N,Z)$ values are nearly constant as a function of p_T/A. Moreover, ^{3}He behaves like a proton ($N-Z=-1$) with a ratio value smaller than 1, and ^{4}He behaves similarly to a deuteron ($N-Z=0$) with a higher ratio value compared to a proton. The triton ($N-Z=1$) has the highest ratio values, about twice the difference for protons and ^{3}He particles.

The R_{21} for the five particles are plotted as functions of N and Z in the left panels of Fig 5.6 for $p_T/A < 280$ MeV/c. The three parameters α, β, and C are determined simultaneously by fitting with Eq. (5.2). The result of the fit with given N and Z numbers are shown by lines in the left panels of Fig. 5.6. On the top left panel, the fit lines of the data for isotopes with Z = 1(solid) and 2(dotted) are shown separately. The slopes represent the fit parameter α = 0.29. On the bottom left panel, the three fit lines of isotones with N = 0(solid), 1(dotted), and 2(dashed) are shown. The slopes represent the fit parameter β = -0.23. In the absence of Coulomb, protons and neutrons should behave similarly, and one would expect the two parameters to have similar values but opposite signs. This has been observed in most of the previous

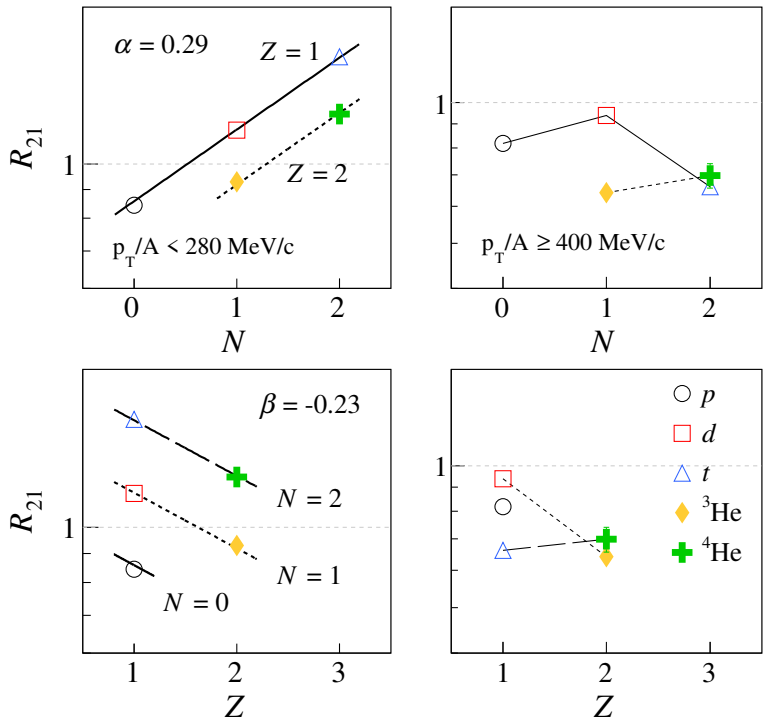

Figure 5.6 The R_{21} values of Z=1 and 2 particles are plotted as a function of N and Z at the top and bottom, respectively. In left panels, fit with Eq. (5.2) is performed for the isoscaling for $p_T/A < 280$ MeV/c. The Eq. (5.2) fit points and draw lines corresponding to the same Z (top panel) and N (bottom panel) number. The slope of the fitted lines represents the fit parameters α and β, and the values are written on the top corners. The data do not follow Eq. (5.2) in the right panels. The lines joining the data points are mainly used to guide the eyes.

studies of isoscaling. In this case, the magnitude of the α value is larger than the β value. The isoscaling ratios obtained from these fits are plotted as solid lines in the lower panel of Fig. 5.5 to the left of the vertical dashed line. The isoscaling fit of experimental data for each p_T/A range with an interval of 40 MeV/c can be found in Section B.

In contrast, except for protons, $R_{21}(N,Z)$ for high energy isotopes shown on the right side of the vertical dashed line decreases with p_T/A. Furthermore, the lines from different isotopes cross over each other. In the case of $N = 2$ particles (triton and ^{4}He), R_{21} falls off suddenly above $p_T/A = 280$ MeV/c with the most significant drop exhibited by tritons. This reflects the sharper drop in the t and ^{4}He particle spectra at the high energy. The right panels of Fig. 5.6 show the ratios R_{21} plotted as a function of N and Z for $p_T/A \geq 400$ MeV/c. The R_{21} values for t, ^{3}He and ^{4}He have nearly the same values leading to the breakdown of isoscaling. The lines connecting the data points serve only to guide the eye and provide a contrast of the trends of the R_{21} values between the low and high energy fragments.

It is also interesting to note that R_{21} is less than 1 for all high-energy isotopes. For isotopes with $p_T/A \approx 500$ MeV/c, $R_{21} \approx 0.5$ for t, ^{3}He and ^{4}He, *i.e.* 50% less tritons are produced by the neutron-rich system of ^{132}Sn + ^{124}Sn than that from the ^{108}Sn + ^{112}Sn system. So far, there is no explanation for the surprising result.

5.4 Model Comparisons

The isoscaling ratios $R_{21}(N,Z)$ of the hydrogen and helium isotopes, obtained from the experimental yields measured in the ^{132}Sn+^{124}Sn and ^{108}Sn+^{112}Sn systems, are shown in Fig. 5.7. In each panel, data are compared to the models; SMM (straight lines in the top panel), AMD$^{(S)}$, and AMD$^{(F)}$ (hatched areas in the middle and bottom panels, respectively).

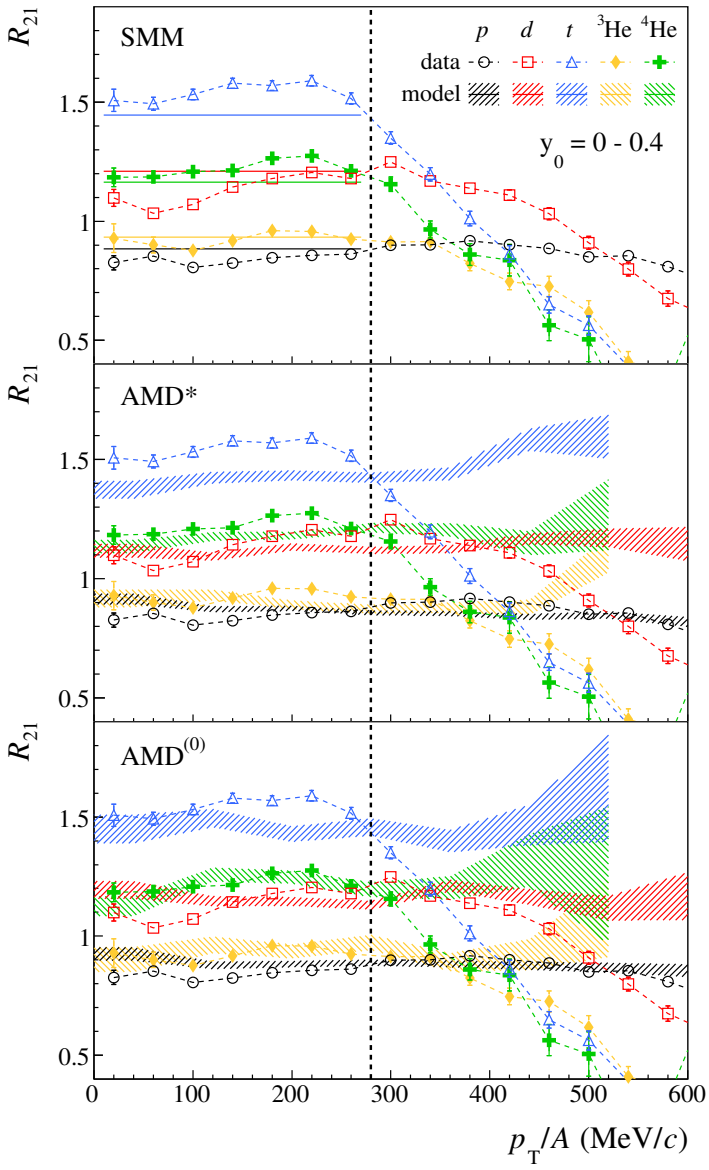

Figure 5.7 Isotope yield ratios compared with the models: SMM (top), AMD$^{(S)}$ (middle), and AMD$^{(F)}$ (bottom). The different trend of isoscaling is shown on the left and right side of the break line at $p_T/A = 280$ MeV/c.

5.4.1 Statistical Multi-fragmentation Model

Isoscaling properties observed experimentally may be understood from an equilibrated thermal source scenario. In order to check this, we employ the canonical version of the SMM model described in Refs. [40, 77]. The model assumes a breakup volume three times larger than the source at normal density and breakup temperature $T = 8$ MeV. The mass and atomic numbers of the decaying source associated with the $^{132}\mathrm{Sn} + ^{124}\mathrm{Sn}$ system are $N_2 = 93$ and $Z_2 = 79$. At the same time, $N_1 = 71$ and $Z_2 = 71$ are used in the case of the $^{108}\mathrm{Sn} + ^{112}\mathrm{Sn}$ system. These values have been selected to agree well with the measured R_{21} ratios. Different source compositions lead to slightly different R_{21} values; therefore, those adopted in this work should be seen as average values.

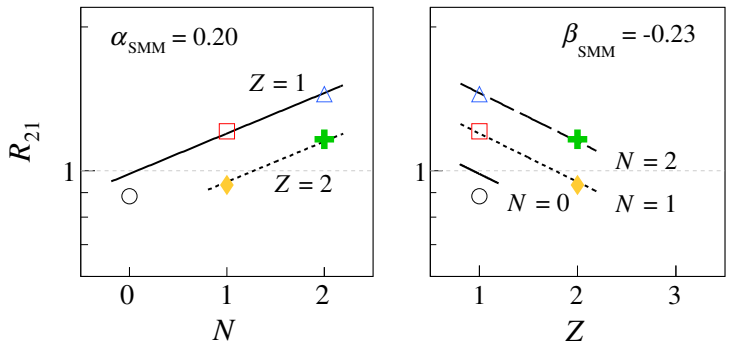

Figure 5.8 Isoscaling fit of SMM.

The predicted isotope ratios R_{21} are shown in the top panel of Fig. 5.7. The yield ratio of SMM explains experimental data roughly, but details are missing. The SMM result underestimates the triton yield ratio, and the deuteron yield ratio is larger than ^{4}He yield ratio. This is the opposite of what is found in the experimental data. The isoscaling fit of SMM is shown in Fig. 5.8 with fitted parameters $(\alpha, \beta)_{\mathrm{SMM}} = (0.20, -0.23)$. It can be predicted that SMM will not explain experimental data qualitatively as the temperature of experimental data increases from 8 MeV to 11 MeV. This suggests that Sn+Sn collision at the energy of 270 MeV/u is not a fully

thermalized system.

5.4.2 Asymmetrized Molecular Dynamic Model

In Ref. [13], the AMD model [5, 78] has been employed to describe the rapidity distributions of $Z = 1$ particles (top six panels in Fig. 5.9). The time evolution of the system is calculated by AMD until $t = 300$ fm/c. Light-charged particles' production and properties are almost determined at this primary stage. A set of parameters was chosen in Ref. [79] for a reasonable reproduction of the FOPI data of central Xe + CsI collisions at 250 MeV/u [4], paying attention to the yields of light charged particles and heavier fragments, and a kind of stopping observable of various particle species, which can be approximately expressed as $\frac{1}{2}\langle p_T^2\rangle/\langle p_z^2\rangle$ with transverse and longitudinal momentum components, p_T and p_z, in the center-of-mass frame. This parametrization of Ref. [79] with the Skyrme SLy4 effective interaction, which corresponds to soft symmetry energy with the slope parameter $L = 46$ MeV is called AMD$^{(\mathrm{F})}$ here.

For the present systems of Sn + Sn collisions, the rapidity distributions predicted by AMD$^{(\mathrm{F})}$ are shown in the right panels of Fig. 5.9. The calculated distribution looks more transparent than the data and underestimates the yields of deuterons, especially that of tritons in the mid-rapidity region. To reduce this discrepancy in the rapidity distributions, we attempted in Ref. [13] another parametrization by choosing large in-medium NN cross sections σ_{NN}, so that the rapidity distributions become much narrower as shown in the left panels of Fig. 5.9. In addition, the triton multiplicity was improved by modifying the phase space so that the bound phase space for the relative coordinate between a two-nucleon pair and another nucleon becomes approximately $(2\pi\hbar)^3$ [13]. We label this parameter set as AMD$^{(\mathrm{S})}$. The yield of ^{4}He could be improved by adjusting the in-medium cluster correlations, which was, however, not done in AMD$^{(\mathrm{S})}$. A steadily observed problem is that the $t/^3$He yield ratio is always underestimated, either by AMD$^{(\mathrm{F})}$ or AMD$^{(\mathrm{S})}$.

In Fig. 5.10, the p_T/A spectra predicted by the AMD$^{(\mathrm{S})}$ and AMD$^{(\mathrm{F})}$ are depicted

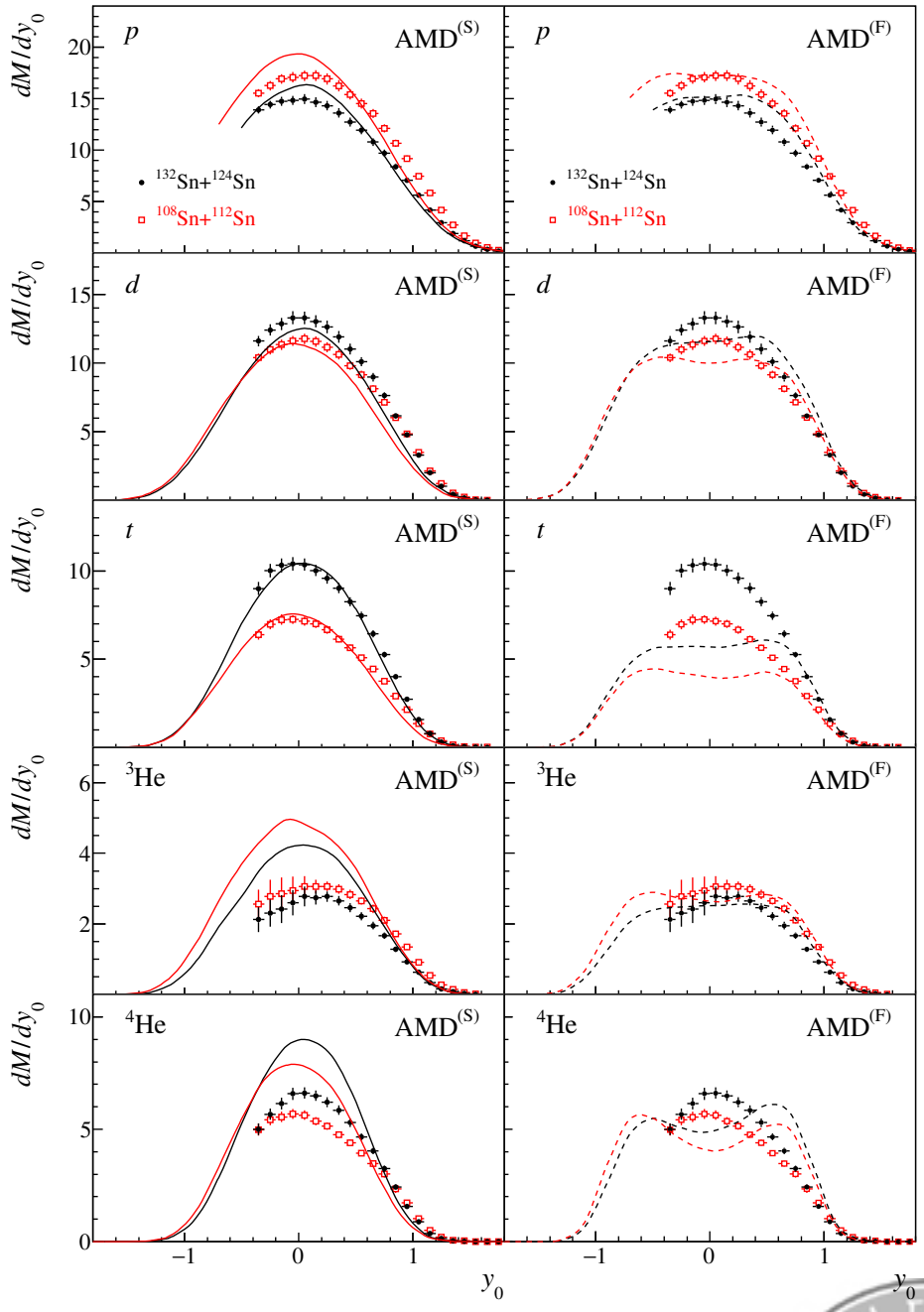

Figure 5.9 Rapidity distribution of ^{132}Sn + ^{124}Sn (black circle) ^{108}Sn + ^{112}Sn (red square) systems at 270 MeV/u. The experimental data (markers) are compared to the AMD$^{(S)}$ (left panels) and AMD$^{(F)}$ (right panels).

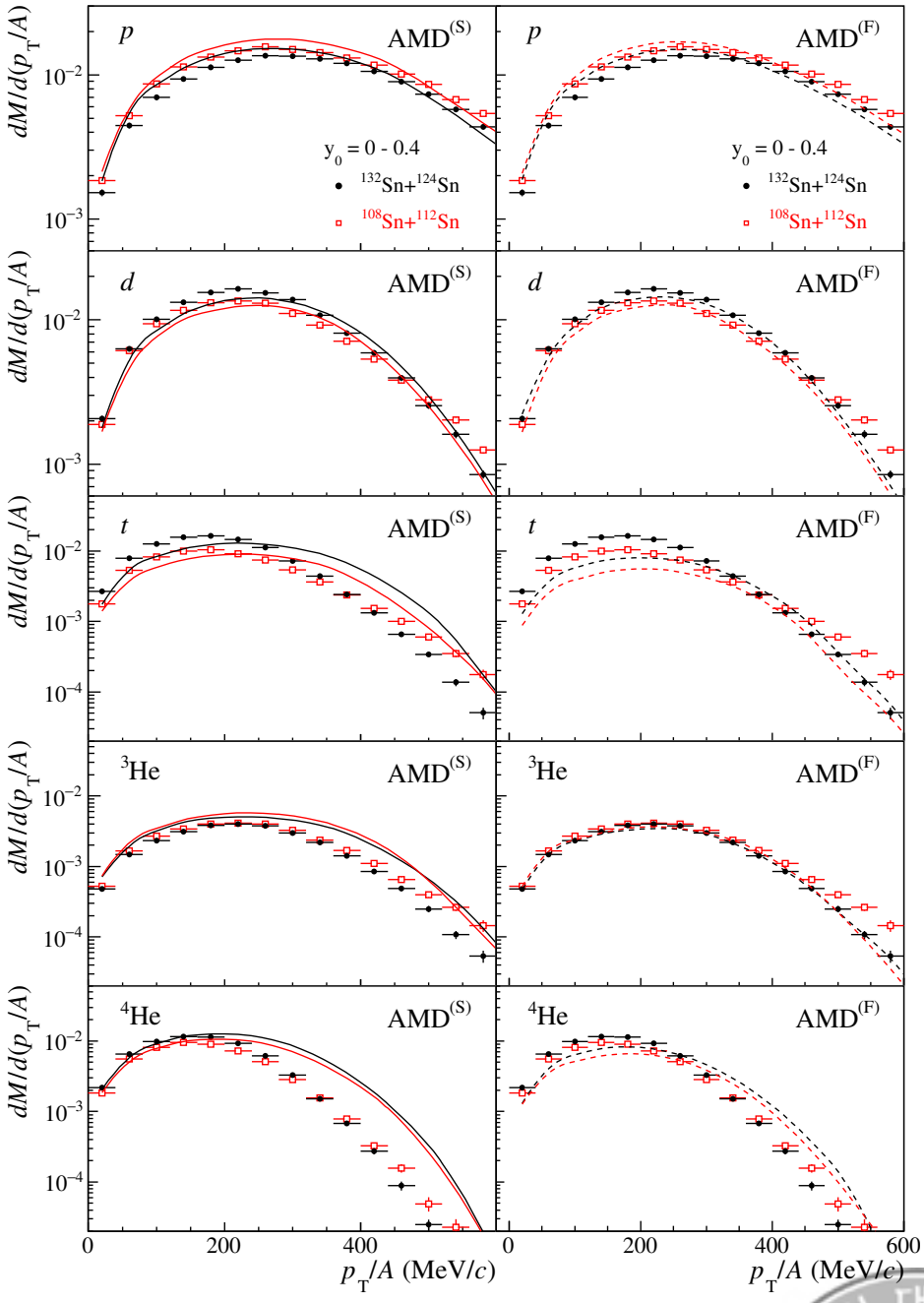

Figure 5.10 Transverse-momentum per nucleon distribution of ^{132}Sn + ^{124}Sn (black circle) ^{108}Sn + ^{112}Sn (red square) systems at 270 MeV/u. The experimental data (markers) are compared to the AMD$^{(S)}$ (left panels) and AMD$^{(F)}$ (right panels). Mid-rapidity gate for y_0 = 0 - 0.4 is applied.

by the solid lines (left panels) and dotted lines (right panels), respectively. For proton and deuteron, the overall shapes and absolute yields are well explained with both AMD$^{(S)}$ and AMD$^{(F)}$. On the other hand, for clusters with $A \geq 3$, the shapes of the p_T/A spectra change significantly when the in-medium cross sections σ_{NN} are increased from AMD$^{(F)}$ to AMD$^{(S)}$, and the spectra extend to high p_T/A in AMD$^{(S)}$ compared to the experimental data. The change from AMD$^{(F)}$ to AMD$^{(S)}$ is understood as a natural consequence of the increased σ_{NN} to reduce $\langle p_z^2 \rangle$ and increase $\langle p_T^2 \rangle$. To reproduce the experimental data of both the rapidity and p_T/A distributions, both $\langle p_z^2 \rangle$ and $\langle p_T^2 \rangle$ of clusters need to be reduced, in particular for tritons, but it is not possible by changing σ_{NN} in AMD.

For the low energy particles with $p_T/A < 280$ MeV/c, the behavior of R_{12} is qualitatively explained by AMD without depending much on the parameter set, AMD$^{(F)}$ or AMD$^{(S)}$. The predicted R_{21} values are shown as bands in the middle and bottom panels of Fig. 5.7. The widths of the bands represent statistical uncertainties. The predicted R_{21} for all particles except proton show slightly lower values. Similar to SMM, the R_{12} of tritons shows the largest difference in the model comparisons.

In Fig. 5.11, AMD$^{(F)}$ (left panels) and AMD$^{(S)}$ (right panels) are fitted with Eq. 5.2 in $p_T/A < 280$ MeV/c. The neutron R_{21} value is shown as a star marker, but it is not fitted together with hydrogen and helium isotopes. The fitted scaling values $(\alpha, \beta)_{\mathrm{AMD}^{(F)}} = (0.25, -0.18)$ and $(\alpha, \beta)_{\mathrm{AMD}^{(S)}} = (0.25, -0.20)$ are not comparable to experimental data $(\alpha, \beta)_{\mathrm{exp}} = (0.29, -0.23)$, The isoscaling fit of AMD for each p_T/A range with an interval of 80 MeV/c can be found in Section B. Although the neutron yield of experimental data is not analyzed in this work, the neutron yield ratio of AMD$^{(F)}$ and AMD$^{(S)}$ is fitted together with hydrogen and helium isotopes as shown in Fig. 5.12.

An emergence of isoscaling in the AMD calculation is not trivial because AMD does not assume any equilibrium state, and the fragments are produced within a rapidly evolving system [47]. However, clusters are repeatedly created and broken by the microscopic processes explained above during the dynamical evolution. Therefore

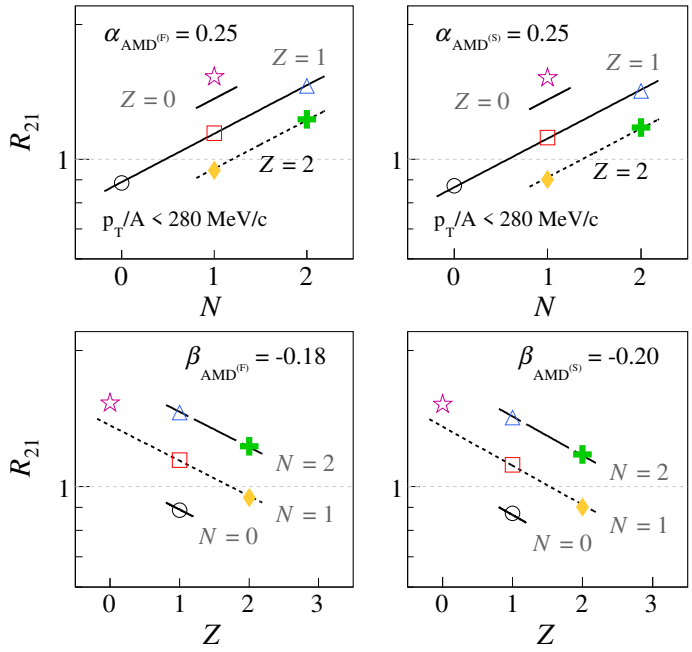

Figure 5.11 Isoscaling fit of AMD$^{(F)}$ (left) and AMD$^{(S)}$ (right) without neutron. The neutron point (star) is not fitted but plotted just for the reference.

a situation similar to a chemical equilibrium may be realized before particles stop interacting. The isoscaling observed in AMD is consistent with such a picture, at least qualitatively. The precise values of R_{12} may depend on the details of the model ingredients. However, the steep drop of R_{12} of clusters at high p_T down to $R_{12} < 1$ in the experimental data seems to be difficult to explain by a minor modification of the present AMD model. Direct information on free neutrons can be an essential clue to solving this puzzle.

5.5 Conclusion

In summary, the isoscaling phenomenon of hydrogen and helium isotopes ^{132}Sn + ^{124}Sn and ^{108}Sn + ^{112}Sn reactions at a beam energy of 270 MeV/u is presented as a function of p_T/A. The collision systems are found to form a thermal equilibrium

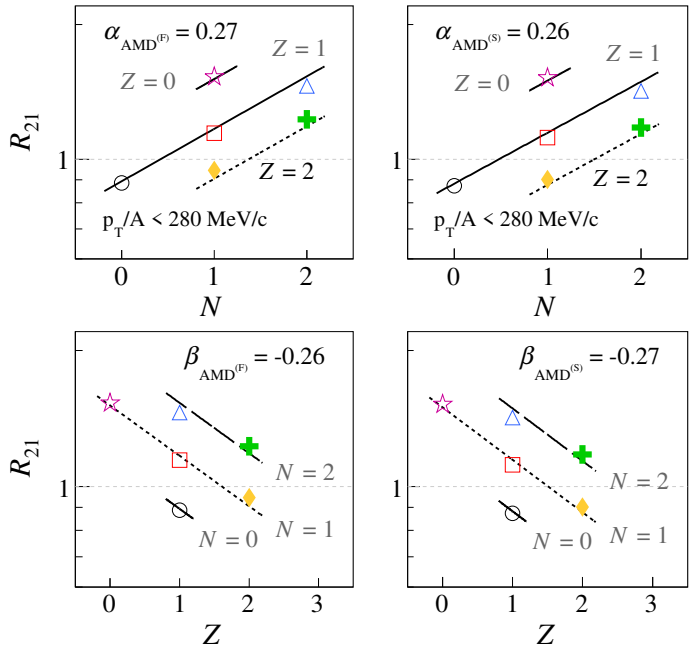

Figure 5.12 Isoscaling fit of AMD$^{(F)}$ (left) and AMD$^{(S)}$ (right) with neutron.

locally, evident from the increasing trend of H-He double ratio temperature with increasing p_T/A. The isoscaling phenomenon is visible up to $p_T/A < 280$ MeV/c. The R_{21} distribution shows clear $(N - Z)$ groups, and a good fit is given with isoscaling law as a function of N and Z in this range. On the other hand, isoscaling breaks in the above range of $p_T/A > 280$ MeV/c. In this range, the R_{21} of Helium isotopes break down together as p_T/A increases, and fit with isoscaling law is unattainable with these R_{21} values. Both the SMM and AMD models can qualitatively explain the isoscaling. When the yield spectra and isoscaling are compared to the predictions from the dynamical model AMD with two different parameter sets, we do not find any preference in increasing the default values of σ_{NN} as observed in an earlier study of Z=1 particles. While isoscaling breaks down for $p_T/A > 280$ MeV/c particles in the data, the isoscaling trend in AMD persists. Most intriguingly, the high-momentum clusters are suppressed in the neutron-rich system compared to the more isospin-

symmetric system, suggesting the non-equilibrium nature of the emission process, especially for the high-energy particles.

Appendix A

Systematic Uncertainties

The following Tables and Figures in this section show a detailed systematic analysis of p_T/A and y_0 distributions for each particle varied by the different cuts. The selected cuts and variations can be found in Table. 4.3. For example, Figure A.1 shows the p_T/A distribution and a systematic error of proton. The different colors and markers show the error calculated from these changes in the middle panel. A red dashed line draws the statistical error for reference. In this case, it is shown that the charged particle multiplicity cut makes a slight difference compared to the other cuts. The distance to vertex cut of 11 mm contributes mainly for p_T/A below ~ 450 while the number of cluster cut is the main contribution in the high p_T/A region. In the bottom panel, the error is shown in the log plot. The most significant error among quality cuts for each p_T/A and y_0 range are summarized in Table A.1 and A.2.

	$p_T/A \pm 20$ MeV/c														
	20	60	100	140	180	220	260	300	340	380	420	460	500	540	580
p (Y_2)	4.5	4.6	4.3	4.0	4.0	3.7	3.6	3.2	3.3	3.0	2.8	2.7	2.6	3.6	3.8
p (Y_1)	3.9	3.9	4.7	4.0	3.8	3.6	3.1	3.4	3.2	3.0	2.8	2.8	4.2	3.1	3.9
p (R_{21})	2.6	1.3	0.5	1.2	1.1	0.7	0.6	0.5	1.3	0.8	1.4	1.3	2.4	1.9	3.7
d (Y_2)	4.4	3.9	4.1	4.0	3.7	3.3	3.4	2.9	3.1	3.3	3.5	4.1	4.1	5.6	5.1
d (Y_1)	4.3	3.4	3.5	3.4	3.1	3.1	2.9	3.0	3.7	4.3	3.7	4.1	4.2	4.6	3.3
d (R_{21})	3.8	1.1	0.8	1.0	0.7	1.0	1.4	0.8	1.2	2.4	1.2	2.2	2.5	3.2	2.7
t (Y_2)	4.1	3.9	3.1	3.2	3.1	2.7	2.8	3.2	3.4	3.4	6.3	6.1	5.8	8.1	13.4
t (Y_1)	3.5	3.6	3.6	2.9	2.8	3.0	3.0	3.4	5.7	5.2	4.4	4.8	7.2	8.3	12.5
t (R_{21})	0.8	3.2	2.9	1.2	1.5	1.3	1.6	2.0	3.2	2.4	8.9	6.1	7.2	9.8	17.1
^{3}He (Y_2)	6.4	5.2	5.1	5.1	5.3	4.7	5.6	5.4	6.0	5.8	7.2	6.5	7.6	8.4	14.5
^{3}He (Y_1)	6.0	5.6	5.4	5.3	4.8	4.1	4.0	3.9	4.2	4.8	3.0	7.7	5.6	5.5	15.5
^{3}He (R_{21})	3.5	3.8	2.7	1.4	0.8	0.6	1.8	2.4	2.4	1.8	4.3	6.9	4.0	5.7	11.3
^{4}He (Y_2)	5.3	4.2	3.8	3.2	3.4	3.0	3.0	3.9	4.2	6.2	7.2	10.7	8.7	50.1	69.5
^{4}He (Y_1)	4.7	3.3	3.2	3.1	2.9	2.2	2.8	2.7	3.1	5.6	6.4	9.2	16.0	19.2	50.3
^{4}He (R_{21})	2.8	1.6	1.2	0.8	1.1	1.1	1.6	1.5	1.2	10.0	4.9	9.3	13.8	42.6	62.5

Table A.1 The overall systematic errors (%) in each p_T/A bin for the rapidity range of y_0 = 0 - 0.4. p_T/A range for each column is $\pm$ 20 MeV/c from the center value. Y_2, Y_1 and R_21 are the yield of ^{132}Sn + ^{124}Sn, yield of ^{108}Sn + ^{112}Sn and yield ratio between ^{132}Sn + ^{124}Sn and ^{108}Sn + ^{112}Sn.

	$y_0 \pm 0.1$																						
	-0.35	-0.25	-0.15	-0.05	0.05	0.15	0.25	0.35	0.45	0.55	0.65	0.75	0.85	0.95	1.05	1.15	1.25	1.35	1.45	1.55	1.65	1.75	1.85	1.95
p (Y_1)	2.6	2.6	2.9	2.9	3.1	3.2	3.2	3.4	3.4	3.4	3.5	3.6	3.3	3.2	3.2	3.4	3.2	2.9	3	5.2	3.1	5.2	4.8	
p (Y_2)	2.5	2.7	2.6	2.8	2.9	3	3.1	3.4	3.3	3.3	3.1	3.2	3.3	3.1	3	3.4	3.1	3.4	2.9	3.2	4.2	4.5	3.8	4.3
d (Y_1)	3.2	3.3	3.4	3.5	3.4	3.4	3.6	3.5	3.5	3.3	3.5	3.3	3.1	3.1	3.3	3.4	3.3	5.5	3.6	11	14	0	0	0
d (Y_2)	3	3.1	3.2	3.1	3.1	3.2	3.3	3.3	3	3.1	3	2.9	3.2	2.7	2.6	3	3.2	3.8	4.7	9.2	22	40	0	0
t (Y_1)	4.1	3.7	3.8	3.6	3.3	3.2	3.3	3.2	3.1	3	3	3	2.6	2.7	3.5	3.2	7.1	4.4	5.4	16	17	52	0	0
t (Y_2)	4.3	3.9	4	3.2	3.3	3.3	3.4	3	3	3.1	2.8	3	2.5	2.4	2.7	3.9	4.2	6.1	9.1	18	23	120	99	0
^{3}He (Y_1)	17	17	16	14	10	7.1	5.2	4.9	5.2	5.1	5.3	5.5	5.4	5.8	7.7	9.8	11	16	16	30	0	0	0	0
^{3}He (Y_2)	16	17	16	14	9.5	6.2	4.4	4.3	4.5	3.8	4.8	4.6	4.7	5.9	5.8	7.9	11	13	21	17	100	0	0	0
^{4}He (Y_1)	5.3	4.4	4.2	3.9	3.7	3.5	3.5	3.4	3.6	3.1	3.3	4	5.1	7.1	7.4	10	14	17	22	32	200	0	0	0
^{4}He (Y_2)	5.3	4.7	4.1	3.8	3.6	3.2	3.1	2.7	2.8	2.8	3.5	5.1	7.8	7.2	8.1	7.3	9.4	16	27	25	0	0	0	0

Table A.2 The overall systematic errors (%) in each y_0 bin. y_0 range for each column is $\pm$ 0.1 from the center value. Y_2, Y_1 and R_21 are the yield of ^{132}Sn + ^{124}Sn, yield of ^{108}Sn + ^{112}Sn and yield ratio between ^{132}Sn + ^{124}Sn and ^{108}Sn + ^{112}Sn.

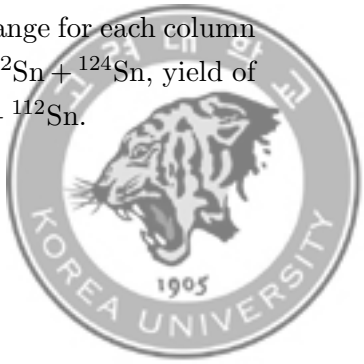

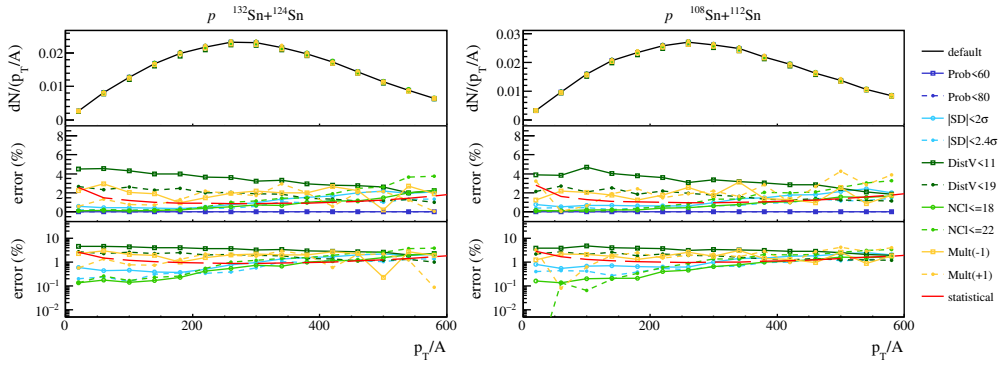

Figure A.1 p_T/A distributions and corresponding systematic errors of proton from the variations of different cuts.

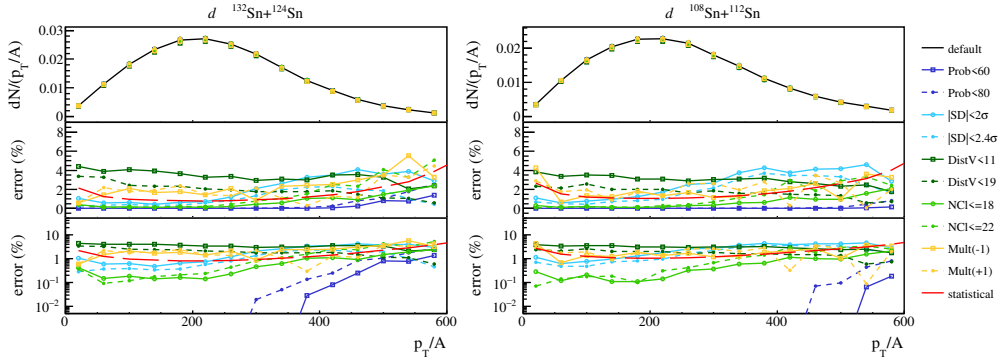

Figure A.2 p_T/A distributions and corresponding systematic errors of deuteron from the variations of different cuts.

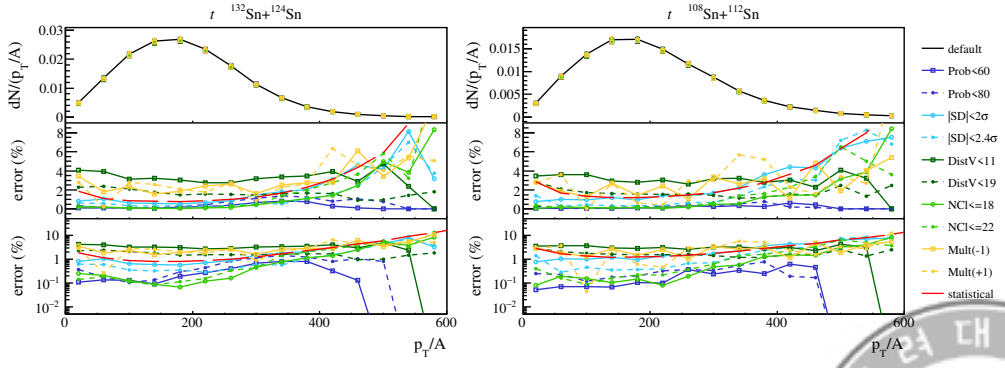

Figure A.3 p_T/A distributions and corresponding systematic errors of triton from the variations of different cuts.

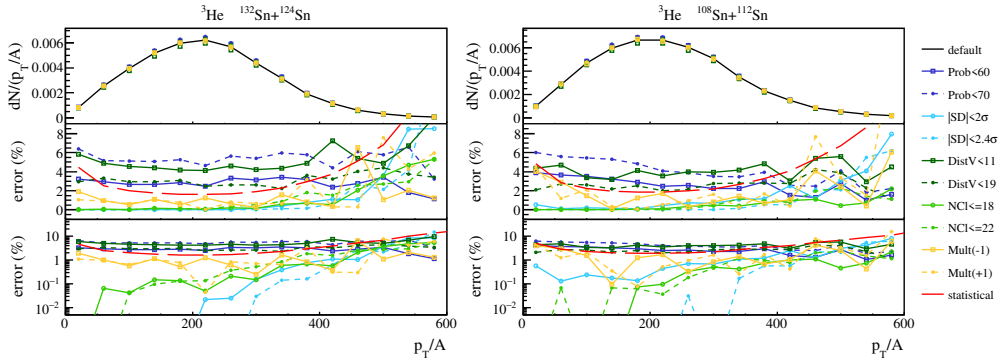

Figure A.4 p_T/A distributions and corresponding systematic errors of ^{3}He from the variations of different cuts.

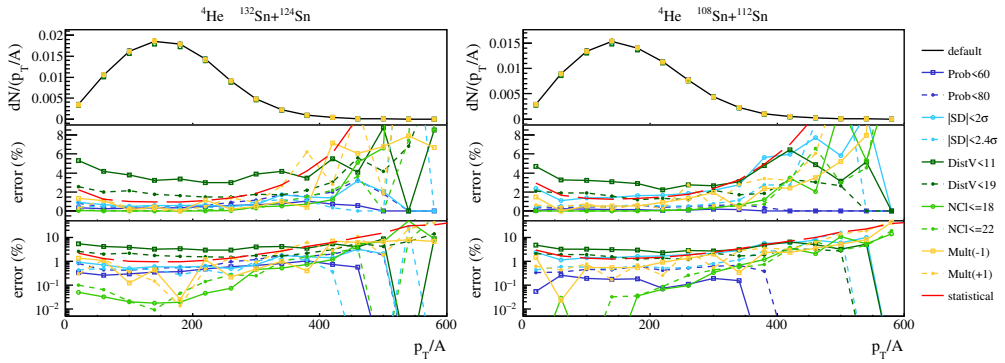

Figure A.5 p_T/A distributions and corresponding systematic errors of ^{4}He from the variations of different cuts.

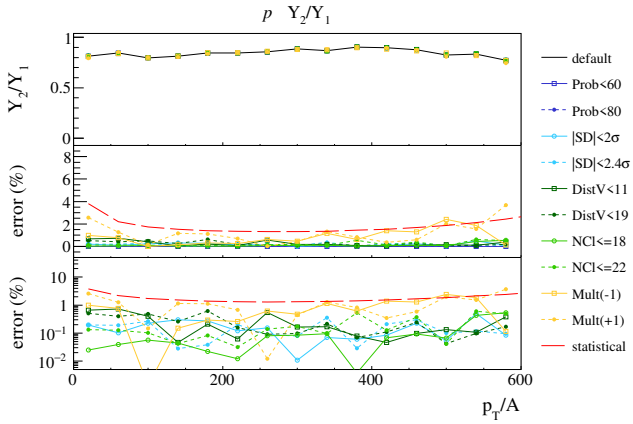

Figure A.6 p_T/A distributions and corresponding systematic errors of proton yield ratio between ^{132}Sn + ^{124}Sn and ^{108}Sn + ^{112}Sn from the variations of different cuts.

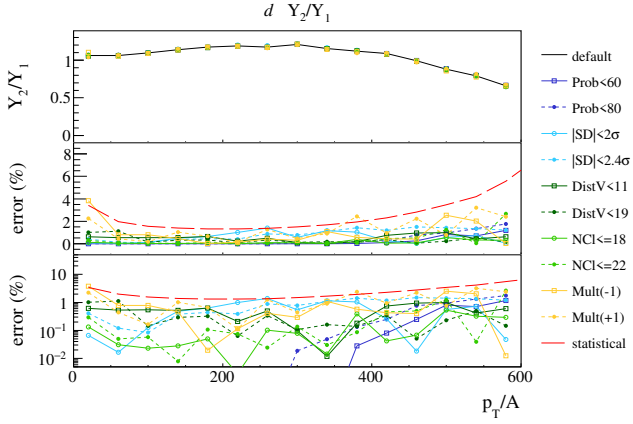

Figure A.7 p_T/A distributions and corresponding systematic errors of deuteron yield ratio between ^{132}Sn + ^{124}Sn and ^{108}Sn + ^{112}Sn from the variations of different cuts.

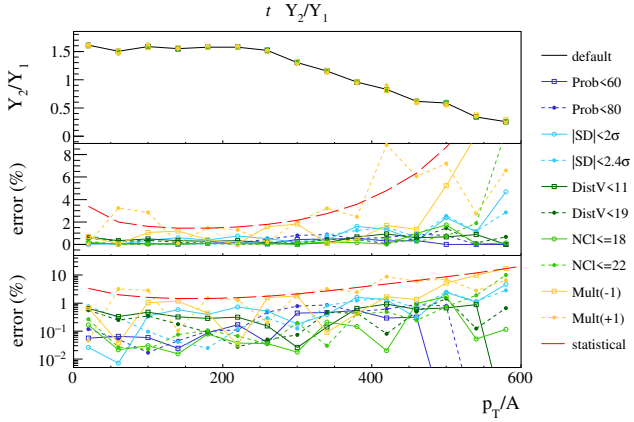

Figure A.8 p_T/A distributions and corresponding systematic errors of triton yield ratio between ^{132}Sn + ^{124}Sn and ^{108}Sn + ^{112}Sn from the variations of different cuts.

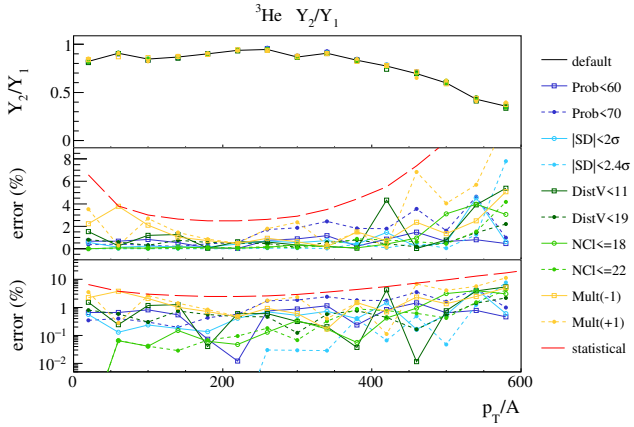

Figure A.9 p_T/A distributions and corresponding systematic errors of ^{3}He yield ratio between ^{132}Sn + ^{124}Sn and ^{108}Sn + ^{112}Sn from the variations of different cuts.

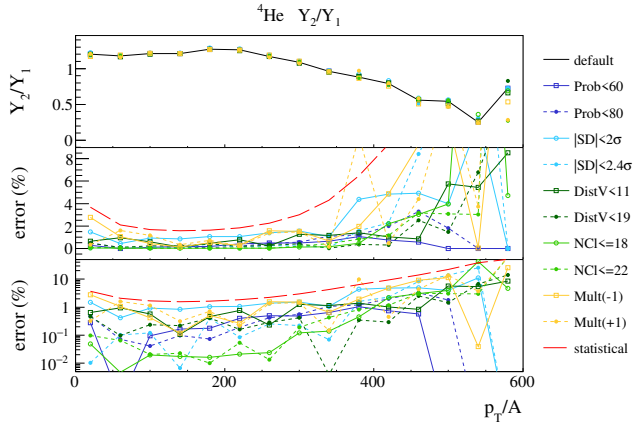

Figure A.10 p_T/A distributions and corresponding systematic errors of ^{4}He yield ratio between ^{132}Sn + ^{124}Sn and ^{108}Sn + ^{112}Sn from the variations of different cuts.

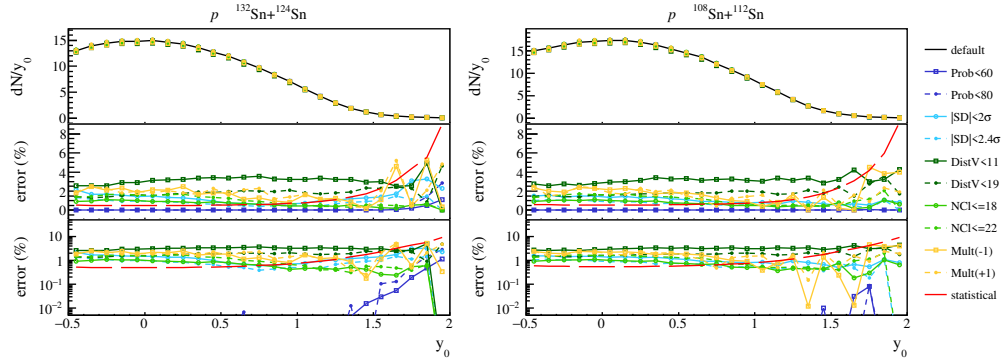

Figure A.11 y_0 distributions and corresponding systematic errors of proton from the variations of different cuts.

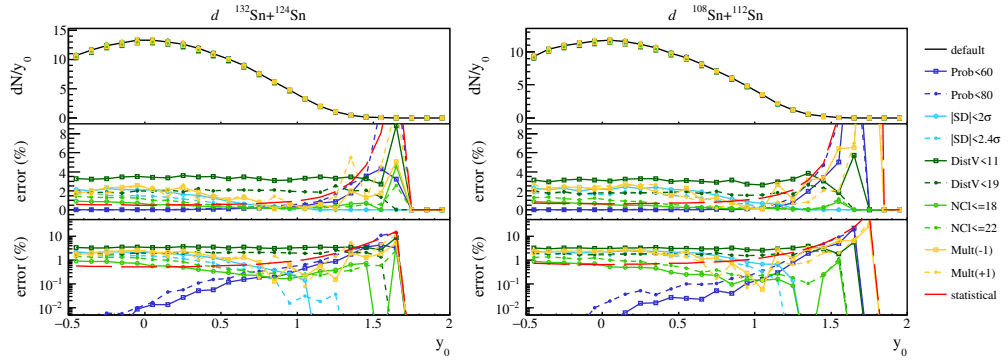

Figure A.12 y_0 distributions and corresponding systematic errors of deuteron from the variations of different cuts.

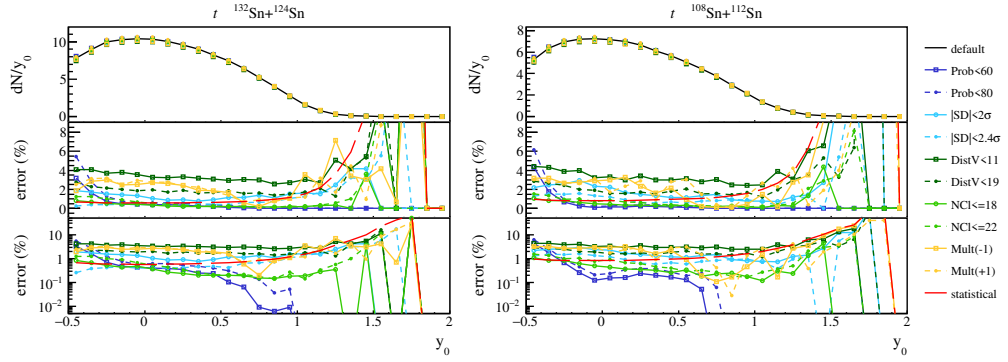

Figure A.13 y_0 distributions and corresponding systematic errors of triton from the variations of different cuts.

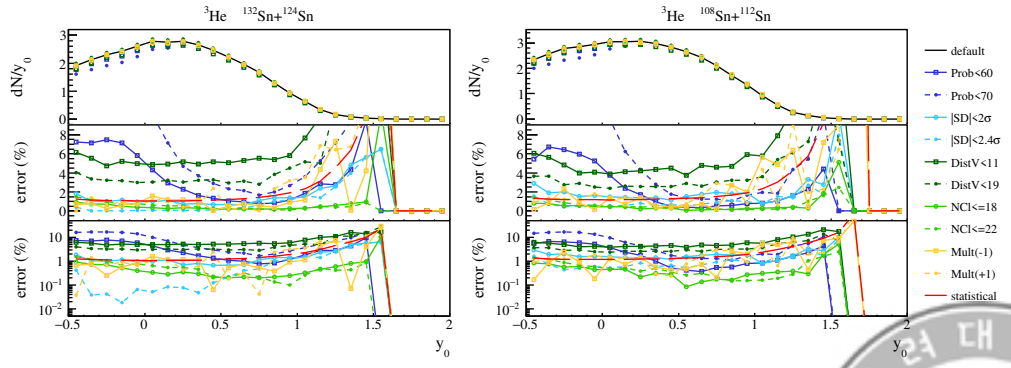

Figure A.14 y_0 distributions and corresponding systematic errors of ^{3}He from the variations of different cuts.

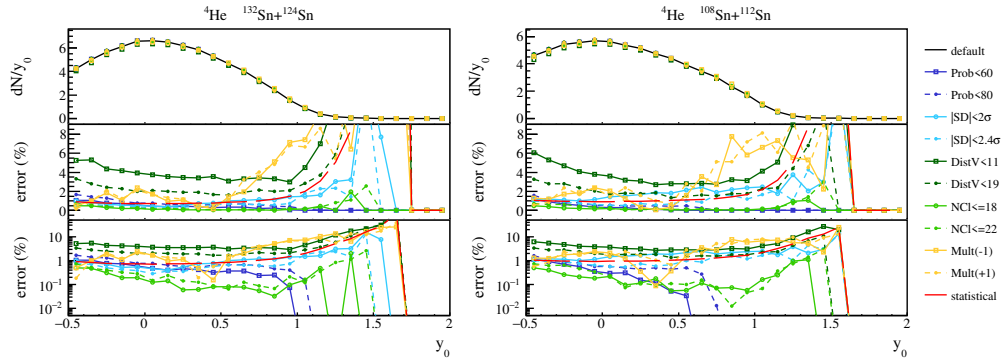

Figure A.15 y_0 distributions and corresponding systematic errors of ^{4}He from the variations of different cuts.

Appendix B

Isoscaling Fit Results

The Figures in this section show isoscaling fit for all ranges of p_T/A. The fits are performed where isoscaling is observed. This corresponds to $p_T/A < 280$ MeV/c for experimental data. For the ranges where isoscaling cannot be observed, isotopes and isotones are joined by a line to guide the eye. The data are simultaneously fitted for α and β, but α and β fits are shown separately as a function of N and Z.

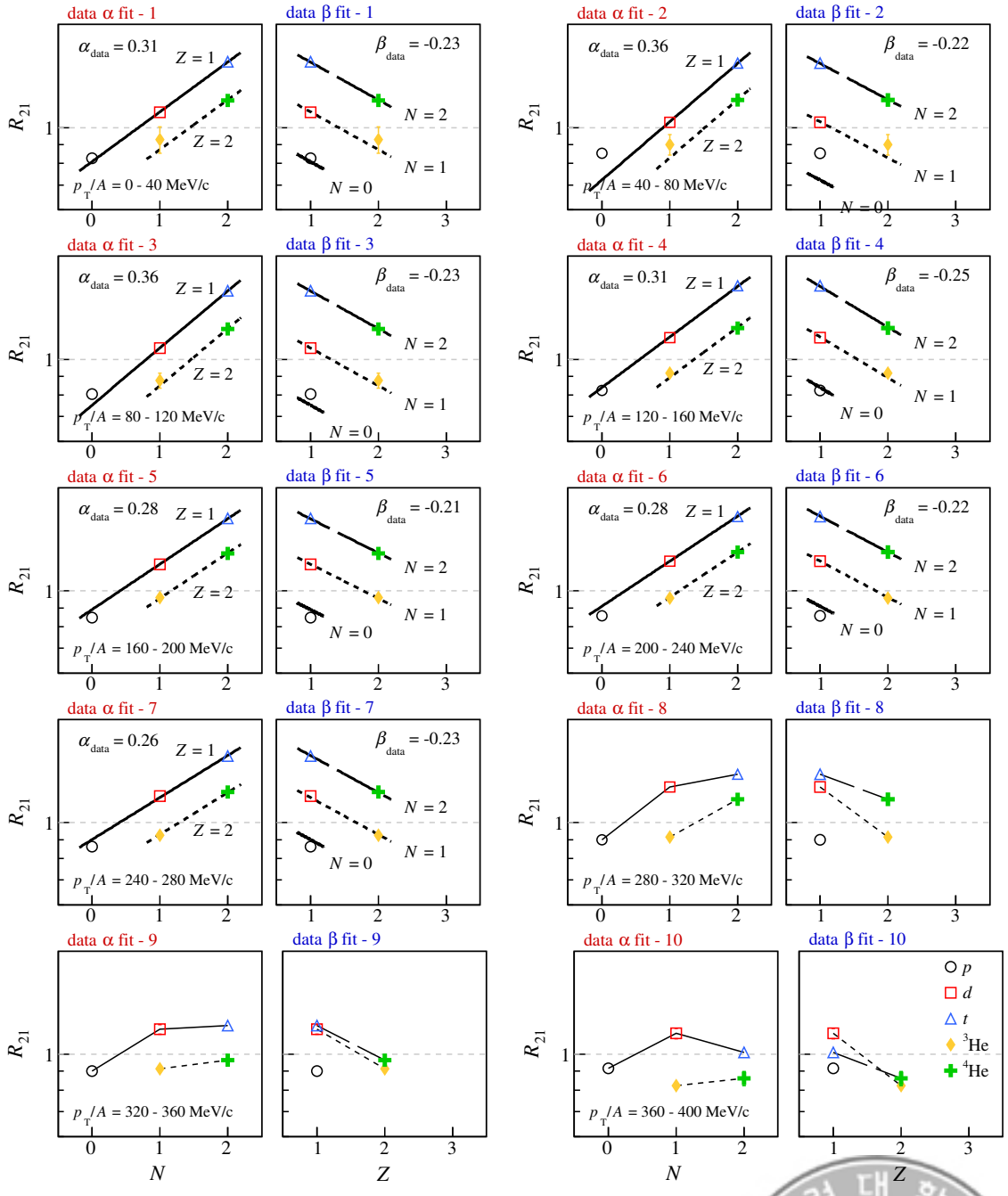

Figure B.1 Isoscaling fits from the experimental data. Each paired two-panels show the fit in p_T/A bins every 40 MeV/c. The range is noted in the α fit panels.

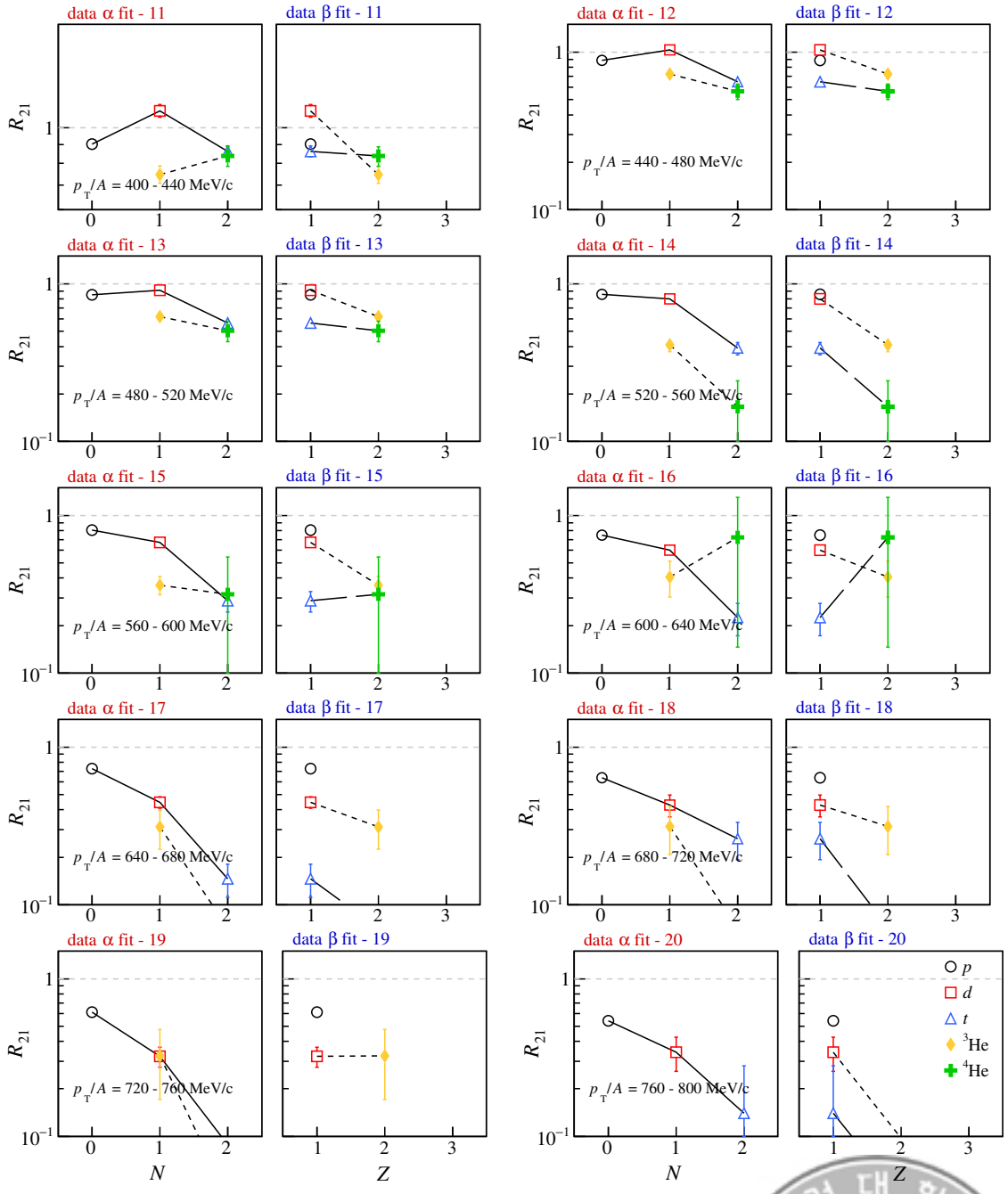

Figure B.2 Isoscaling fits from the experimental data. Each paired two-panels show the fit in p_T/A bins every 40 MeV/c. The range is noted in the α fit panels.

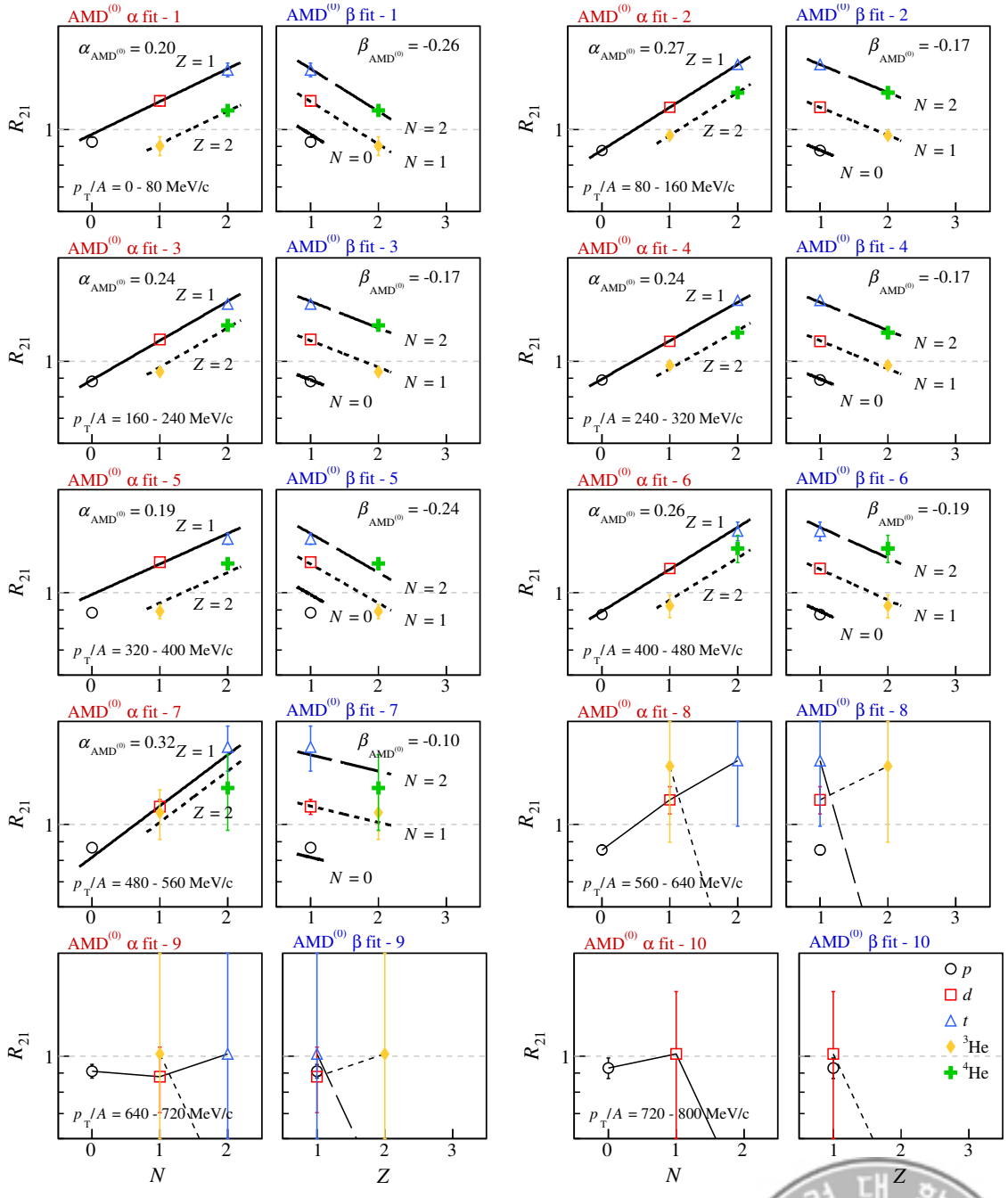

Figure B.3 Isoscaling fits from the AMD$^{(F)}$. Each paired two-panels show the fit in p_T/A bins every 80 MeV/c. The range is noted in the α fit panels.

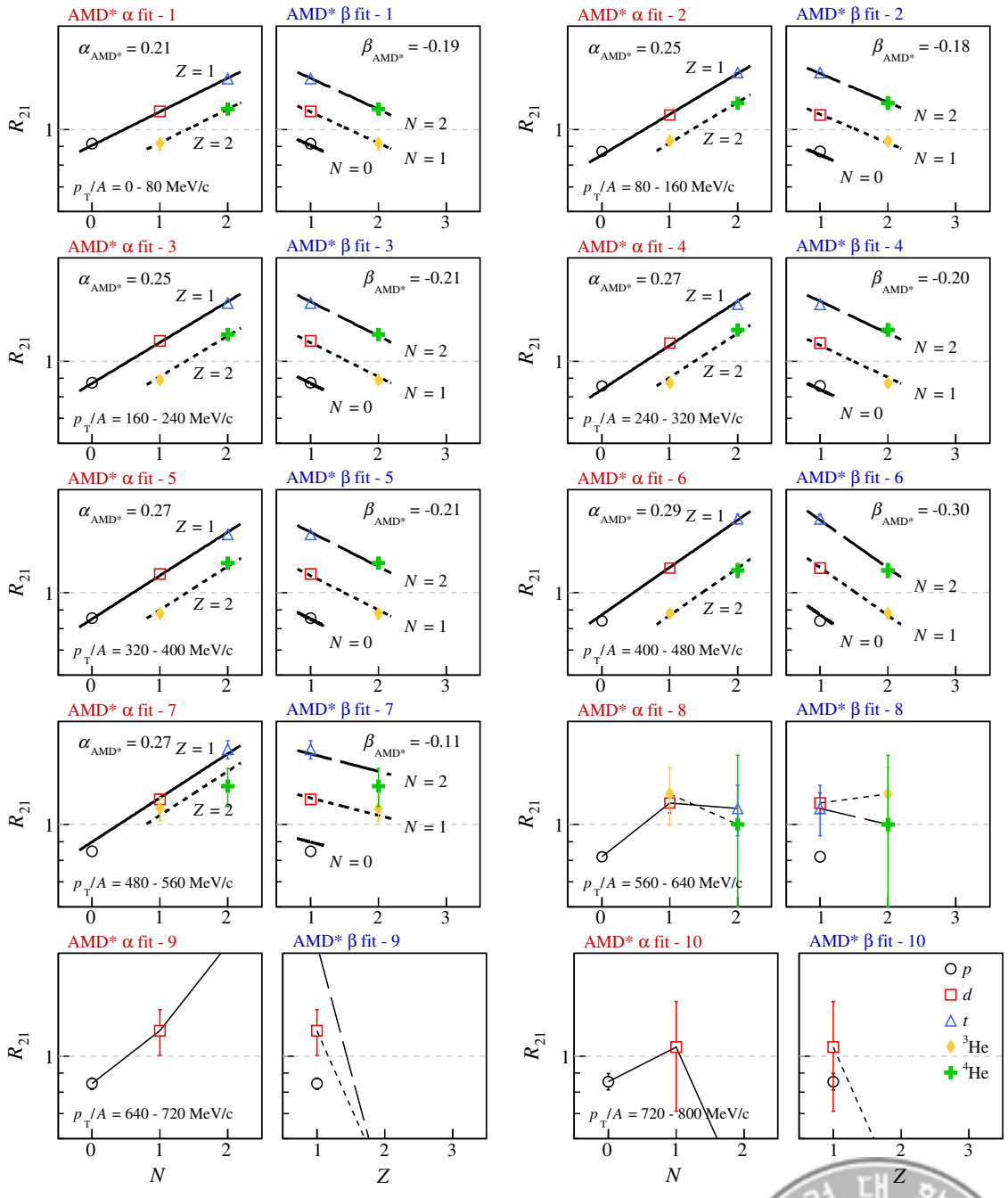

Figure B.4 Isoscaling fits from the AMD$^{(S)}$. Each paired two-panels show the fit in p_T/A bins every 80 MeV/c. The range is noted in the α fit panels.

Appendix C

Data

Table C.1 shows the list of runs used in the analysis. Followed tables summarize the experimental values of yield, yield ratio, and temperature discussed in Chapter 5. The data values are also summarized in the following link:
https://github.com/ejungwoo/spirit_isoscaling_data.

System	#runs	Run numbers
^{132}Sn + ^{124}Sn	113	2841, 2843, 2844, 2845, 2846, 2848, 2849, 2850, 2851, 2852, 2855, 2856, 2857
		2858, 2859, 2860, 2861, 2875, 2877, 2878, 2879, 2880, 2881, 2882, 2883, 2884
		2887, 2888, 2889, 2890, 2891, 2892, 2893, 2894, 2896, 2898, 2899, 2900, 2901
		2902, 2903, 2904, 2905, 2907, 2914, 2916, 2917, 2919, 2920, 2921, 2922, 2924
		2925, 2926, 2927, 2929, 2930, 2931, 2932, 2933, 2934, 2935, 2936, 2939, 2940
		2941, 2942, 2943, 2944, 2945, 2946, 2948, 2955, 2956, 2958, 2959, 2960, 2961
		2962, 2964, 2965, 2966, 2968, 2969, 2970, 2971, 2972, 2973, 2975, 2976, 2977
		2978, 2979, 2980, 2981, 2982, 2983, 2984, 2985, 2986, 2988, 2989, 2990, 2991
		2992, 2993, 2997, 2999, 3000, 3002, 3003, 3007, 3039
^{108}Sn + ^{112}Sn	85	2272, 2273, 2274, 2275, 2276, 2283, 2284, 2285, 2286, 2288, 2289, 2291, 2310
		2311, 2314, 2315, 2320, 2322, 2323, 2324, 2325, 2331, 2332, 2333, 2334, 2335
		2336, 2337, 2340, 2341, 2362, 2363, 2368, 2369, 2370, 2371, 2372, 2373, 2374
		2375, 2378, 2379, 2380, 2381, 2382, 2383, 2384, 2385, 2386, 2387, 2388, 2389
		2391, 2392, 2393, 2394, 2395, 2396, 2397, 2398, 2399, 2400, 2401, 2402, 2429
		2432, 2433, 2434, 2437, 2438, 2439, 2440, 2442, 2453, 2461, 2462, 2463, 2501
		2502, 2503, 2505, 2506, 2507, 2508, 2509
^{112}Sn + ^{124}Sn	60	2542, 2543, 2544, 2546, 2547, 2548, 2552, 2553, 2554, 2555, 2556, 2557, 2558
		2559, 2560, 2562, 2563, 2564, 2565, 2566, 2567, 2568, 2569, 2570, 2571, 2572
		2573, 2574, 2575, 2578, 2579, 2580, 2581, 2582, 2583, 2584, 2585, 2586, 2587
		2588, 2589, 2590, 2591, 2592, 2593, 2594, 2595, 2596, 2597, 2598, 2599, 2600
		2601, 2617, 2618, 2619, 2620, 2621, 2622, 2623
^{124}Sn + ^{112}Sn	68	3059, 3061, 3062, 3065, 3066, 3068, 3069, 3071, 3074, 3075, 3076, 3077, 3078
		3080, 3081, 3082, 3083, 3084, 3085, 3087, 3088, 3089, 3090, 3091, 3092, 3093
		3094, 3095, 3097, 3098, 3102, 3103, 3138, 3139, 3140, 3141, 3142, 3143, 3144
		3145, 3146, 3148, 3149, 3150, 3151, 3152, 3153, 3154, 3155, 3156, 3157, 3158
		3159, 3165, 3166, 3167, 3168, 3169, 3170, 3171, 3172, 3177, 3179, 3180, 3181
		3182, 3183, 3184

Table C.1 List of runs used in the analysis.

proton — SπRIT experiment Sn+Sn @ 270 MeV/u

	^{132}Sn + ^{124}Sn		^{108}Sn + ^{112}Sn		Yield Ratio	
p_T/A (MeV/c)	$\frac{dN}{d(p_T/A)}$ ($\times 10^4$)	error (%)	$\frac{dN}{d(p_T/A)}$ ($\times 10^4$)	error (%)	Y_2/Y_1 ($\times 1$)	error (%)
20 ± 20	15.2	4.52	18.4	4.52	0.826	2.58
60 ± 20	44.4	4.56	52	4.56	0.853	1.48
100 ± 20	69.7	4.33	86.6	4.33	0.805	1.18
140 ± 20	93.2	3.97	113	3.97	0.824	1.16
180 ± 20	113	3.99	133	3.99	0.847	1.11
220 ± 20	126	3.67	147	3.67	0.857	0.895
260 ± 20	135	3.62	157	3.62	0.862	0.867
300 ± 20	135	3.23	150	3.23	0.899	0.869
340 ± 20	129	3.34	143	3.34	0.901	1.31
380 ± 20	120	2.96	131	2.96	0.917	0.94
420 ± 20	105	2.79	117	2.79	0.901	1.39
460 ± 20	89.9	2.74	101	2.74	0.886	1.3
500 ± 20	73.1	2.63	86	2.63	0.85	2.39
540 ± 20	57.6	3.64	67.3	3.64	0.855	1.86
580 ± 20	43.6	3.77	53.9	3.77	0.809	3.67

Table C.2 Table of yield and yield ratio of the proton in Sn+Sn at 270 MeV/u from SπRIT experiment of Fig. 5.1 and Fig. 5.5. The $dN/d(p_T/A)$ is scaled by ($\times 10^4$).

deuteron — SπRIT experiment Sn+Sn @ 270 MeV/u

	^{132}Sn + ^{124}Sn		^{108}Sn + ^{112}Sn		Yield Ratio	
p_T/A (MeV/c)	$\frac{dN}{d(p_T/A)}$ ($\times 10^4$)	error (%)	$\frac{dN}{d(p_T/A)}$ ($\times 10^4$)	error (%)	Y_2/Y_1 ($\times 1$)	error (%)
20 ± 20	20.7	4.42	18.9	4.42	1.1	3.83
60 ± 20	63.1	3.9	61	3.9	1.03	1.23
100 ± 20	101	4.05	94.3	4.05	1.07	0.965
140 ± 20	133	3.95	116	3.95	1.14	1.02
180 ± 20	155	3.67	131	3.67	1.18	0.801
220 ± 20	163	3.29	136	3.29	1.2	1
260 ± 20	154	3.39	130	3.39	1.18	1.4
300 ± 20	138	2.92	111	2.92	1.25	0.896
340 ± 20	107	3.1	92	3.1	1.17	1.15
380 ± 20	80.7	3.29	70.9	3.29	1.14	2.43
420 ± 20	59.2	3.51	53.4	3.51	1.11	1.43
460 ± 20	39.5	4.1	38.3	4.1	1.03	2.23
500 ± 20	25.4	4.07	28	4.07	0.909	2.53
540 ± 20	16.1	5.56	20.2	5.56	0.799	3.2
580 ± 20	8.46	5.06	12.5	5.06	0.676	3.87

Table C.3 Table of yield and yield ratio of the deuteron in Sn+Sn at 270 MeV/u from SπRIT experiment of Fig. 5.1 and Fig. 5.5. The $dN/d(p_T/A)$ is scaled by ($\times 10^4$).

triton — SπRIT experiment Sn+Sn @ 270 MeV/u

	^{132}Sn + ^{124}Sn		^{108}Sn + ^{112}Sn		Yield Ratio	
p_T/A (MeV/c)	$\frac{dN}{d(p_T/A)}$ ($\times 10^4$)	error (%)	$\frac{dN}{d(p_T/A)}$ ($\times 10^4$)	error (%)	Y_2/Y_1 ($\times 1$)	error (%)
20 ± 20	26.7	4.08	17.7	4.08	1.51	1.85
60 ± 20	78.8	3.93	52.8	3.93	1.49	3.22
100 ± 20	126	3.14	82.5	3.14	1.53	2.86
140 ± 20	157	3.24	99.2	3.24	1.58	1.18
180 ± 20	163	3.06	104	3.06	1.57	1.48
220 ± 20	146	2.74	91.7	2.74	1.59	1.3
260 ± 20	112	2.78	74	2.78	1.52	1.56
300 ± 20	72.6	3.2	53.8	3.2	1.35	2.04
340 ± 20	43.6	3.36	36.4	3.36	1.2	3.21
380 ± 20	24.1	3.44	23.8	3.44	1.01	2.45
420 ± 20	13.1	6.32	15.2	6.32	0.863	8.87
460 ± 20	6.52	6.1	10	6.1	0.649	6.07
500 ± 20	3.37	5.89	6	5.89	0.563	7.2
540 ± 20	1.37	9	3.5	9	0.39	9.76
580 ± 20	0.505	13.4	1.76	13.4	0.287	17.1

Table C.4 Table of yield and yield ratio of the triton in Sn+Sn at 270 MeV/u from SπRIT experiment of Fig. 5.1 and Fig. 5.5. The $dN/d(p_T/A)$ is scaled by ($\times 10^4$).

^{3}He — SπRIT experiment Sn+Sn @ 270 MeV/u

	^{132}Sn + ^{124}Sn		^{108}Sn + ^{112}Sn		Yield Ratio	
p_T/A (MeV/c)	$\frac{dN}{d(p_T/A)}$ ($\times 10^4$)	error (%)	$\frac{dN}{d(p_T/A)}$ ($\times 10^4$)	error (%)	Y_2/Y_1 ($\times 1$)	error (%)
20 ± 20	4.38	6.4	4.71	6.4	0.929	4.46
60 ± 20	13.7	5.17	15.3	5.17	0.9	3.79
100 ± 20	21.6	5.11	24.6	5.11	0.877	2.68
140 ± 20	29.1	5.07	31.7	5.07	0.918	1.76
180 ± 20	36	5.26	37.5	5.26	0.96	1.63
220 ± 20	37.3	4.65	38.9	4.65	0.958	1.61
260 ± 20	35	5.64	37.9	5.64	0.924	1.78
300 ± 20	28.2	5.4	30.8	5.4	0.914	2.37
340 ± 20	20.5	5.97	22.5	5.97	0.914	2.44
380 ± 20	13.3	5.79	16.1	5.79	0.824	2.95
420 ± 20	7.98	7.22	10.7	7.22	0.747	4.32
460 ± 20	4.62	6.55	6.36	6.55	0.726	6.85
500 ± 20	2.38	7.57	3.85	7.57	0.618	6.79
540 ± 20	1.05	9.94	2.55	9.94	0.41	9.94
580 ± 20	0.513	14.5	1.42	14.5	0.361	13.2

Table C.5 Table of yield and yield ratio of the ^{3}He in Sn+Sn at 270 MeV/u from SπRIT experiment of Fig. 5.1 and Fig. 5.5. The $dN/d(p_T/A)$ is scaled by ($\times 10^4$).

^{4}He — SπRIT experiment Sn+Sn @ 270 MeV/u

	^{132}Sn + ^{124}Sn		^{108}Sn + ^{112}Sn		Yield Ratio	
p_T/A (MeV/c)	$\frac{dN}{d(p_T/A)}$ ($\times 10^4$)	error (%)	$\frac{dN}{d(p_T/A)}$ ($\times 10^4$)	error (%)	Y_2/Y_1 ($\times 1$)	error (%)
20 ± 20	21.7	5.32	18.3	5.32	1.18	2.77
60 ± 20	65.8	4.17	55.5	4.17	1.19	1.61
100 ± 20	98.6	3.79	81.6	3.79	1.21	1.16
140 ± 20	116	3.21	95.4	3.21	1.21	0.947
180 ± 20	114	3.35	90	3.35	1.26	1.05
220 ± 20	92.9	2.97	72.9	2.97	1.27	1.09
260 ± 20	61.7	2.98	51	2.98	1.21	1.57
300 ± 20	32.8	3.9	28.4	3.9	1.16	1.87
340 ± 20	15.2	4.18	15.7	4.18	0.965	2.74
380 ± 20	6.76	6.2	7.86	6.2	0.86	9.98
420 ± 20	2.74	7.15	3.28	7.15	0.837	6.11
460 ± 20	0.889	10.7	1.58	10.7	0.563	9.82
500 ± 20	0.248	15	0.491	15	0.505	15
540 ± 20	0.0378	50.1	0.228	50.1	0.166	42.6
580 ± 20	0.0228	69.5	0.0723	69.5	0.316	62.5

Table C.6 Table of yield and yield ratio of the ^{4}He in Sn+Sn at 270 MeV/u from SπRIT experiment of Fig. 5.1 and Fig. 5.5. The $dN/d(p_T/A)$ is scaled by ($\times 10^4$).

He-H Temperature — SπRIT experiment Sn+Sn @ 270 MeV/u

	^{132}Sn + ^{124}Sn		^{108}Sn + ^{112}Sn		^{112}Sn + ^{124}Sn		^{124}Sn + ^{112}Sn	
p_T/A (MeV/c)	$T_{\text{He-H}}$ (MeV)	error (MeV)	$T_{\text{He-H}}$ (MeV)	error (MeV)	$T_{\text{He-H}}$ (MeV)	error (MeV)	error (Mev)	$T_{\text{He-H}}$ (MeV)
20 ± 20	8.341	0.5718	8.056	0.5289	9.199	1.067	7.74	0.9279
60 ± 20	8.25	0.4401	7.914	0.3978	7.853	0.5222	7.538	0.5142
100± 20	8.509	0.4343	8.359	0.424	8.342	0.5238	8.243	0.5802
140± 20	8.855	0.4508	8.685	0.4288	9.155	0.5695	8.519	0.4786
180± 20	9.547	0.5205	9.488	0.4733	9.795	0.5677	10.05	0.6494
220± 20	10.01	0.515	10.02	0.4903	10.01	0.5936	9.543	0.5869
260± 20	11.19	0.7128	11.21	0.6302	11.68	0.8529	10.8	0.7737
300± 20	11.96	0.8537	13.59	0.9833	13.25	1.179	12.73	1.221
340± 20	14.37	1.374	14.46	1.443	14.67	2.008	14.81	1.906
380± 20	15.24	1.835	17.91	2.708	17.89	2.996	23.93	7.333
420± 20	16.89	2.952	28.03	7.077	22.64	5.93	18.61	6.714

Table C.7 Table of He-H temperature as a function of p_T/A. The table correspond to Fig. 5.4

References

[1] B. Alex Brown, "Neutron radii in nuclei and the neutron equation of state," *Phys. Rev. Lett.*, vol. 85, pp. 5296–5299, 2000.

[2] M. B. Tsang, J. R. Stone, F. Camera, P. Danielewicz, S. Gandolfi, K. Hebeler, C. J. Horowitz, J. Lee, W. G. Lynch, Z. Kohley, R. Lemmon, P. Möller, T. Murakami, S. Riordan, X. Roca-Maza, F. Sammarruca, A. W. Steiner, I. Vidaña, and S. J. Yennello, "Constraints on the symmetry energy and neutron skins from experiments and theory," *Phys. Rev. C*, vol. 86, p. 015803, 2012.

[3] S. Hudan, A. Chbihi, J. D. Frankland, A. Mignon, J. P. Wieleczko, G. Auger, N. Bellaize, B. Borderie, A. Botvina, R. Bougault, B. Bouriquet, A. M. Buta, J. Colin, D. Cussol, R. Dayras, D. Durand, E. Galichet, D. Guinet, B. Guiot, G. Lanzalone, Lautesse, F. Lavaud, Lecolley, R. Legrain, L. Neindre, O. Lopez, L. Manduci, J. Marie, L. Nalpas, J. Normand, M. Pârlog, P. Pawłowski, M. Pichon, E. Plagnol, M. F. Rivet, E. Rosato, R. Roy, J. Steckmeyer, G. Tăbăcaru, B. Tamain, A. van Lauwe, E. Vient, M. Vigilante, and C. Volant, "Characteristics of the fragments produced in central collisions of ^{129}Xe+$^{\mathrm{nat}}$Sn from 32a to 50 a mev," *Phys. Rev. C*, vol. 67, p. 064613, 2003.

[4] W. Reisdorf, A. Andronic, R. Averbeck, M. Benabderrahmane, O. Hartmann, N. Herrmann, K. Hildenbrand, T. Kang, Y. Kim, M. KiÅ¡, P. Koczon, T. Kress, Y. Leifels, M. Merschmeyer, K. Piasecki, A. Schuttauf, M. Stockmeier, V. Barret, Z. Basrak, N. Bastid, R. Caplar, P. Crochet, P. Dupieux, M. Dzelalija, Z. Fodor,

P. Gasik, Y. Grishkin, B. Hong, J. Kecskemeti, M. Kirejczyk, M. Korolija, R. Kotte, A. Lebedev, X. Lopez, T. Matulewicz, W. Neubert, M. Petrovici, F. Rami, M. Ryu, Z. Seres, B. Sikora, K. Sim, V. Simion, K. Siwek-Wilczynska, V. Smolyankin, G. Stoicea, Z. Tyminski, K. Wisniewski, D. Wohlfarth, Z. Xiao, H. Xu, I. Yushmanov, and A. Zhilin, "Systematics of central heavy ion collisions in the 1a gev regime," *Nuclear Physics A*, vol. 848, pp. 366–427, 2010.

[5] A. Ono, "Dynamics of clusters and fragments in heavy-ion collisions," *Progress in Particle and Nuclear Physics*, vol. 105, pp. 139–179, 2019.

[6] M. B. Tsang, W. A. Friedman, C. K. Gelbke, W. G. Lynch, G. Verde, and H. S. Xu, "Conditions for isoscaling in nuclear reactions," *Phys. Rev. C*, vol. 64, p. 041603, 2001.

[7] H. Okuno, N. Fukunishi, and O. Kamigaito, "Progress of ribf accelerators," *Progress of Theoretical and Experimental Physics*, vol. 2012, p. 03C002, 2012.

[8] R. Shane, A. McIntosh, T. Isobe, W. Lynch, H. Baba, J. Barney, Z. Chajecki, M. Chartier, J. Estee, M. Famiano, B. Hong, K. Ieki, G. Jhang, R. Lemmon, F. Lu, T. Murakami, N. Nakatsuka, M. Nishimura, R. Olsen, W. Powell, H. Sakurai, A. Taketani, S. Tangwancharoen, M. Tsang, T. Usukura, R. Wang, S. Yennello, and J. Yurkon, "Sπrit: A time-projection chamber for symmetry-energy studies," *Nuclear Instruments and Methods in Physics Research Section A: Accelerators, Spectrometers, Detectors and Associated Equipment*, vol. 784, pp. 513–517, 2015.

[9] T. Isobe, G. Jhang, H. Baba, J. Barney, P. Baron, G. Cerizza, J. Estee, M. Kaneko, M. Kurata-Nishimura, J. Lee, W. Lynch, T. Murakami, N. Nakatsuka, E. Pollacco, W. Powell, H. Sakurai, C. Santamaria, D. Suzuki, S. Tangwancharoen, and M. Tsang, "Application of the generic electronics for time projection chamber (get) readout system for heavy radioactive isotope collision experiments," *Nuclear Instruments and Methods in Physics Research Section*

A: Accelerators, Spectrometers, Detectors and Associated Equipment, vol. 899, pp. 43–48, 2018.

[10] J. B. Estee, *CHARGED PION EMISSION FROM NEUTRON-RICH HEAVY ION COLLISIONS FOR STUDIES ON THE SYMMETRY ENERGY.* PhD thesis, 2020.

[11] J. Estee, W. Lynch, J. Barney, G. Cerizza, G. Jhang, J. Lee, R. Wang, T. Isobe, M. Kaneko, M. Kurata-Nishimura, T. Murakami, R. Shane, S. Tangwancharoen, C. Tsang, M. Tsang, B. Hong, P. Lasko, J. Lukasik, A. McIntosh, P. PawLowski, K. Pelczar, H. Sakurai, C. Santamaria, D. Suzuki, S. Yennello, and Y. Zhang, "Extending the dynamic range of electronics in a time projection chamber," *Nuclear Instruments and Methods in Physics Research Section A: Accelerators, Spectrometers, Detectors and Associated Equipment*, vol. 944, p. 162509, 2019.

[12] M. Kaneko, *Hydrogen Isotope Productions in Sn + Sn Collisions with Radioactive Beams at 270 MeV/nucleon.* PhD thesis, 2022.

[13] M. Kaneko, T. Murakami, T. Isobe, M. Kurata-Nishimura, A. Ono, N. Ikeno, J. Barney, G. Cerizza, J. Estee, G. Jhang, J. Lee, W. Lynch, C. Santamaria, C. Tsang, M. Tsang, R. Wang, D. Ahn, L. Atar, T. Aumann, H. Baba, K. Boretzky, J. Brzychczyk, N. Chiga, N. Fukuda, I. Gasparic, B. Hong, A. Horvat, T. Ichihara, K. Ieki, N. Inabe, Y. Kim, T. Kobayashi, Y. Kondo, P. Lasko, H. Lee, Y. Leifels, J. Lukasik, J. Manfredi, A. McIntosh, P. Morfouace, T. Nakamura, N. Nakatsuka, S. Nishimura, R. Olsen, H. Otsu, P. Pawlowski, K. Pelczar, D. Rossi, H. Sakurai, H. Sato, H. Scheit, R. Shane, Y. Shimizu, H. Simon, T. Sumikama, D. Suzuki, H. Suzuki, H. Takeda, S. Tangwancharoen, Y. Togano, H. Tornqvist, Z. Xiao, S. Yennello, J. Yurkon, and Y. Zhang, "Rapidity distributions of z=1 isotopes and the nuclear symmetry energy from sn+sn collisions with radioactive beams at 270 mev/nucleon," *Physics Letters B*, vol. 822, p. 136681, 2021.

[14] C. J. Horowitz, E. F. Brown, Y. Kim, W. G. Lynch, R. Michaels, A. Ono, J. Piekarewicz, M. B. Tsang, and H. H. Wolter, "A way forward in the study of the symmetry energy: experiment, theory, and observation," *Journal of Physics G: Nuclear and Particle Physics*, vol. 41, p. 093001, 2014.

[15] I. Lagaris and V. Pandharipande, "Variational calculations of asymmetric nuclear matter," *Nuclear Physics A*, vol. 369, pp. 470–482, 1981.

[16] M. B. Tsang, Y. Zhang, P. Danielewicz, M. Famiano, Z. Li, W. G. Lynch, and A. W. Steiner, "Constraints on the density dependence of the symmetry energy," *Phys. Rev. Lett.*, vol. 102, p. 122701, 2009.

[17] P. Danielewicz, R. Lacey, and W. G. Lynch, "Determination of the equation of state of dense matter," *Science*, vol. 298, pp. 1592–1596, 2002.

[18] M. Tsang, W. Lynch, P. Danielewicz, and C. Tsang, "Symmetry energy constraints from gw170817 and laboratory experiments," *Physics Letters B*, vol. 795, pp. 533–536, 2019.

[19] B.-A. Li, P. G. Krastev, D.-H. Wen, and N.-B. Zhang, "Towards understanding astrophysical effects of nuclear symmetry energy," *The European Physical Journal A*, vol. 55, p. 117, 2019.

[20] C. J. Horowitz and J. Piekarewicz, "Neutron star structure and the neutron radius of ^{208}pb," *Phys. Rev. Lett.*, vol. 86, pp. 5647–5650, 2001.

[21] B.-A. Li, L.-W. Chen, G.-C. Yong, and W. Zuo, "Double neutron/proton ratio of nucleon emissions in isotopic reaction systems as a robust probe of nuclear symmetry energy," *Physics Letters B*, vol. 634, pp. 378–382, 2006.

[22] N. Ikeno, A. Ono, Y. Nara, and A. Ohnishi, "Probing neutron-proton dynamics by pions," *Phys. Rev. C*, vol. 93, p. 044612, 2016.

[23] M. Cozma, "Neutron-proton elliptic flow difference as a probe for the high density dependence of the symmetry energy," *Physics Letters B*, vol. 700, pp. 139–144, 2011.

[24] L.-W. Chen, C. Ko, and B.-A. Li, "Light cluster production in intermediate energy heavy-ion collisions induced by neutron-rich nuclei," *Nuclear Physics A*, vol. 729, pp. 809–834, 2003.

[25] H. S. Xu, M. B. Tsang, T. X. Liu, X. D. Liu, W. G. Lynch, W. P. Tan, A. Vander Molen, G. Verde, A. Wagner, H. F. Xi, C. K. Gelbke, L. Beaulieu, B. Davin, Y. Larochelle, T. Lefort, R. T. de Souza, R. Yanez, V. E. Viola, R. J. Charity, and L. G. Sobotka, "Isospin fractionation in nuclear multifragmentation," *Phys. Rev. Lett.*, vol. 85, pp. 716–719, 2000.

[26] M. B. Tsang, W. A. Friedman, C. K. Gelbke, W. G. Lynch, G. Verde, and H. S. Xu, "Isotopic scaling in nuclear reactions," *Phys. Rev. Lett.*, vol. 86, pp. 5023–5026, 2001.

[27] P. Senger, "Particle production in heavy-ion collisions," *Progress in Particle and Nuclear Physics*, vol. 53, pp. 1–23, 2004.

[28] J. Hong and P. Danielewicz, "Subthreshold pion production within a transport description of central au + au collisions," *Phys. Rev. C*, vol. 90, p. 024605, 2014.

[29] H. M. Xu, W. G. Lynch, and P. Danielewicz, "Residue temperatures in intermediate energy nucleus-nucleus collisions," *Phys. Rev. C*, vol. 50, pp. 1659–1674, 1994.

[30] B. Borderie and J. Frankland, "Liquid-gas phase transition in nuclei," *Progress in Particle and Nuclear Physics*, vol. 105, pp. 82–138, 2019.

[31] B.-A. Li, C. M. Ko, and Z. Ren, "Equation of state of asymmetric nuclear matter and collisions of neutron-rich nuclei," *Phys. Rev. Lett.*, vol. 78, pp. 1644–1647, 1997.

[32] W. P. Tan, B.-A. Li, R. Donangelo, C. K. Gelbke, M.-J. van Goethem, X. D. Liu, W. G. Lynch, S. Souza, M. B. Tsang, G. Verde, A. Wagner, and H. S. Xu, "Fragment isotope distributions and the isospin dependent equation of state," *Phys. Rev. C*, vol. 64, p. 051901, 2001.

[33] G. Jhang, J. Estee, J. Barney, G. Cerizza, M. Kaneko, J. Lee, W. Lynch, T. Isobe, M. Kurata-Nishimura, T. Murakami, C. Tsang, M. Tsang, R. Wang, D. Ahn, L. Atar, T. Aumann, H. Baba, K. Boretzky, J. Brzychczyk, N. Chiga, N. Fukuda, I. Gasparic, B. Hong, A. Horvat, K. Ieki, N. Inabe, Y. Kim, T. Kobayashi, Y. Kondo, P. Lasko, H. Lee, Y. Leifels, J. Lukasik, J. Manfredi, A. McIntosh, P. Morfouace, T. Nakamura, N. Nakatsuka, S. Nishimura, R. Olsen, H. Otsu, P. Pawlowski, K. Pelczar, D. Rossi, H. Sakurai, C. Santamaria, H. Sato, H. Scheit, R. Shane, Y. Shimizu, H. Simon, A. Snoch, A. Sochocka, Z. Sosin, T. Sumikama, H. Suzuki, D. Suzuki, H. Takeda, S. Tangwancharoen, H. Toernqvist, Y. Togano, Z. Xiao, S. Yennello, J. Yurkon, Y. Zhang, M. Colonna, D. Cozma, P. Danielewicz, H. Elfner, N. Ikeno, C. M. Ko, J. Mohs, D. Oliinychenko, A. Ono, J. Su, Y. J. Wang, H. Wolter, J. Xu, Y.-X. Zhang, and Z. Zhang, "Symmetry energy investigation with pion production from sn+sn systems," *Physics Letters B*, vol. 813, p. 136016, 2021.

[34] T. Alm, G. Röpke, W. Bauer, F. Daffin, and M. Schmidt, "The in-medium nucleon-nucleon cross section and buu simulations of heavy-ion reactions," *Nuclear Physics A*, vol. 587, pp. 815–827, 1995.

[35] B. Barker and P. Danielewicz, "Shear viscosity from nuclear stopping," *Phys. Rev. C*, vol. 99, p. 034607, 2019.

[36] J. Bondorf, A. Botvina, A. Iljinov, I. Mishustin, and K. Sneppen, "Statistical multifragmentation of nuclei," *Physics Reports*, vol. 257, pp. 133–221, 1995.

[37] C. Das, S. Das Gupta, W. Lynch, A. Mekjian, and M. Tsang, "The thermody-

namic model for nuclear multifragmentation," *Physics Reports*, vol. 406, pp. 1–47, 2005.

[38] A. S. Botvina and I. N. Mishustin, "Statistical description of nuclear break-up," *The European Physical Journal A - Hadrons and Nuclei*, vol. 30, p. 121, 2006.

[39] A. Botvina, A. Iljinov, I. Mishustin, J. Bondorf, R. Donangelo, and K. Sneppen, "Statistical simulation of the break-up of highly excited nuclei," *Nuclear Physics A*, vol. 475, pp. 663–686, 1987.

[40] W. P. Tan, S. R. Souza, R. J. Charity, R. Donangelo, W. G. Lynch, and M. B. Tsang, "Isospin effects in nuclear multifragmentation," *Phys. Rev. C*, vol. 68, p. 034609, 2003.

[41] S. Albergo, S. Costa, E. Costanzo, and A. Rubbino, "Temperature and free-nucleon densities of nuclear matter exploding into light clusters in heavy-ion collisions," *Il Nuovo Cimento A (1965-1970)*, vol. 89, pp. 1–28, 1985.

[42] M. B. Tsang, C. K. Gelbke, X. D. Liu, W. G. Lynch, W. P. Tan, G. Verde, H. S. Xu, W. A. Friedman, R. Donangelo, S. R. Souza, C. B. Das, S. Das Gupta, and D. Zhabinsky, "Isoscaling in statistical models," *Phys. Rev. C*, vol. 64, p. 054615, 2001.

[43] G. A. Souliotis, D. V. Shetty, M. Veselsky, G. Chubarian, L. Trache, A. Keksis, E. Martin, and S. J. Yennello, "Isotopic scaling of heavy projectile residues from the collisions of 25MeV/nucleon^{86}Kr with ^{124}Sn, ^{112}Sn and ^{64}Ni, ^{58}Ni," *Phys. Rev. C*, vol. 68, p. 024605, 2003.

[44] S. Wuenschel, R. Dienhoffer, G. A. Souliotis, S. Galanopoulos, Z. Kohley, K. Hagel, D. V. Shetty, K. Huseman, L. W. May, S. N. Soisson, B. C. Stein, A. L. Caraley, and S. J. Yennello, "Isoscaling of fragments with $z = 1-17$ from reconstructed quasiprojectiles," *Phys. Rev. C*, vol. 79, p. 061602, 2009.

[45] M. Youngs, A. McIntosh, K. Hagel, L. Heilborn, M. Huang, A. Jedele, Z. Kohley, L. May, E. McCleskey, A. Zarrella, and S. Yennello, "Observation of different isoscaling behavior between emitted fragments and residues," *Nuclear Physics A*, vol. 962, pp. 61–72, 2017.

[46] A. S. Botvina, O. V. Lozhkin, and W. Trautmann, "Isoscaling in light-ion induced reactions and its statistical interpretation," *Phys. Rev. C*, vol. 65, p. 044610, 2002.

[47] A. Ono, P. Danielewicz, W. A. Friedman, W. G. Lynch, and M. B. Tsang, "Isospin fractionation and isoscaling in dynamical simulations of nuclear collisions," *Phys. Rev. C*, vol. 68, p. 051601, 2003.

[48] G. Kunde, S. Gaff, C. Gelbke, T. Glasmacher, M. Huang, R. Lemmon, W. Lynch, L. Manduci, L. Martin, M. Tsang, W. Friedman, J. Dempsey, R. Charity, L. Sobotka, D. Agnihotri, B. Djerroud, W. SchrÅ¡der, W. Skulski, and J. Toke, "Isospin independence of the h-he double isotope ratio "thermometer"," *Physics Letters B*, vol. 416, pp. 56–61, 1998.

[49] Y. Yano, "The riken ri beam factory project: A status report," *Nuclear Instruments and Methods in Physics Research Section B: Beam Interactions with Materials and Atoms*, vol. 261, pp. 1009–1013, 2007.

[50] J. E. Barney, *CHARGED PION EMISSION FROM ^{112}SN+^{124}SN AND ^{124}SN+^{112}SN REACTIONS WITH THE SπRIT TIME PROJECTION CHAMBER.* PhD thesis, 2019.

[51] H. Otsu, S. Koyama, N. Chiga, T. Isobe, T. Kobayashi, Y. Kondo, M. Kurokawa, W. Lynch, T. Motobayashi, T. Murakami, T. Nakamura, M. Kurata-Nishimura, V. Panin, H. Sato, Y. Shimizu, H. Sakurai, M. Tsang, K. Yoneda, and H. Wang, "Samurai in its operation phase for ribf users," *Nuclear Instruments and Methods in Physics Research Section B: Beam Interactions with Materials and Atoms*, vol. 376, pp. 175–179, 2016.

[52] S. Biagi, "Monte carlo simulation of electron drift and diffusion in counting gases under the influence of electric and magnetic fields," *Nuclear Instruments and Methods in Physics Research Section A: Accelerators, Spectrometers, Detectors and Associated Equipment*, vol. 421, pp. 234–240, 1999.

[53] J. Barney, J. Estee, W. G. Lynch, T. Isobe, G. Jhang, M. Kurata-Nishimura, A. B. McIntosh, T. Murakami, R. Shane, S. Tangwancharoen, M. B. Tsang, G. Cerizza, M. Kaneko, J. W. Lee, C. Y. Tsang, R. Wang, C. Anderson, H. Baba, Z. Chajecki, M. Famiano, R. Hodges-Showalter, B. Hong, T. Kobayashi, P. Lasko, J. Łukasik, N. Nakatsuka, R. Olsen, H. Otsu, P. Pawłowski, K. Pelczar, H. Sakurai, C. Santamaria, H. Setiawan, A. Taketani, J. R. Winkelbauer, Z. Xiao, S. J. Yennello, J. Yurkon, and Y. Zhang, "The sπrit time projection chamber," *Review of Scientific Instruments*, vol. 92, p. 063302, 2021.

[54] Y. Zhang, "The veto collimator for the sπrit-tpc," *RIKEN Accel. Prog. Rep.*, vol. 50, p. 170, 2017.

[55] M. Kaneko, "Kyoto multiplicity array for the sπrit experiment," *RIKEN Accel. Prog. Rep.*, vol. 50, p. 172, 2017.

[56] P. Lasko, M. Adamczyk, J. Brzychczyk, P. Hirnyk, J. Lukasik, P. Pawłowski, K. Pelczar, A. Snoch, A. Sochocka, Z. Sosin, J. Barney, G. Cerizza, J. Estee, T. Isobe, G. Jhang, M. Kaneko, M. Kurata-Nishimura, W. Lynch, T. Murakami, C. Santamaria, M. Tsang, and Y. Zhang, "Katana - a charge-sensitive triggering system for the sπrit experiment," *Nuclear Instruments and Methods in Physics Research Section A: Accelerators, Spectrometers, Detectors and Associated Equipment*, vol. 856, pp. 92–98, 2017.

[57] S. Collaboration, "Sπritroot software," 2021.

[58] G. Jhang, J. Barney, J. Estee, T. Isobe, M. Kaneko, M. Kurata-Nishimura, G. Cerizza, C. Santamaria, J. W. Lee, P. Lasko, J. Łukasik, W. G. Lynch, A. B.

McIntosh, T. Murakami, P. Pawłowski, R. Shane, S. Tangwancharoen, M. B. Tsang, H. Baba, B. Hong, Y. J. Kim, H. S. Lee, H. Otsu, K. Pelczar, H. Sakurai, D. Suzuki, Z. Xiao, S. J. Yennello, and S. Zhang, Yan, "Beam commissioning of the SπRIT time projection chamber," *Journal of the Korean Physical Society*, vol. 69, pp. 144–151, 2016.

[59] J. Lee, G. Jhang, G. Cerizza, J. Barney, J. Estee, T. Isobe, M. Kaneko, M. Kurata-Nishimura, W. Lynch, T. Murakami, C. Tsang, M. Tsang, R. Wang, B. Hong, A. McIntosh, H. Sakurai, C. Santamaria, R. Shane, S. Tangwancharoen, S. Yennello, and Y. Zhang, "Charged particle track reconstruction with sπrit time projection chamber," *Nuclear Instruments and Methods in Physics Research Section A: Accelerators, Spectrometers, Detectors and Associated Equipment*, vol. 965, p. 163840, 2020.

[60] M. Al-Turany, D. Bertini, R. Karabowicz, D. Kresan, P. Malzacher, T. Stockmanns, and F. Uhlig, "The fairroot framework," *Journal of Physics: Conference Series*, vol. 396, p. 022001, 2012.

[61] R. Brun and F. Rademakers, "Root – an object oriented data analysis framework," *Nuclear Instruments and Methods in Physics Research Section A: Accelerators, Spectrometers, Detectors and Associated Equipment*, vol. 389, pp. 81–86, 1997.

[62] E. Mathieson, "Cathode charge distributions in multiwire chambers: 4. empirical formula for small anode-cathode separation," *Nuclear Instruments and Methods in Physics Research Section A: Accelerators, Spectrometers, Detectors and Associated Equipment*, vol. 270, pp. 602–603, 1988.

[63] E. Pollacco, G. Grinyer, F. Abu-Nimeh, T. Ahn, S. Anvar, A. Arokiaraj, Y. Ayyad, H. Baba, M. Babo, P. Baron, D. Bazin, S. Beceiro-Novo, C. Belkhiria, M. Blaizot, B. Blank, J. Bradt, G. Cardella, L. Carpenter, S. Ceruti, E. De Filippo, E. Delagnes, S. De Luca, H. De Witte, F. Druillole, B. Duclos, F. Favela,

A. Fritsch, J. Giovinazzo, C. Gueye, T. Isobe, P. Hellmuth, C. Huss, B. Lachacinski, A. Laffoley, G. Lebertre, L. Legeard, W. Lynch, T. Marchi, L. Martina, C. Maugeais, W. Mittig, L. Nalpas, E. Pagano, J. Pancin, O. Poleshchuk, J. Pedroza, J. Pibernat, S. Primault, R. Raabe, B. Raine, A. Rebii, M. Renaud, T. Roger, P. Roussel-Chomaz, P. Russotto, G. SaccÃ , F. Saillant, P. Sizun, D. Suzuki, J. Swartz, A. TrifirÃ³, N. Usher, G. Wittwer, and J. Yang, "Get: A generic electronics system for tpcs and nuclear physics instrumentation," *Nuclear Instruments and Methods in Physics Research Section A: Accelerators, Spectrometers, Detectors and Associated Equipment*, vol. 887, pp. 81–93, 2018.

[64] G. Jhang, *Performance of the SπRIT TPC for the nuclear physics experiment at RIBF*. PhD thesis, 2016.

[65] A. Strandlie, J. Wroldsen, R. FrÌwirth, and B. Lillekjendlie, "Particle tracks fitted on the riemann sphere," *Computer Physics Communications*, vol. 131, pp. 95–108, 2000.

[66] R. Frühwirth and A. Strandlie, "Robust circle reconstruction with the riemann fit," *Journal of Physics: Conference Series*, vol. 1085, p. 042004.

[67] C. Tsang, J. Estee, R. Wang, J. Barney, G. Jhang, W. Lynch, Z. Zhang, G. Cerizza, T. Isobe, M. Kaneko, M. Kurata-Nishimura, J. Lee, T. Murakami, and M. Tsang, "Space charge effects in the sπrit time projection chamber," *Nuclear Instruments and Methods in Physics Research Section A: Accelerators, Spectrometers, Detectors and Associated Equipment*, vol. 959, p. 163477, 2020.

[68] J. Rauch and T. SchlÃŒter, "GENFIT — a generic track-fitting toolkit," *Journal of Physics: Conference Series*, vol. 608, p. 012042.

[69] R. Frühwirth, "Application of kalman filtering to track and vertex fitting," *Nuclear Instruments and Methods in Physics Research Section A: Accelerators, Spectrometers, Detectors and Associated Equipment*, vol. 262, pp. 444–450, 1987.

[70] W. Waltenberger, "Adaptive vertex reconstruction," tech. rep.

[71] W. Waltenberger, "Rave - a detector-independent toolkit to reconstruct vertices," *IEEE Transactions on Nuclear Science*, vol. 58, pp. 434–444, 2011.

[72] Particle Data Group, P. A. Zyla, R. M. Barnett, J. Beringer, O. Dahl, D. A. Dwyer, D. E. Groom, C. J. Lin, K. S. Lugovsky, E. Pianori, D. J. Robinson, C. G. Wohl, W. M. Yao, K. Agashe, G. Aielli, B. C. Allanach, C. Amsler, M. Antonelli, E. C. Aschenauer, D. M. Asner, H. Baer, S. Banerjee, L. Baudis, C. W. Bauer, J. J. Beatty, V. I. Belousov, S. Bethke, A. Bettini, O. Biebel, K. M. Black, E. Blucher, O. Buchmuller, V. Burkert, M. A. Bychkov, R. N. Cahn, M. Carena, A. Ceccucci, A. Cerri, D. Chakraborty, R. S. Chivukula, G. Cowan, G. D'Ambrosio, T. Damour, D. de Florian, A. de Gouvêa, T. DeGrand, P. de Jong, G. Dissertori, B. A. Dobrescu, M. D'Onofrio, M. Doser, M. Drees, H. K. Dreiner, P. Eerola, U. Egede, S. Eidelman, J. Ellis, J. Erler, V. V. Ezhela, W. Fetscher, B. D. Fields, B. Foster, A. Freitas, H. Gallagher, L. Garren, H. J. Gerber, G. Gerbier, T. Gershon, Y. Gershtein, T. Gherghetta, A. A. Godizov, M. C. Gonzalez-Garcia, M. Goodman, C. Grab, A. V. Gritsan, C. Grojean, M. Grünewald, A. Gurtu, T. Gutsche, H. E. Haber, C. Hanhart, S. Hashimoto, Y. Hayato, A. Hebecker, S. Heinemeyer, B. Heltsley, J. J. Hernández-Rey, K. Hikasa, J. Hisano, A. Höcker, J. Holder, A. Holtkamp, J. Huston, T. Hyodo, K. F. Johnson, M. Kado, M. Karliner, U. F. Katz, M. Kenzie, V. A. Khoze, S. R. Klein, E. Klempt, R. V. Kowalewski, F. Krauss, M. Kreps, B. Krusche, Y. Kwon, O. Lahav, J. Laiho, L. P. Lellouch, J. Lesgourgues, A. R. Liddle, Z. Ligeti, C. Lippmann, T. M. Liss, L. Littenberg, C. Lourengo, S. B. Lugovsky, A. Lusiani, Y. Makida, F. Maltoni, T. Mannel, A. V. Manohar, W. J. Marciano, A. Masoni, J. Matthews, U. G. Meißner, M. Mikhasenko, D. J. Miller, D. Milstead, R. E. Mitchell, K. Mönig, P. Molaro, F. Moortgat, M. Moskovic, K. Nakamura, M. Narain, P. Nason, S. Navas, M. Neubert, P. Nevski, Y. Nir, K. A. Olive, C. Patrignani, J. A. Peacock, S. T. Petcov,

V. A. Petrov, A. Pich, A. Piepke, A. Pomarol, S. Profumo, A. Quadt, K. Rabbertz, J. Rademacker, G. Raffelt, H. Ramani, M. Ramsey-Musolf, B. N. Ratcliff, P. Richardson, A. Ringwald, S. Roesler, S. Rolli, A. Romaniouk, L. J. Rosenberg, J. L. Rosner, G. Rybka, M. Ryskin, R. A. Ryutin, Y. Sakai, G. P. Salam, S. Sarkar, F. Sauli, O. Schneider, K. Scholberg, A. J. Schwartz, J. Schwiening, D. Scott, V. Sharma, S. R. Sharpe, T. Shutt, M. Silari, T. Sjöstrand, P. Skands, T. Skwarnicki, G. F. Smoot, A. Soffer, M. S. Sozzi, S. Spanier, C. Spiering, A. Stahl, S. L. Stone, Y. Sumino, T. Sumiyoshi, M. J. Syphers, F. Takahashi, M. Tanabashi, J. Tanaka, M. Taševský, K. Terashi, J. Terning, U. Thoma, R. S. Thorne, L. Tiator, M. Titov, N. P. Tkachenko, D. R. Tovey, K. Trabelsi, P. Urquijo, G. Valencia, R. Van de Water, N. Varelas, G. Venanzoni, L. Verde, M. G. Vincter, P. Vogel, W. Vogelsang, A. Vogt, V. Vorobyev, S. P. Wakely, W. Walkowiak, C. W. Walter, D. Wands, M. O. Wascko, D. H. Weinberg, E. J. Weinberg, M. White, L. R. Wiencke, S. Willocq, C. L. Woody, R. L. Workman, M. Yokoyama, R. Yoshida, G. Zanderighi, G. P. Zeller, O. V. Zenin, R. Y. Zhu, S. L. Zhu, F. Zimmermann, J. Anderson, T. Basaglia, V. S. Lugovsky, P. Schaffner, and W. Zheng, "Review of particle physics," *Progress of Theoretical and Experimental Physics*, vol. 2020, p. 083C01, 2020.

[73] M. Anderson, J. Berkovitz, W. Betts, R. Bossingham, F. Bieser, R. Brown, M. Burks, M. CalderÃ³n de la Barca SÃ¡nchez, D. Cebra, M. Cherney, J. Chrin, W. Edwards, V. Ghazikhanian, D. Greiner, M. Gilkes, D. Hardtke, G. Harper, E. Hjort, H. Huang, G. Igo, S. Jacobson, D. Keane, S. Klein, G. Koehler, L. Kotchenda, B. Lasiuk, A. Lebedev, J. Lin, M. Lisa, H. Matis, J. Nystrand, S. Panitkin, D. Reichold, F. Retiere, I. Sakrejda, K. Schweda, D. Shuman, R. Snellings, N. Stone, B. Stringfellow, J. Thomas, T. Trainor, S. Trentalange, R. Wells, C. Whitten, H. Wieman, E. Yamamoto, and W. Zhang, "The star time projection chamber: a unique tool for studying high multiplicity events at rhic," *Nuclear Instruments and Methods in Physics Research Section A: Accelerators,*

Spectrometers, Detectors and Associated Equipment, vol. 499, pp. 659–678, 2003.

[74] C. Cavata, M. Demoulins, J. Gosset, M.-C. Lemaire, D. L'Hôte, J. Poitou, and O. Valette, "Determination of the impact parameter in relativistic nucleus-nucleus collisions," *Phys. Rev. C*, vol. 42, pp. 1760–1763, 1990.

[75] J. W. Lee, M. B. Tsang, C. Y. Tsang, R. Wang, J. Barney, J. Estee, T. Isobe, M. Kaneko, M. Kurata-Nishimura, W. G. Lynch, T. Murakami, A. Ono, S. R. Souza, D. S. Ahn, L. Atar, T. Aumann, H. Baba, K. Boretzky, J. Brzychczyk, G. Cerizza, N. Chiga, N. Fukuda, I. Gasparic, B. Hong, A. Horvat, K. Ieki, N. Ikeno, N. Inabe, G. Jhang, Y. J. Kim, T. Kobayashi, Y. Kondo, P. Lasko, H. S. Lee, Y. Leifels, J. Łukasik, J. Manfredi, A. B. McIntosh, P. Morfouace, T. Nakamura, N. Nakatsuka, S. Nishimura, H. Otsu, P. Pawłowski, K. Pelczar, D. Rossi, H. Sakurai, C. Santamaria, H. Sato, H. Scheit, R. Shane, Y. Shimizu, H. Simon, A. Snoch, A. Sochocka, T. Sumikama, H. Suzuki, D. Suzuki, H. Takeda, S. Tangwancharoen, Y. Togano, Z. G. Xiao, S. J. Yennello, and Y. Zhang, "Isoscaling in central Sn+Sn collisions at 270 MeV/u," *The European Physical Journal A*, vol. 58, no. 10, p. 201, 2022.

[76] Z. Chajecki, M. Youngs, D. D. S. Coupland, W. G. Lynch, M. B. Tsang, D. Brown, A. Chbihi, P. Danielewicz, R. T. deSouza, M. A. Famiano, T. K. Ghosh, B. Giacherio, V. Henzl, D. Henzlova, C. Herlitzius, S. Hudan, M. A. Kilburn, J. Lee, F. Lu, S. Lukyanov, A. M. Rogers, P. Russotto, A. Sanetullaev, R. H. Showalter, L. G. Sobotka, Z. Y. Sun, A. M. V. Molen, G. Verde, M. S. Wallace, and J. Winkelbauer, "Scaling properties of light-cluster production," 2014.

[77] S. Souza, B. Carlson, and R. Donangelo, "Post breakup dynamical evolution of fragments produced in nuclear multifragmentation," *Nuclear Physics A*, vol. 989, pp. 69–80, 2019.

[78] A. Ono, H. Horiuchi, T. Maruyama, and A. Ohnishi, "Antisymmetrized version

of molecular dynamics with two-nucleon collisions and its application to heavy ion reactions," *Progress of Theoretical Physics*, vol. 87, pp. 1185–1206, 1992.

[79] A. Ono, "Impacts of cluster correlations on heavy-ion collision dynamics," *JPS Conf. Proc.*, vol. 32, p. 010076, 2020.